UNIVERSITY OF OKLAHOMA

GRADUATE COLLEGE

THE ABUNDANCE AND CHEMICAL EVOLUTION OF NITROGEN IN SPIRAL GALAXIES

A DISSERTATION

SUBMITTED TO THE GRADUATE FACULTY

in partial fulfillment of the requirements for the

degree of

DOCTOR OF PHILOSOPHY

By

TAD R. THURSTON

Norman, Oklahoma

1998

UMI Number: 9826293

THE ABUNDANCE AND CHEMICAL EVOLUTION OF NITROGEN IN SPIRAL GALAXIES

A DISSERTATION APPROVED FOR THE DEPARTMENT OF PHYSICS AND ASTRONOMY

BY

Richard Henry

John Cowan

David Branch

Jack Cohn

Joseph Rodgers

Acknowledgments

The opportunity and gift to participate in a field of study that I love does not come without the love and support of those who have been close to me, and I wish to recognize the following people who have helped me to realize my ambitions:

Dr. Mike Edmunds deserves recognition for his collaborative trips to the U.S., his patient and enthusiastic support of research ideas, and stimulating conversations and comments.

Two members of my graduate committee: Dr. David Branch and Dr. John Cowan. I have worked with and known you for many years, and have grown and learned much under your teaching.

Dr. Jack Cohn, for being a good friend through the years and always "stoking the fire." You have continuously inspired the wonder and deep questions that initially attracted me to science.

Dr. Joe Rodgers, for being a valued friend and teacher to our family.

Dr. Richard Henry, for seeing me through these 10 (!) years and a calm guiding voice who has been with me from my earliest studies in astronomy. Your patience and encouragement through my life's changes has been greatly appreciated, and I look forward to many more years of friendship and collaboration.

"The Group": Truly no one has had a better group of friends. You all are as family to me.

Leona and Mike McKinley, who welcomed me into their family with open arms.

To Grandmother, a remarkable woman and also a friend, I love you and miss you.

Torin and Tammy, you have shown me love and the meaning of family. Our relationships are a blessing in my life.

My parents, Richard and Iris, for the unswerving commitment and encouragement these many years. I could not have asked for a more nurturing environment from which to follow my passions. I would not be where I am today were it not for your continuing love and support.

And finally, I wish to recognize the two most important people in my life, my wife Karen and son Gehrig. To thank you is not enough; you are the anchor and the center of my life. It is one thing to have a best friend, it is quite another to be able to spend your life with them. Gehrig, every day you show the wonder and the fascination that is the basis for true love both for others and in life. I am truly blessed.

Contents

List of Tables

List of Figures

Chapter 1

Introduction

1.1 Galactic Processing of the Elements and H II Regions

One of the great realizations in modern science since the Enlightenment is the understanding that the universe is *dynamic*. The physical properties of systems in the past is, in general, not the same as those properties measured presently. The universe, and the systems that comprise it, evolve over time. Another great foundation for modern scientific thought is that the evolution of these systems proceeds through understandable and predictable processes. We may predict the evolution of systems over time via application of standard modes of scientific inquiry: observation of present parameters and prediction of the future values of those parameters based upon "known" principles. In this dissertation, I shall attempt to follow the spirit of this paradigm as it relates to my investigation of the evolution of nitrogen processing in spiral galaxies.

Most of our information regarding the abundance of nitrogen comes from the observation of gaseous nebulae in spirals. Photographs of spiral galaxies often show bright "knotty" regions along the spiral arms that are, in fact, areas of active star formation. These clumps of gas are typically illuminated by ionizing radiation from giant O- and B-type stars with surface temperatures of about 40,000K that have been newly formed. We commonly designate these as "HII" regions, named for the singly ionized state (HII) of hydrogen that largely defines the luminous area. HII regions are not very dense (electron densities of $\sim 10 - 100$ cm^{-3}), and usually have strong optical emission lines of elements such as hydrogen, helium, nitrogen and oxygen. Free electrons are generated from the photoionization of neutral hydrogen, where photons with energies greater than 13.6 eV are absorbed, and the energy is transferred to the newly liberated electrons. These electrons may collisionally excite orbital electrons of other elements to higher levels, producing characteristic spectral lines upon de-excitation. These collisions tend to thermalize the gas, giving a Maxwellian velocity distribution with temperature T of typically 10,000K. Interestingly, the low densities of HII regions enable historically "forbidden" atomic transitions to take place, such as the lines of [OIII] $\lambda\lambda$4959, 5007, the green pair of lines once thought to indicate the presence of the hypothetical new element *nebulium*.

HII regions are of great importance in the study of galactic dynamics and chemical evolution. From spectral analysis, one may directly sample the chemical makeup of a spiral galaxy in star-forming regions at the present time. This is an important distinction to draw between different types of nebulae; for other types, such as supernovae remnants and planetary nebulae, the gas represents the processed remains of a star at the end of its lifetime. This gas may therefore reflect the abundance of elements at the time of stellar birth (which may be a long time ago), as well as a measure of the degree of elemental processing that took place within the star. HII regions, on the other hand, are illuminations of relatively unprocessed gas that has recently collapsed into stars. We are thus measuring the *current* chemical composition of the distant stellar neighborhood with observations of these regions.

To illustrate the dynamic paradigm as mentioned above, consider a standard model of galactic chemical evolution. A simple model of galaxy formation begins with a rotating spherical distribution of gas. Angular momentum conservation along with gravitational self-collapse flattens the sphere over time into a disk. The gas that falls onto the proto-disk will have chemical properties very much like the matter left over from the Big Bang — a mixture of about 75% hydrogen and 25% helium, along with traces of lithium and deuterium. As the gas falls onto the disk, local gravitational instabilities trigger collapse of small clumps of material, forming the first (not counting stars that formed in the original sphere) generation of stars. The most massive of these evolved fastest, generating new elements such as carbon, nitrogen, and oxygen during their lifetime (elements with atomic numbers greater than that of helium are collectively referred to by astronomers as "metals"). These new elements are released into the local interstellar medium (ISM) along with still heavier elements (magnesium, sulfur, and iron) manufactured during the massive stars' death processes. Future generations of stars will incorporate these elements and manufacture more. Generally, the abundance of heavy elements continues to increase while the abundance of hydrogen will decrease (since there is no source of new hydrogen). Details of the different death processes of stars are important, as stars of varying mass have vastly different lifetimes. The chief source of iron, for instance, is thought to be type Ia supernovae. These explosions are ultimately the result of relatively small stars in binary systems that accrete gas from their neighbors past the Chandrasekhar limit, and then undergo a thermonuclear deflagration. Small stars, however, have a long lifetime. We should expect to find a time delay for the enrichment of iron as opposed to, say, sulfur and oxygen (produced in the explosions of short-lived, massive stars). The relation between the abundance of manufactured elements and time is often used as a sort of clock; i.e. small stars with extremely low metal abundances were probably formed a very long time ago, before the widespread pollution of the local ISM.

1.2 The Importance of Chemical Abundance Determinations

Chemical abundances of HII regions are important not only to determine the chemical properties of the star-forming region, but also for the analysis of large-scale trends in galaxies. Many spiral galaxies each have numerous HII regions scattered along the disk, and intrinsic variations of elemental abundances have been discovered with correlations to a number of parameters. The ratio of [N/O], for instance, declines along the outward radius of spirals (Chapter 3). The ratio of [N/S] increases with the mass of galaxies for a given value of galactic radius (Chapter 4). These relations, interpreted with the results of numerical chemical evolution modeling (Chapter 2), may give some insight into other galactic properties.

In particular, this dissertation will focus on the abundance and evolution of nitrogen. New tabulations detailing the generation of nitrogen in intermediate-mass stars may lead to an understanding of the galactic processing history of this element. It seems to be generated almost entirely in stars between 1 and 8 solar masses, and there is evidence that the yield from these stars may depend significantly upon the initial abundance of a "seed" element. This would seem to imply that in the distant past, when the overall abundance of metals was deficient, the yield of nitrogen was different than it is presently. This is an important hypothesis to be addressed in this thesis.

Further, abundance measurements are important parameters used to constrain numerical models. This will be seen in Chapter 2, as the chief test of the simulation is to accurately reflect the current elemental abundances.

1.3 Research Outline of this Dissertation

The goals for this research program may be summarized by previewing the subsequent chapters. In Chapter 2, I discuss the new chemical evolution code, NICE, and test the code against observational constraints. In order to address the evolution of nitrogen, I must first possess a database of nitrogen abundances. Nitrogen abundances are often difficult to calculate directly, due to the weakness of a diagnostic spectral line. I (in collaboration with Dr. Mike Edmunds and Dr. Richard Henry) developed and tested an algorithm to compute these abundances from stronger, more easily observed emission lines. Chapter 3 details this algorithm as well as the testing procedure. A new database of nitrogen abundances for 164 extragalactic HII regions and star formation regions in dwarf galaxies is given in Appendix A. Finally, in Chapter 4 I apply the NICE code to determine which galactic properties are responsible for the behavior of certain elemental ratios found in Chapter 3 and in the literature. I shall also attempt to probe the early chemical history of nitrogen in galaxies and an account of the relative importance of two nitrogen generation mechanisms.

Chapter 2

Chemical Evolution Modeling

I will develop in this chapter a treatment of galactic chemical evolution. The eventual goal is a series of relationships between the evolution of nitrogen, oxygen, and the surrounding galactic environmental parameters.

In § 2.1 I describe an analytical framework from which to build a numerical model of chemical evolution. This is followed in § 2.2 by a description of the code itself, and then in § 2.3 by tests of the code and comparison to previous efforts and observations.

2.1 Analytic Considerations

Analytic treatments of physical systems are very useful in understanding the behavior of complex numerical treatments. In providing simple behavioral aspects of the variables involved, they also serve as a guide to testing the output of numerical codes. The goal of this section is to serve both purposes with respect to the NICE program to follow.

I will first develop the "simple" closed box model (Pagel and Patchett 1975), which traces the evolution of gas and heavy element production in a column of gas (here called a "cell") at an arbitrary position in a galaxy. Gas and other densities are often given in terms of a surface density, σ, in order to mask variations of these parameters with galactic scale height. These variations are hard to obtain observationally for other galaxies, and are not well quantified. This simple model assumes an initial mass of unenriched gas (unenriched, for this discussion, is equivalent to a 75% hydrogen and 25% helium mix by mass) which undergoes star formation, stellar evolution, and stellar death. Any element with an atomic number greater than Helium ($Z > 2$) will have been generated in stars in these models. These generated elements will globally be referred to as "metals" or "heavy elements". Stars return gas to the interstellar medium in two basic methods:

- Loss of the outer envelope via stellar pulsations and radiative pressure
- Loss of elementally enriched material via explosive death processes

These processes and the quantities of elements returned, as will be seen, are dependent upon the mass of the star in question. The epoch of stellar birth is also important — new calculations (Buell (1997), van den Hoek and Groenewegen (1996)) show the dependence of the elemental yields on the initial metal content of the star. The total mass of the cell is the sum of two components: the mass of gas and the mass of stars. Initially, the total mass is entirely gas; as the cell evolves, the gas is used in star formation and some mass is locked away in long-lived stellar remnants such as white dwarfs, neutron stars, and black holes. The mass in remnants is unrecoverable as gas, except in the case of a binary system with at least one white dwarf. These systems may undergo a tremendous explosion called a supernova, and return newly generated heavy elements back to the interstellar medium (ISM). Over time, then, the gas mass is expected to decline while the stellar mass will increase. The decline of gas mass will have an effect on the rate of new star formation (assumed to be a function of the amount of gas present) and therefore the subsequent metal enrichment of the cell.

The simple model is characterized by two assumptions:

- *Instantaneous Recycling Approximation* New elements are generally formed in the cores of massive stars, which live very short lifetimes as compared to low-mass stars. Over long timescales, such as the evolution of the galactic disk, it is assumed that these massive stars live infinitesimally short lifetimes. As soon as they are formed they return some quantity of processed material back to the ISM.

- *Closed-box Approximation* The total amount of mass in the cell is constant. The form of the mass shifts from gas to stars and stellar remnants, but there is no new source of gas infall or outflow.

The standard notation used here will follow that of Edmunds (1990), where

g = gas mass

z = fraction of heavy elements

α = fraction of mass formed into stars not returned to the ISM

p' = fraction of mass formed into heavy elements and returned to the ISM

ds = amount of local ISM mass formed into stars in time dt

In general, the change of overall metallicity for a region proceeds as

$$d(gz) = p'\,ds - \alpha z\,ds$$

which states simply that the difference between the mass of metals produced and the mass locked away in long-lived stellar remnants must enrich the local ISM. The change in the gas mass is then

$$dg = -\alpha\,ds$$

Now expanding the differential above,

$$g\,dz + z\,dg = p'\,ds - \alpha z\,ds$$

this leads to

$$dz = \frac{p'\,ds}{g}$$

If we identify

$$\begin{aligned} p' &= \alpha p \\ f &= \frac{g}{g + \alpha s} \end{aligned}$$

where p is the "yield" and f is the gas fraction, we then obtain

$$dz = pf\, d(\frac{1}{f})$$

$$\Rightarrow z = p\, \ln(\frac{1}{f})$$

which is the well-known relation for the evolution of metallicity as a function of gas fraction in a simple, closed-box model. The result is not surprising, as the overall metallicity of the cell should increase with the efficiency of metal production and the decrease of available gas.

It will be useful to define the "effective yield", p_{eff}, which is the yield that would be deduced if the system were assumed to be a simple model,

$$p_{\text{eff}} = \frac{z}{\ln(\frac{1}{f})}$$

The assumptions of the simple model are almost certainly false. A component of the standard model of galaxy formation includes infall of material from a spherical halo onto a disk. Material is also ejected from the disk via supernovae winds, although I will neglect outflow in the discussion to follow.

An expanded list of assumptions in the simple model, is given by Tinsley (1980):

1) The solar neighborhood can be modeled as a closed system

2) The local environment was initially unenriched material

3) The mass distribution function for stellar births is constant, and

4) The gas is chemically homogeneous at all times

As asserted above, (1) is almost certainly incorrect. Assumptions (2)-(4) are also probably incorrect, but not violated sufficiently to solve the problem. In fact, in the code NICE I shall hold to assumptions (2)-(4) but introduce a time-varying exponential form of infall.

The instantaneous recycling approximation is also invalid for the consideration of nitrogen. The major contributors of nitrogen seem to be intermediate mass stars with main-sequence masses of 1-8 solar masses (Renzini and Voli (1981), Buell (1997), van den Hoek and Groenewegen (1996)), and since stellar lifetimes scale approximately as

$$\tau \sim M^{-2.5}$$

we cannot neglect the timescale of these processes.

These aforementioned theorems will be used to guide the choice of parameters and evaluation of the numerical code in the next section.

Relaxing these requirements of the simple model, it is useful to employ a generalized infall in analytic models to gauge the realistic behavior of metallicity in a model cell, as done by Edmunds (1990). Three important theorems from that study are now presented (italicized expressions are discussed below):

- In a model with inflow of unenriched gas, the effective yield is always less than that of the simple model
- In a model with inflow, the ratio of yields of a *secondary* to a *primary* element is always greater than for a simple model

- The *G dwarf problem* can be solved by particular forms of inflow (in particular, non-linear inflow)

A secondary element is defined as an element whose production is directly proportional to the abundance of a pre-existing primary "seed" element (Edmunds (1990)). The production of a primary element is independent of any such seed element. In particular, nitrogen is thought to be synthesized in the processing of oxygen and carbon via the CNO cycle. If only the oxygen and carbon originally incorporated into the star when it formed are involved in nitrogen production, then the resulting nitrogen is termed "secondary." Under these circumstances, the ratio of (N/O) is expected to increase linearly with (O/H). Primary nitrogen could be generated from the carbon and oxygen produced by helium burning in the core of the star and later mixed into a hydrogen-burning shell. Note that in this way the synthesized nitrogen is *not* dependent on the *initial* abundance of O and C, since they were newly manufactured in the star. Convective dredging may then bring nitrogen near the stellar surface, where it is later returned to the ISM through main-sequence mass loss mechanisms or in planetary nebulae ejecta.

The G dwarf problem can be stated simply as follows: There are far fewer small metal-poor stars in the solar neighborhood than one predicts using assumptions from the simple model. The canonical form of the mass distribution of new stars is a power law weighted towards lower-mass objects. If one assumes an initially unenriched mass of gas that undergoes star formation, many low-mass stars are formed that have little processed metal enrichment. Since stellar lifetimes also can be represented as an inverse power-law with respect to mass (see the relation above), we expect that these initial small stars will live a very long time (longer, in fact, than the age of the disk of the galaxy). Since we do not see these metal-deficient dwarfs in great numbers, we must revise our assumptions regarding the initial state of the disk of the galaxy. A simple solution to this problem is given by assuming a time-dependent infall of primordial gas onto the disk. Here, there is relatively little gas available at first to form stars, and the local environment is imbued with processed material from the first generation of high-mass stars. Later dwarfs formed will incorporate these new metals, and we see the resultant abundance spectrum in Fig. 2.7.

2.2 Numerical Modeling — NICE

The following section describes the code NICE written in C++ for this dissertation. A complete code listing, as well as a sample makefile and the stellar yields database is also included in Appendix B. Interested readers may enter the code as presented into the 5 files:

```
nice.cc

nice_functions.cc

nice.hh

nice_yields.hh

Makefile
```

Using the sample makefile included in Appendix B with a standard GNU C++ compiler, one should only have to type `make` to compile and `NICE` to run.

The program instantiates a new data type called `Element`. A two-dimensional array of pointers to individual element objects is then created. Each entry is indexed by the elemental species as well as the current loop number in the code. In this way, the abundance history of each element can be queried. Access to member variables such as mass fraction, mass fraction in infall material, amount ejected this iteration, and total mass are provided by the accessor member functions. Each element considered, then, records relevant quantities about itself during each iteration.

2.2.1 Overview

For this discussion, I will change to a more tractable notation following Tinsley (1980). For a closed system, as discussed earlier, the total mass of gas within the cell does not change. In this model, however, an inflow of gas into the cell is allowed. The total mass of the cell will evolve as

$$\frac{dM_t}{dt} = f$$

where f is the rate of infall of new gas, in solar masses per 10^9 years (Gyr). A cell is now formally defined as the entire column of gas intersecting the galactic plane with a cross-sectional area of 1 pc^2. Ordinarily, the intensity of emission lines from distant galaxies is integrated in a direction along the column towards the observer, so this is a "natural" choice for a model volume. Observations therefore often refer to quantities based upon the "surface density" of gas and elemental mass fractions. The total mass M_t of the cell is comprised of two components, the stellar mass M_s and the gas mass M_g. The gas mass in the cell may change via three mechanisms: infall, star formation, and ejection of gas from dying stars. Star formation depletes the cell of gas (making it into stars), while the other two processes augment M_g. We have then

$$\frac{dM_g}{dt} = -\psi + E + f$$

We will consider specific models for the star formation rate (SFR) ψ, the infall rate, and the initial mass function (IMF) in sections to follow.

The mass ejection rate is simply that mass returned to the interstellar medium (ISM) during the death of a star. If we define m as the initial mass (zero-age main sequence mass, or ZAMS), then what is returned is just the difference between the initial mass and final, or remnant, mass. The remnant mass is most often the mass of the long-lived core of the former star, usually in the form of a white dwarf, neutron star, or black hole. If we call the remnant mass w_m, then the ejected mass rate is

$$E(t) = \int_{m_t}^{m_{up}} (m - w_m)\psi(t - \tau_m)\phi(m)\, dm$$

Here, m_t is called the "turnoff mass," which indicates that all stars above this mass have evolved and have therefore returned some gas back to the ISM. Data for the main sequence lifetime of stars in this study are given in Schaller et al. (1992) and in Appendix B. There is a slight metallicity dependence of the lifetimes, so this parameter should be adjusted as the galaxy evolves, but the effect is small enough to ignore in most chemical evolution scenarios (Timmes, Woosley and Weaver (1995)). The upper limit of integration, $m_{\rm up}$, will be discussed below as well. A new parameter is τ_m, which is the lifetime of a star of initial mass m. We must evaluate the SFR at this earlier time $(t - \tau_m)$, since environmental conditions may have been very different when this star was born. If $\tau_m = 0$, then we recover the instantaneous recycling approximation discussed earlier. We also must include the IMF, $\phi(m)$, which represents the fraction of all stars formed that fall between m and $m + dm$. The IMF is normalized such that

$$\int_0^\infty m\phi(m)\,dm = 1$$

NICE is an isotopic chemical evolution model, so we are concerned with the rate of change of specific isotopes. Calling the mass fraction of a specific isotope Z, our gas mass rate equation becomes

$$\frac{d(ZM_g)}{dt} = -Z\psi + E_z + Z_f f$$

where E_z is the total ejection rate of this isotope from stars and Z_f is the mass fraction of isotope Z in the infalling gas. To obtain a new expression for E_z, we need to determine the amount of Z ejected from each mass of star in our integration range. Call this parameter, p_z, the *yield*. This terminology is not unique, as the yield can also be defined as the *mass* of isotopes ejected per unit mass of matter locked into stars. This difference will be addressed in the formal calculations, as the yields given in the literature may adopt either of these schemes. It is certainly plausible that $p_z = p_z(m)$, as stars of different masses have very different lifetimes, core temperatures and environments, and energy generation mechanisms. Low- and intermediate-mass stars ($< 8M_\odot$), as will be seen, are the chief contributors of nitrogen to the ISM. Oxygen, on the other hand, is almost completely a product of massive star ($> 8M_\odot$) evolution. It is important to realize that E_Z includes not only the new elements generated within the star, but also the unprocessed elements that were present when the star was born and ejected during final-stage mass loss. This unprocessed returned material has a mass of $(m - w_m - mp_z)$, and the mass of unprocessed isotope Z will be $Z(t-\tau_m)(m - w_m - mp_z)$. Once again we must use the historical value $Z(t-\tau_m)$, as the mass fraction of isotope Z is not constant in time, and we would like to know the mass fraction of Z that was incorporated into the star at time $(t - \tau_m)$ ago. We may now write the total ejection rate of processed and unprocessed Z as

$$E_z(t) = \int_{m_t}^{m_{up}} [(m - w_m - mp_z)Z(t-\tau_m) + mp_z]\psi(t-\tau_m)\phi(m)\,dm$$

Assuming expressions for the star formation rate and the infall rate, we may now integrate ZM_g over time to calculate the complete chemical history of Z. These expressions, as well as the other functions used in the code, are described in more detail in the following sections.

2.2.2 Star Formation Rate

To obtain the rate of star formation (and thus the rate of depletion of the gas), one may start with the function assumed by Schmidt (Schmidt (1959), Schmidt (1963)),

$$\psi(t) \approx \rho_{gas}^n$$

It is naively justifiable that the SFR depends on some power of the gas density, as a higher gas density might trigger a higher rate of local instabilities. These instabilities presumably result in stars being formed in this region. Schmidt had rough observational justification for $n = 2$, as stated by Timmes, Woosley and Weaver (1995). A subtle consideration is that Schmidt's function utilizes the *volume* density, while the computations in NICE operate using a *surface* density σ_g. Of course, the two systems are equal for $n = 1$, but are also equal if the scale height of the gas above the galactic disk is constant along the galactocentric radius (the scale height is the exponential decrease in gas density in a direction perpendicular to the radius vector). This assumption is probably false, due to the gravitational potential variations along the disk, but will be employed here nevertheless for simplicity. Many observational parameters are best expressed in terms of the scale height, since an explicit computation of the scale height is avoided. For these results, a Schmidt function with a dependence on the total gas mass is adopted (Timmes, Woosley and Weaver (1995), with cutoff modification by Gratton et al. (1996), and references therein),

$$\psi(t) = \nu\sigma_t(t)\left\{\frac{\sigma_g(t)}{\sigma_t(t)}\right\}^2 M_\odot\,\mathrm{Gyr}^{-1}$$

$$\psi(t) = 0 \text{ when } \sigma_g(t) \leq 7\,M_\odot$$

where ν is the efficiency of star formation (in Gyr^{-1}), and σ_t is the total mass surface density (gas + stars). Another possible formulation is given by Chiappini, Matteucci and Gratton (1996), Matteucci and François (1989),

$$\psi(r,t) = \nu\sigma_g^{1.1}(r)\sigma_t^{0.1}(r)$$

$$\psi(r,t) = 0 \text{ when } \sigma_g(r,t) \leq 7\, M_\odot$$

and quoted in Tosi (1996). This is different from the previous form in that there is a direct dependence on the *total* mass density. This is a way to take into account the local environment, and in particular the local gravitational potential. The motivation for this choice is the consideration that the greater the gravitational potential, the easier it is for gas to collapse into stars.

Both forms include the SFR cutoff (Gratton et al. (1996)), implying that there is a threshold below which there is no star formation. This threshold is suggested by observations relative to the massive star formation in external galaxies (Kennicutt (1989)). It is also suggested physically by the consideration of gravitational stability — below a critical density the gas is stable against density condensations, and consequently the star formation rate is suppressed. A plot of the SFR against time is shown in Fig. 2.1 for this study. Note in the plot the oscillatory behavior due to the implementation of the cutoff value. As the SFR cuts off, infall of new material and the ejected mass from evolved starts drives the local gas density above the critical value until star formation consumes enough gas to drop σ_g back below the critical point.

Tosi (1996) compares different models of chemical evolution, and notes how strikingly similar the results are for varying input models of $\psi(t)$. In fact, it can be seen that the star formation rate function used in NICE produces a plot of

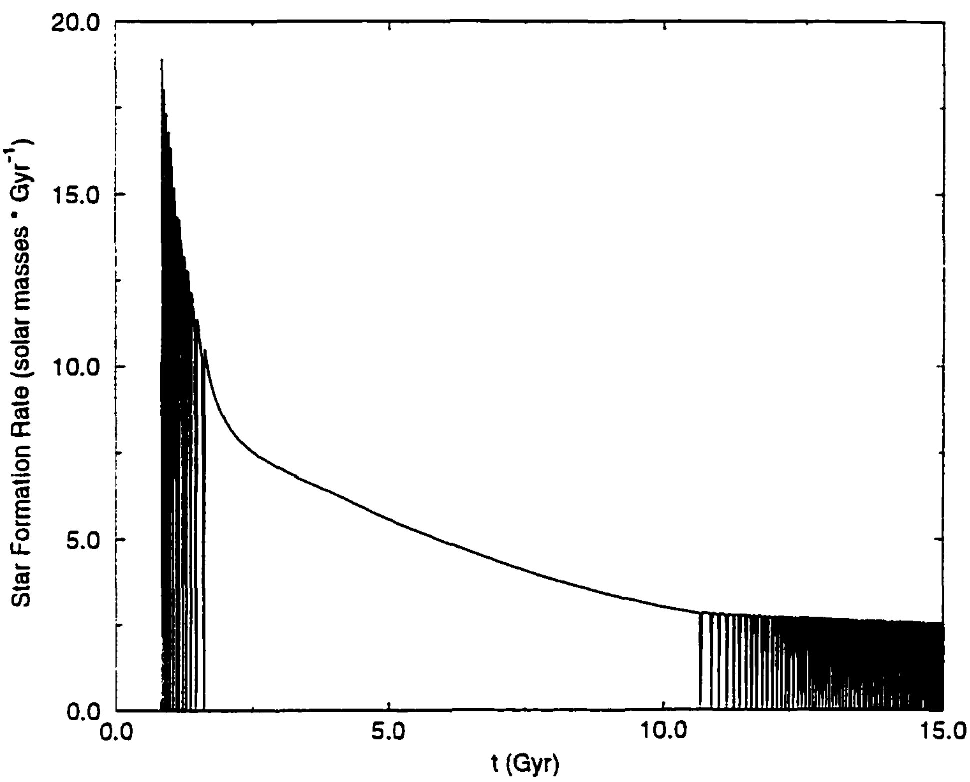

Figure 2.1: Plot of SFR against time for NICE. Note oscillatory behavior of ψ due to the inclusion of cutoff value of local gas density

SFR vs. time (Fig. 2.1) very similar to the same plot in Chiappini, Matteucci and Gratton (1996), Fig. 4.

2.2.3 Rate of Infall

For the infall rate, an exponentially decaying accumulation of primordial (big-bang) gas is assumed:

$$\dot{\sigma_t} = f(t) = A_{\rm inf} e^{\frac{-t}{\tau_d}}\, M_\odot\,{\rm Gyr}^{-1}$$

This expression is normalized to the boundary conditions

$$\begin{aligned} \sigma(0) &= 0 \\ \sigma(t_{\rm now}) &= 50 M_\odot \end{aligned}$$

giving

$$A_{\rm inf} = \frac{\sigma(t_{\rm now})}{\tau_d \left(1 - e^{\frac{t_{\rm now}}{\tau_{\rm disk}}}\right)}$$

This model for the infall rate is common to almost all the chemical evolution codes studied by Tosi (1996), and is based upon the assumption that the disk component of the Galaxy grew to many times its early value during the early phase of the evolution. The rate of infall is characterized by the timescale for disk formation, τ_d, and decreases to the present-day (nonzero) value. Observational constraints on the present infall rate (Chiappini, Matteucci and Gratton (1996), Timmes, Woosley and Weaver (1995), and references therein) place the current mass accumulation

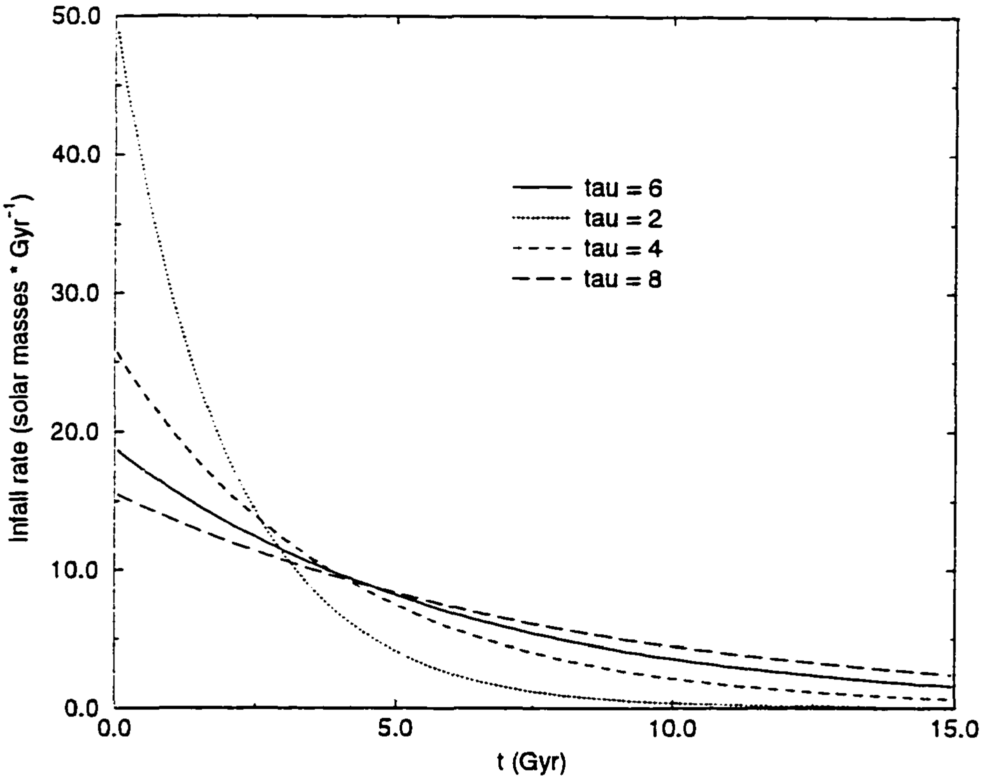

Figure 2.2: Graph of infall rates vs. time for different values of τ_d

on the order of 1 $M_\odot\,\mathrm{Gyr}^{-1}$. Rates of infall for varying values of τ_d are shown in Fig. 2.2, and the response of the star formation rate to this infall function is plotted in Fig. 2.3, with $M = 100 M_\odot$ to suppress the SFR cutoff.

As shown in Fig. 2.3, the SFR is peaked during times of rapid infall; we expect this, since high infall rates drive up the local gas density, which is the chief dependent variable in the star formation rate.

An exponential infall model is one of the simplest models to also solve the G-dwarf problem discussed earlier. The observed paucity of small metal-poor stars

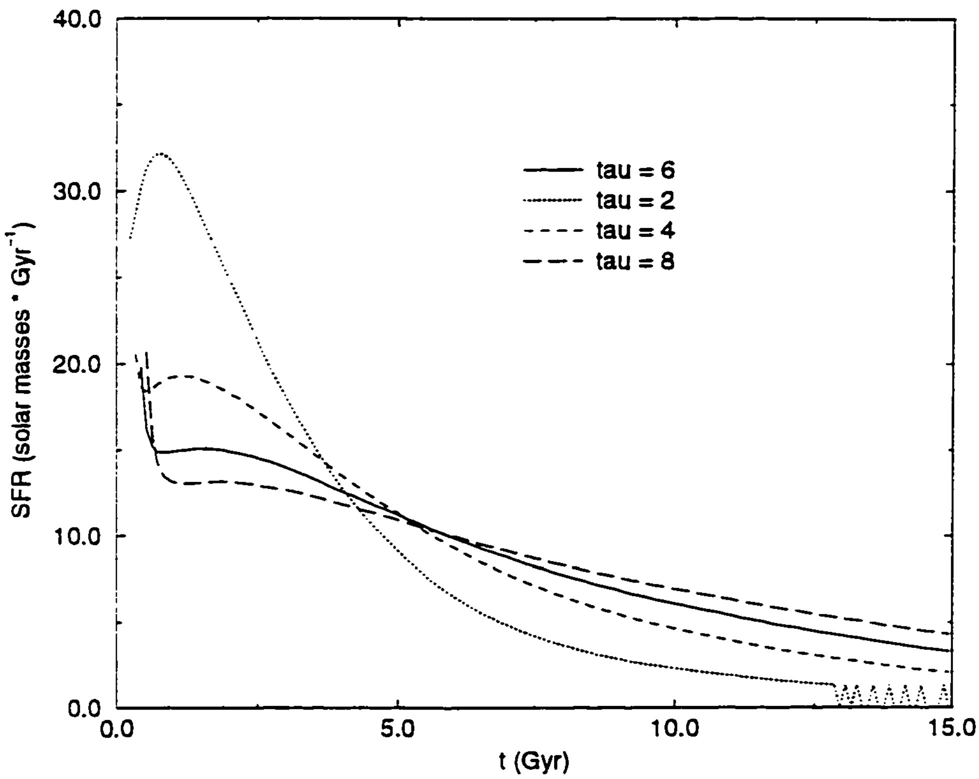

Figure 2.3: Graph of SFR against time for varying infall rates

conflicts with simple chemical evolution models with no infall and a large initial gas mass. Using the simple exponential model, the G-dwarf distribution predicted also closely mimics the observed quantities (Fig. 2.7).

2.2.4 Initial Mass Function

As introduced earlier, the IMF gives the fraction of stars that are formed in a given mass range. Salpeter (1955) gives a functional form for the IMF as

$$\phi(m) \sim m^{-(1+x)}$$

and this form has proved successful in many different evolutionary models up to the present day. His derived value for $x = 1.35$, and is typically normalized between the lower and upper mass limits in a given scheme. Clearly, in a given region of star formation, the initial mass function is sharply weighted in favor of low-mass stars. A good review of the techniques used in determining the IMF for the local stellar neighborhood is given in Tinsley (1980). There is some observational evidence for a change in slope of the IMF for massive stars above 10 $M_\odot$ (Tinsley (1980), Gibson and Matteucci (1997), Scalo (1986)), though Tsujimoto et al. (1997) finds that a singular slope is effective with an upper-mass cutoff of $50 \pm 10\, M_\odot$, implying that stars born with a mass above this threshold do not return an appreciable amount of material to the local interstellar medium, but instead trap the mass in a remnant such as a black hole. To examine both cases, the overall IMF mass fraction is normalized from 0.08 $M_\odot$ to 40 $M_\odot$ as follows:

$$1 = A_{\rm imf}\left(\int_{0.08}^{10} m\phi_1(m)\,dm + \int_{10}^{40} m\phi_2(m)\,dm\right)$$

where

$$\phi_1 = m^{-(1+x_1)}, x_1 = 1.30$$

$$\phi_2 = m^{-(1+x_2)}, x_2 = 1.90$$

giving

$$A_{\rm imf} = \left\{\frac{m_c^{1-x_1} - m_l^{1-x_1}}{1-x_1} + \frac{m_h^{1-x_2} - m_c^{1-x_2}}{1-x_2}\right\}^{-1}$$

where $m_l = 0.08M_\odot$, $m_c = 10M_\odot$, and $m_h = 40M_\odot$. Since the adopted yields of high-mass stars and Type II supernovae are from Woosley and Weaver (1995) (discussed in § 2.2.6), with ejected masses given up to 40 solar masses, I adopt this as the upper limiting mass for returning gas to the ISM. Results from NICE show a good match to observational parameters with a single-slope IMF ($x = 1.3$) and a large discrepancy in the oxygen abundance for a dual-slope IMF ($x = 1.9$ for $M > 10M_\odot$). Fig. 2.4 shows this discrepancy, with the dotted line indicating the present solar oxygen abundance.

The lines in Fig. 2.4 have a similar history to each other, but the abundance numbers are clearly different due to the lack of massive stars in the dual-slope model. Since oxygen is almost entirely generated in these massive stars, the overall production is deficient. This will justify future consideration of a single slope, $x_1 = x_2 = 1.3$, for the IMF.

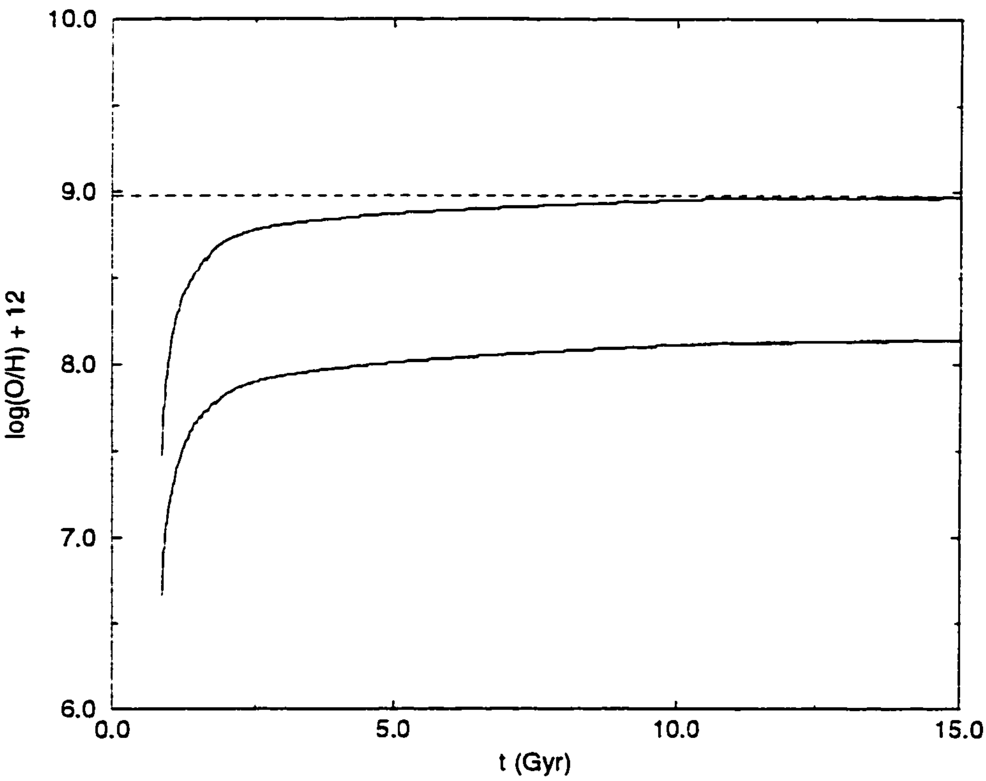

Figure 2.4: Calculated oxygen abundances with a single-slope ($x = 1.35$, upper line), and a dual-slope ($x = 1.9, M > 10M_{\odot}$, lower line.) The dashed line represents the current solar oxygen abundance.

2.2.5 Supernovae Rates and Yields

An important consideration in chemical evolution calculations is one regarding stellar death. The final phases of life are very different for high-mass (Type II supernova progenitors) as opposed to low-mass stars, as well as those lower-mass stars that are members of a binary system (Type Ia supernova progenitors). Since most of the heavy elements are generated in these processes, it is important to accurately calculate the rate of supernova explosions.

Type II supernovae (SNe) are the explosions of stars having, for this model, initial (main sequence) masses $8 < M/M_{\odot} < 40$. If we assume that all stars falling in this mass range undergo this explosion, then by counting the number of stars in this range, we also count the number of SNe. The number of explosions (per Gyr) is

$$R_{\rm II} = \int_{16}^{40} \psi(t - \tau_m)\phi(m)\, dm + (1 - C) \int_{8}^{16} \psi(t - \tau_m)\phi(m)\, dm$$

where again we must use the historical value of ψ. The meaning of the C parameter will be discussed below; for the moment imagine $C = 0$, so that the above is just a single integral over the massive stars. The amount of heavy elements released is taken from the tables of Woosley and Weaver (1995). These tables are an improvement over earlier work Woosley and Weaver (1986), which did not take into account the explosive nucleosynthesis of Si and S into iron. For this study, I also adopt the metallicity dependence of the yields given (0.01, 0.1, and 1 times solar abundances), so that the yields are slightly different as the overall metallicity of the galaxy increases. These are given in Appendix B, according to Table 2.1.

Table 2.1

Appendix B Notation	Woosley and Weaver (1995) Yields
He4ww_1	Helium, $Z = Z_{\odot}$
He4ww_0_1	Helium, $Z = 0.1Z_{\odot}$
He4ww_0_0_1	Helium, $Z = 0.01Z_{\odot}$
N14ww_1	Nitrogen, $Z = Z_{\odot}$
N14ww_0_1	Nitrogen, $Z = 0.1Z_{\odot}$
N14ww_0_0_1	Nitrogen, $Z = 0.01Z_{\odot}$
O16ww_1	Oxygen, $Z = Z_{\odot}$
O16ww_0_1	Oxygen, $Z = 0.1Z_{\odot}$
O16ww_0_0_1	Oxygen, $Z = 0.01Z_{\odot}$

Table 2.1: Key to type II SN yields given in Appendix B

The yields given represent the mass of each element ejected (in solar masses) during a mass-dependent SN event.

Type Ia SN are thought to be the result of carbon deflagration in carbon-oxygen white dwarfs in binary systems. The standard mechanism features a white dwarf accumulating material from its companion at a rate that the Chandrasekhar mass limit is breached, resulting in an explosion. The yield of elements resulting from type Ia events is roughly independent of the mass of the individual progenitor stars, so the strategy is simply to count the number of type Ia events. Yields are taken from Nomoto et al. (1984), the famous W7 model (see Table 2.2). Some recent refinements have been made to the W7 model (Thielemann et al. (1993)), but they are typically adjustments to the yields of elements outside the current study.

Table 2.2

Element	Yield ($M_\odot$)
H	0.0
He	0.0
N	0.0
O	0.143
S	0.084
Fe	0.717

Table 2.2: Yields from type Ia supernovae, in solar masses, W7 model (Nomoto et al. (1984))

Stars of less than 8 solar masses are thought to end their lives as white dwarfs; to calculate the type Ia rates, it is first necessary to count the stars below this mass threshold. Since these SNe are the result of binary systems, this means it is necessary to count all the stars of less than 16 solar masses, and then apply a binary distribution function. The form of this distribution function is taken from Greggio and Renzini (1983),

$$f(\mu) = 2^{1+\gamma}(1+\gamma)\mu^{\gamma} = 24\mu^2 \text{ with } \gamma = 2$$

where μ is the ratio of the less massive (secondary) component of the binary system to the more massive (primary). $f(\mu)$ is normalized over the interval $(0, \frac{1}{2})$. We will also enforce a lower limit of $3M_\odot$ to the initial mass of the star that eventually produces a type Ia SN, to ensure that the final white dwarf eventually reaches the Chandrasekhar mass due to accretion.

This case is surely oversimplified; there are many additional factors that determine when and if a binary white dwarf system will explode, such as the distribution of orbital separation and the inclusion of perturbations of many-star systems. These factors have been crudely incorporated into a "tuning parameter" C, consistent with previous studies (Timmes, Woosley and Weaver (1995), Chiappini, Matteucci and Gratton (1996), Matteucci and François (1989), Matteucci (1986)). This factor was mentioned previously in the calculation of type II SN rates, to exclude those stars in the overlapping mass range that were actually binary systems destined to produce type Ia events. This is an overall "efficiency" parameter that is tuned according to present iron abundances and observed type Ia rates, and is meant to indicate what percentage of qualified systems actually undergo type Ia events. A typical value for C that fits observed SN rates and iron abundances is $C = 0.05$, and the congruence of this choice with observations is shown in § 2.3 and Fig. 2.8.

2.2.6 Yields from Intermediate-Mass Stars

In the studies mentioned earlier in this thesis, the source for yields for intermediate-mass stars was Renzini and Voli (1981). Recently, however, at least two new publications of yields from stars of mass $1 < M/M_{\odot} < 8$ have been completed. These two that will be used and compared are Buell (1997) and van den Hoek and Groenewegen (1996). Note that the data in Buell (1997) are given in solar masses, while the data in van den Hoek and Groenewegen (1996) are given as a fraction (so that they must be multiplied by the mass of the star in order to compare with Buell (1997)). Details of the methods used to calculate the yields can be found in the respective references; however, it seems that the Buell yields are a more sophisticated treatment due to a consideration of the strength of the thermal pulse in the 3rd dredge-up phase of stellar evolution, as well as a non-parameterized treatment of hot-bottom burning and a different mass-loss method. In any case, here I shall briefly compare the nitrogen yields and subsequent evolution, and then choose the Buell yields to use exclusively throughout the rest of this thesis. Once the systematically differential behavior is noticed, it will suffice to use a consistent database for yields.

The yields from each source are tabulated in Appendix B, in the `nice_yields.hh` file. A key to translating between the notation in the code and physical parameters is given in Tables 2.3 and 2.4.

Table 2.3

Appendix B Notation	Element	Metallicity
He4b_15	Helium	[Fe/H] = -1.5
N14b_15	Nitrogen	[Fe/H] = -1.5
O16b_15	Oxygen	[Fe/H] = -1.5
He4b_10	Helium	[Fe/H] = -1.0
N14b_10	Nitrogen	[Fe/H] = -1.0
O16b_10	Oxygen	[Fe/H] = -1.0
He4b_05	Helium	[Fe/H] = -0.5
N14b_05	Nitrogen	[Fe/H] = -0.5
O16b_05	Oxygen	[Fe/H] = -0.5
He4b_02	Helium	[Fe/H] = -0.2
N14b_02	Nitrogen	[Fe/H] = -0.2
O16b_02	Oxygen	[Fe/H] = -0.2
He4b_01	Helium	[Fe/H] = -0.1
N14b_01	Nitrogen	[Fe/H] = -0.1
O16b_01	Oxygen	[Fe/H] = -0.1
He4b_00	Helium	[Fe/H] = 0.0
N14b_00	Nitrogen	[Fe/H] = 0.0
O16b_00	Oxygen	[Fe/H] = 0.0
He4b_p1	Helium	[Fe/H] = 0.1
N14b_p1	Nitrogen	[Fe/H] = 0.1
O16b_p1	Oxygen	[Fe/H] = 0.1
He4b_p2	Helium	[Fe/H] = 0.2
N14b_p2	Nitrogen	[Fe/H] = 0.2
O16b_p2	Oxygen	[Fe/H] = 0.2

Table 2.3: Key to yield data given in Appendix B. From Buell (1997)

Table 2.4

Appendix B Notation	Element	Metallicity
He4v_z_3	Helium	log(Z) = -3.0
N14v_z_3	Nitrogen	log(Z) = -3.0
O16v_z_3	Oxygen	log(Z) = -3.0
He4v_z_2_4	Helium	log(Z) = -2.4
N14v_z_2_4	Nitrogen	log(Z) = -2.4
O16v_z_2_4	Oxygen	log(Z) = -2.4
He4v_z_2_09	Helium	log(Z) = -2.09
N14v_z_2_09	Nitrogen	log(Z) = -2.09
O16v_z_2_09	Oxygen	log(Z) = -2.09
He4v_z_1_7	Helium	log(Z) = -1.7
N14v_z_1_7	Nitrogen	log(Z) = -1.7
O16v_z_1_7	Oxygen	log(Z) = -1.7

Table 2.4: Key to yield data given in Appendix B. From van den Hoek and Groenewegen (1996)

During the integration over all masses that occurs within each time step, the yield database is queried and a yield is returned via linear interpolation between values given in the database. Different sets of yields are chosen based on the value of the local metallicity or [Fe/H] value, since the yields (especially secondary elements such as nitrogen) are dependent upon the initial metal content of the progenitor star.

The dependence of the nitrogen yields on initial metal content can be seen in Figs. 2.5, 2.6, where in general nitrogen production is deficient in small stars with low initial metallicity. This holds true for both sets of yields. It does not seem to hold, interestingly, for stars of mass $> 3.5-4M_{\odot}$. This is roughly the regime where hot-bottom burning becomes an important convective mechanism, and is also the point at which the primary production of nitrogen is an appreciable fraction of the total (Buell (1997)). It is perhaps not surprising, since the secondary mechanism produces an amount of nitrogen proportional to intial seed elements, and so the yield should decline along with the decline in the seed. As motivation for future analysis, consider an initially unenriched cell of gas. After the first generation of stars is formed, the high-mass stars will return primary nitrogen back to the ISM. The secondary (and metal-dependent) component should be returned only after the lower-mass stars have evolved, and therefore should be delayed in time. The timescale for the delayed release of secondary nitrogen is approximately equal to the lifetime of a 3-4 solar mass star, or about 200 million years.

This is an important result, and will be considered in more detail both observationally and in the light of chemical evolution modelling in subsequent sections.

2.2.7 Solar Abundances

Often in this thesis, the notation

$$\frac{[X_1]}{[X_2]}$$

is used, where X_1 and X_2 are certain elements. The use of the square brackets represents the logarithmic difference in abundance between the element in the numerator and the element in the denominator, compared to the standard solar value for this difference. A standard set of solar values is given in Anders and Grevesse (1989), (with extensions from Grevesse and Noels (1993)), and is given in Table 2.5.

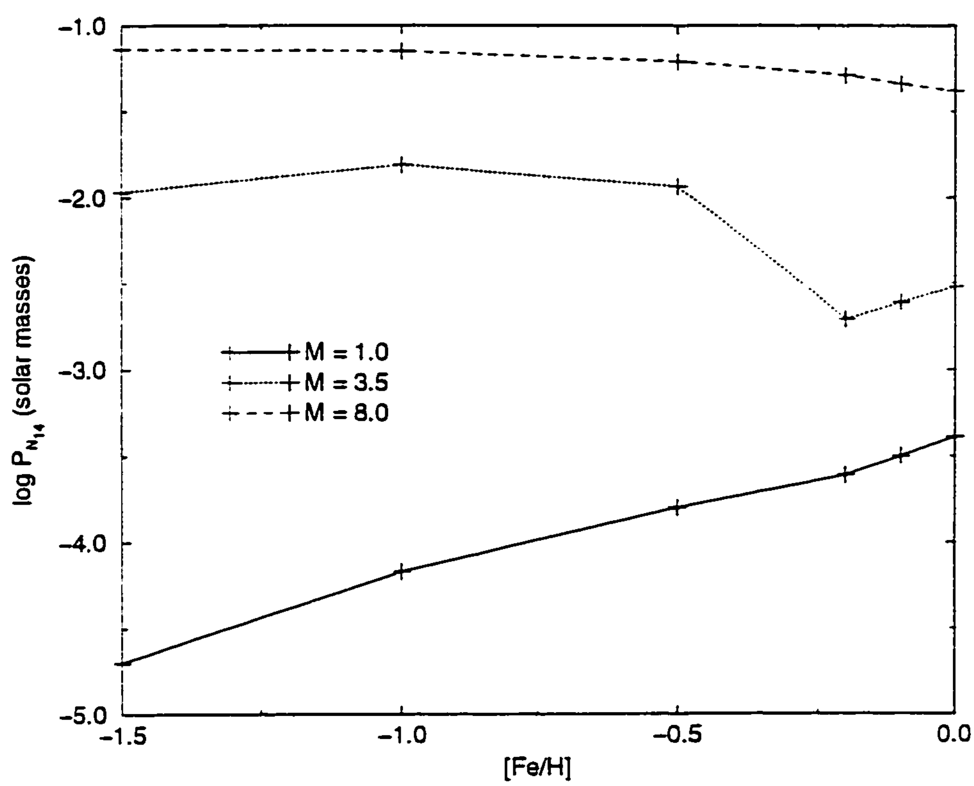

Figure 2.5: Plot of the yield (in solar masses) against metallicity. The metallicity reflects the logarithmic difference between calculated (Fe/H) and solar (Fe/H) at stellar birth. Several lines are shown representing different initial ZAMS masses for the stars. Yields from Buell (1997)

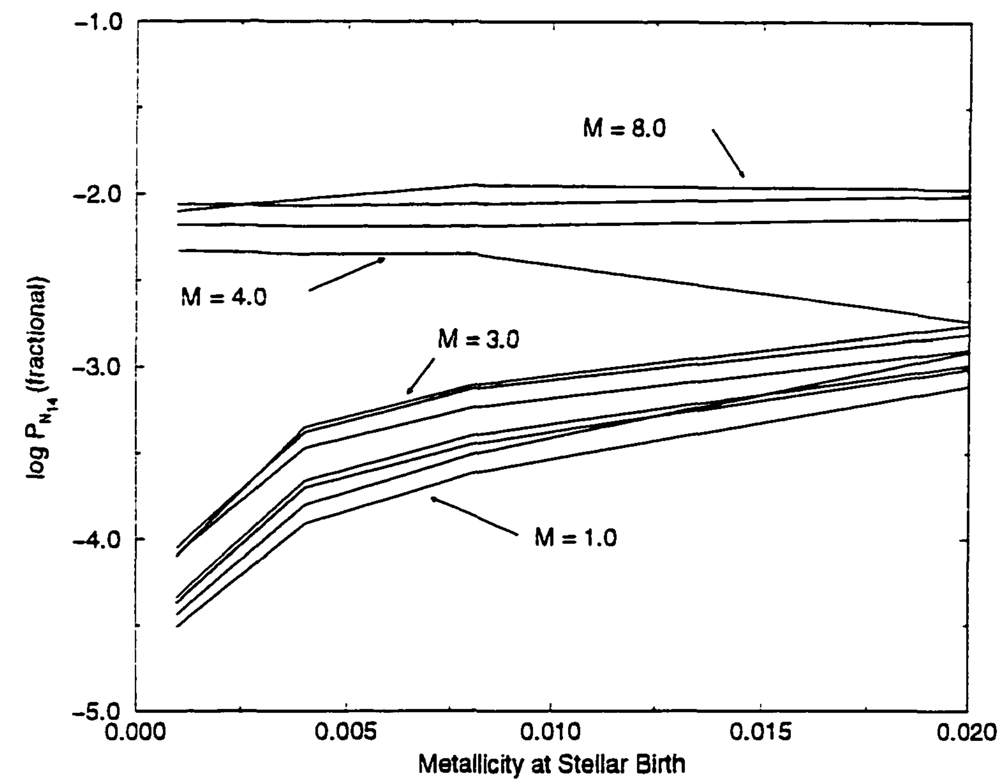

Figure 2.6: Plot of the yield (in solar masses) against metallicity. The metallicity reflects the combined mass fraction of heavy elements at stellar birth. The solar value for metallicity is ≈ 0.02. Several lines are shown representing different initial ZAMS ages for the stars. Yields from van den Hoek and Groenewegen (1996)

Table 2.5

Z	Element	X/H	log(X/H) + 12
1	H	1	12.00
2	He	0.1	11.00
7	N	9.33E-05	7.97
8	O	7.41E-04	8.87
16	S	1.62E-05	7.21
26	Fe	3.24E-05	7.51

Table 2.5: Solar abundance values used in this thesis; sources are Anders and Grevesse (1989), Grevesse and Noels (1993)

This table of solar values is also used in the studies with which we wish to compare, so systematic error should not accumulate due to this process.

2.3 Testing the NICE Code

There are four primary tests against observed quantities for this model of chemical evolution: Reproduction of the G-dwarf distribution, accurate supernove rates (for type Ia and type II), correct form of the O/Fe relation (including other age-metallicity relations), and present ratios of elemental abundances. Details of these tests follow:

2.3.1 The G-dwarf test

As outlined before, the relevance of the distribution of metal-poor dwarf stars became important during the first attempts at analytic and numerical chemical evolution. In the simple model, with no inflow and a large reservoir of available gas for star formation, the form of the IMF leads to an overproduction of small stars with little or no heavy-element pollution that live to the present era. Hence a large sample of these stars carries a "memory" of the star formation history when the galaxy was young.

The natural solution to the problem is to postulate an initially small reservoir of gas, with a continuous infall of primordial material. In this way, small numbers of stars are formed initially, while the local environment is enriched with new metals from recent supernovae. Thus the population of metal-poor stars is suppressed. Using the aforementioned prescription for infall, the G-dwarf distribution calculated by NICE is compared to the observed population in Fig. 2.7; the calculated distribution agrees satisfactorily with the observed. Note in this plot the histograms for both quantities are normalized to the total number of G-dwarf stars ever produced. The number of dwarfs formed in a given time step dt is calculated as

$$N = \int_0^{0.9} \psi(t)\phi(m)\, dm\, dt$$

where the upper limit of $0.9 M_\odot$ is chosen as the most massive star not to have evolved by the present era.

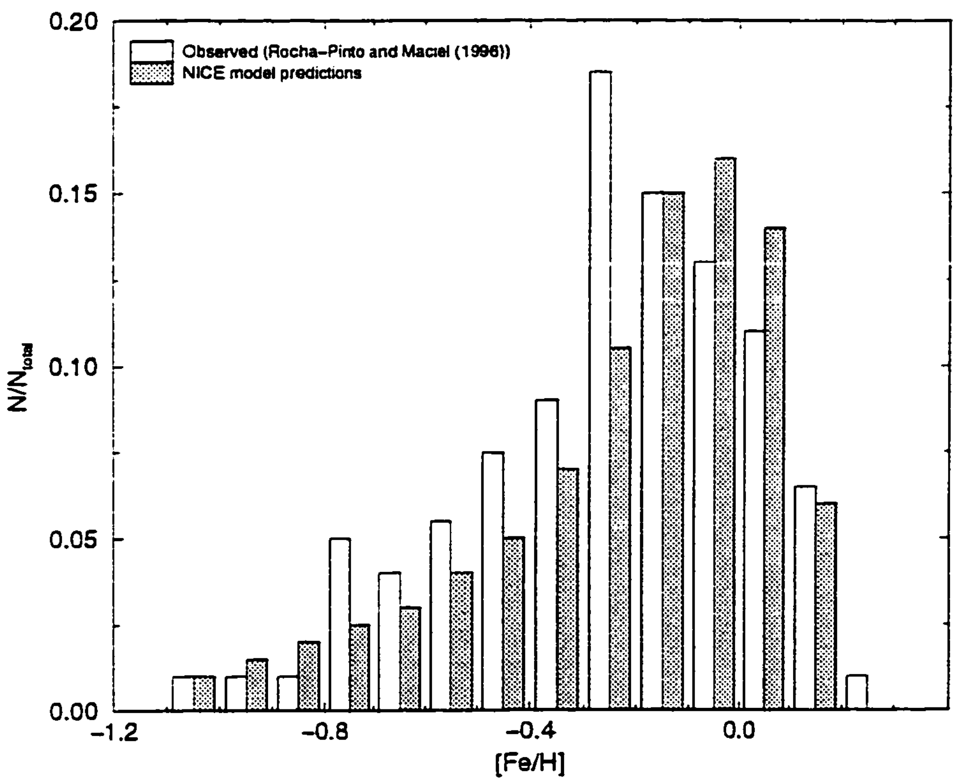

Figure 2.7: Plot showing number of G-dwarfs observed (Rocha-Pinto and Maciel (1996)) compared with NICE model predictions

2.3.2 Predicted Supernovae Rates

The present SN rates in the galactic disk were estimated by van den Bergh and McClure (1994) as about 2.4-2.7 century^{-1} for type II, and 0.3-0.6 century^{-1} for type Ia. The total SN rate, then, should be on the order of 3 per century, with a ratio of type II to type Ia events of about 5. The calculated rates are shown in Fig. 2.8, and behave as expected. The type II rates roughly trace the star formation history, as the delay between massive star birth and death is small compared to changes in the SFR. These events decline in time along with the decline in the gas mass fraction. Type Ia explosions, on the other hand, show a delay due to the fact that the progenitors of these events are intermediate-mass stars with longer lifetimes. The temporal behavior of type Ia SNe is almost independent of the details of the star formation rate due to these longer evolutionary timescales.

To compare with published observational results, an integration over the mass of the disk of the galaxy is performed. This integration, for simplicity, takes the form of a simple mass scaling. Assuming a disk mass of $1.0 \times 10^{11} M_{\odot}$, the NICE model calculates a type Ia rate of 0.66 century^{-1} and a type II rate of 2.5 century^{-1}. Both rates and their ratio are acceptably close to the observed quantities.

2.3.3 Age-Metallicity Relation

Edvardsson et al. (1993) present a set of observational data that relates [Fe/H] to elapsed age in the galactic disk. In general, we expect the [Fe/H] ratio to rise gently over time as the type Ia SNe manufacture and release iron into the ISM. This rate of iron deposition should decrease with time as the star formation rate

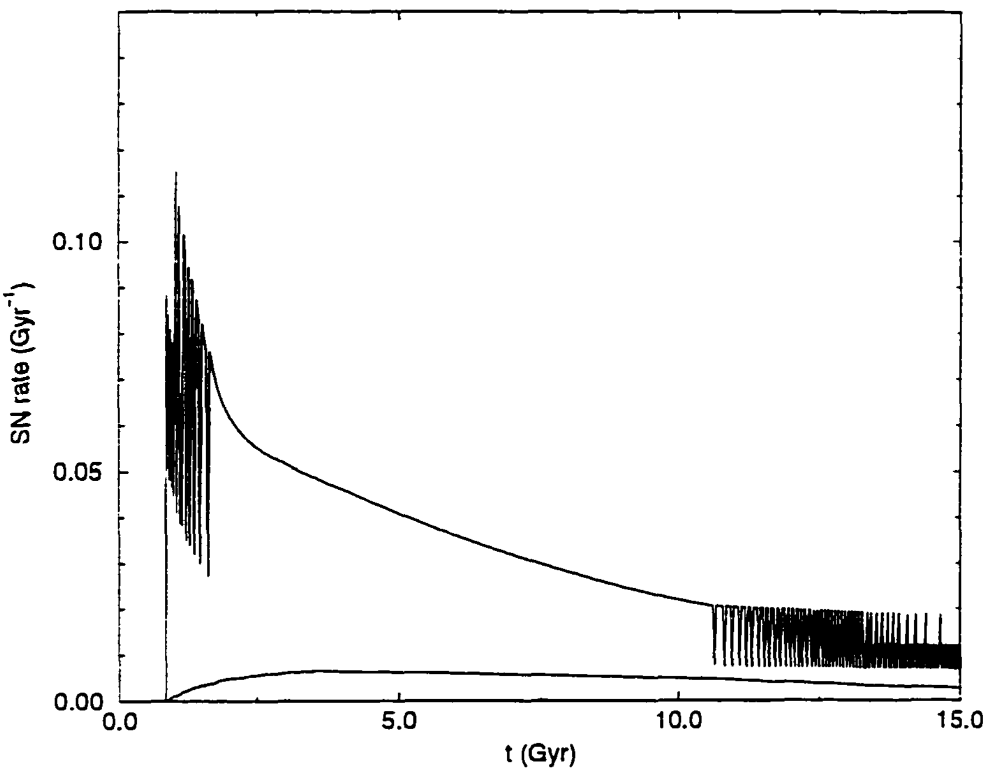

Figure 2.8: Calculated supernovae rates, segregated into Type Ia events (lower curve) and Type II events (upper curve).

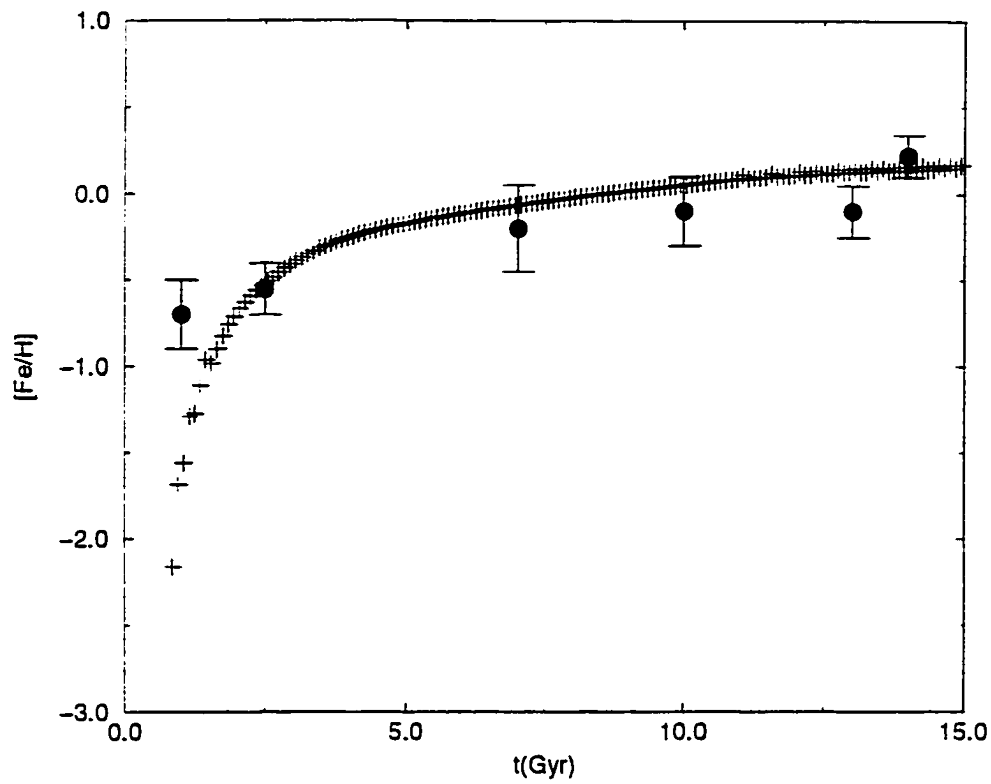

Figure 2.9: Calculated Age-Metallicity Relation is shown by the solid line. The points are selected from Edvardsson et al. (1993), showing the uncertainty in [Fe/H].

declines as well. These results are shown in Fig. 2.9, again with good correlation with observations.

It must be said, however good the fit with these observations, the age-metallicity relation is not very constraining, and the calculated line is very robust with changes in input parameters. Further, the Edvardsson data may be biased with respect to [Fe/H], in the sense that some metal rich stars have been excluded by a temperature cutoff (Nissen (1995)). The scatter in the data is probably real, however, and should motivate further study into chemical evolutionary models that do not assume instantaneous mixing of ejecta into the local ISM. Few of these studies have been undertaken.

2.3.4 Abundance Ratios

The final (and possibly the most visible) test of a chemical evolution code is the prediction of elemental abundance ratios. For brevity, Table 2.6 is presented, with the calculated abundance ratios at the time of solar birth as compared with the measured solar values.

Table 2.6

Z	Element	Calculated	Measured
1	H	12.00	12.00
2	He	10.94	11.00
7	N	7.93	7.97
8	O	8.92	8.87
16	S	7.36	7.21
26	Fe	7.45	7.51

Table 2.6: Comparison of calculated elemental abundance ratios with measured quantities. The ratios are given as $\log(X/H) + 12$, with observed values from Anders and Grevesse (1989).

Following Timmes, Woosley and Weaver (1995) and Chiappini, Matteucci and Gratton (1996), where abundance values falling within a factor of two inside the observed solar values are considered to be in good agreement, it is noted that this model produces satisfactory abundance ratios. We will examine the relationships between these ratios and time in Chapter 4, and apply them to recent observations of these ratios in extragalactic HII regions.

2.4 Summary

In this chapter, a theoretical framework was developed for a chemical evolution model of the galaxy. This model does not assume instantaneous recycling, nor is it a closed-box model. The initial assumptions include an exponentially decreasing infall of primordial matter onto the galactic disk (with no native gas present), a Schmidt star formation rate with a low-density threshold, the (approximately) Salpeter initial mass function with a single slope for all mass ranges, and a standard prescription for the inclusion of type Ia supernovae. The latter are assumed to originate with a binary system where one of the members is an accreting white dwarf. The production of the elements from evolving stars is taken from three sources: Buell (1997) for yields of intermediate-mass stars, Woosley and Weaver (1995) for yields of massive stars (type II SN), and Nomoto et al. (1984) for the production of elements in type Ia SN.

By considering various analytic forms for input parameters, a numerical model was constructed that agrees well with constraining observations of the solar neighborhood. The code was tested against the metal-poor dwarf population (the G-dwarf test), observed supernovae rates, and solar values for elemental abundance ratios. The observed age-metallicity relation was also satisfied, although this was not found to be terribly constraining due to the (probably real) scatter in the data.

We now turn to observational abundance measurements of HII regions in order to apply NICE to real phenomena and understand some of the factors affecting nitrogen processing in spirals.

Chapter 3

Nitrogen Abundance Determinations

3.1 Introduction

Abundance gradients along the radii of galaxies as determined from observations of extragalactic HII regions are evident for some elements, most notably oxygen, for many spirals as shown in the compilations of Vila-Costas and Edmunds (1992) and Zaritsky et al. (1989, 1990). Some factors thought to be responsible for these gradients include dynamical flows (infall, outflow, and fountains) in the disks of galaxies and systematic variations of star formation rates across the disk.

There is also evidence of a gradient in the abundance of nitrogen with respect to oxygen (N/O) along spiral disks (Vila-Costas and Edmunds (1993)). An understanding of the spatial distribution and temporal production dependence of nitrogen would be valuable, and indeed is one of the goals of this thesis. This element, in contrast to elements such as iron and oxygen, i.e. the traditional tracers of metallicity and chemical evolution, is manufactured in different nuclear processes, probably predominantly in stars of less than 8 $M_\odot$. In particular, the question of whether nitrogen is produced as a primary or secondary element is still open. If nitrogen is secondary, meaning that the amount of nitrogen produced by a star depends upon the initial abundance of carbon and oxygen, we would expect the ratio N/O to be proportional to O/H. N/O would be a constant for a primary origin of nitrogen if its production is independent of "seed" elements. These basic behaviours hold for a "closed box" model with instantaneous recycling. They will be modified in more realistic models (Serrano and Peimbert (1983), Matteucci (1986), this thesis) which allow both for delayed release of nitrogen and accretion of gas onto the galactic plane (see Chapter 2 for details on the numerical model used in this study). Serrano and Peimbert were able to find models with a fairly shallow N/O gradient even with predominantly secondary nitrogen production. It seems likely that the delayed release is crucial here, since the presence of accretion in the instantaneous recycling approximation always tends to *steepen* the N/O versus O/H relation (Edmunds 1990). There is some evidence that nitrogen shares both primary and secondary components (Matteucci (1986), Vila-Costas and Edmunds (1993), Buell (1997)), though the relative importance of each is not certain. This question in particular will be further addressed in Chapter 4.

Generally, the abundances of the elements in nebulae can be derived from the measurement of the relative strengths of their spectral emission lines. We further assume that, due to the low matter and electron densities in these clouds, they are "optically thin" (transparent) to the emission lines; therefore, we need not consider blanketing and blocking in the measurements. The elements to be considered in this study, nitrogen and oxygen, have strong spectral lines in the visible region of the spectrum. Once the intensity of radiation is measured coming from a given ion, the following relation is used to determine the number density of the ion, N_i:

$$I_\nu = \frac{1}{4\pi}\int N_i N_e h\nu\, q_{1,2}(T)\, b\, ds \tag{3.1}$$
$$= \frac{1}{4\pi}\int N_i N_e h\nu \frac{8.63\times 10^{-6}}{\sqrt{T}}\frac{\Omega(1,2)}{\omega_1} e^{-\frac{\chi}{kT}}\, b\, ds \tag{3.2}$$

where b is the fraction of excitations to level 2 that are followed by emission of a photon in the line observed. Since this gives the number density for a particular ion, in a rigorous sense we need observations of lines originating in all ionic stages for a particular element. In practice, however, this is never achieved. Highly ionized stages of a particular element exist, if at all, only very close to the ionizing source. The physical extent of these regions is small, and that coupled with the high energies associated with the de-exciting electrons makes these lines both weak and out of the visible wavelength range. Fortuitously, for oxygen there exist sets of visible spectral lines for two stages of ionization. The approximation that

$$\frac{N(O^{++})}{N(H)} + \frac{N(O^{+})}{N(H)} \approx \frac{N(O)}{N(H)}$$

is good in low-excitation phenomena such as HII regions. It can be seen that in the previous relation, the intensity of the observed spectral line is primarily dependent on two environmental parameters: the local electron density and the local electron temperature. Both of these can be inferred from ratios of elemental lines. For HII regions, the temperature effect is the stronger of the two, and is discussed below.

While it is desirable to determine N/O ratios directly from observations of HII regions without having to resort to detailed photoionization model analyses, the direct approach is often hampered by the absence of temperature-sensitive auroral lines such as [NII] $\lambda5755$ and [OIII] $\lambda4363$, especially in metal-rich nebulae where these lines are not excited to observable levels due to the relatively low gas temperatures. Ideally, one obtains an electron temperature for the emission region by observing the ratio of intensities of pairs of emission lines. These emission lines should be the result of electron transitions from two levels with considerably different excitation energies. Oxygen and nitrogen (specifically [OIII] and [NII]) are good examples of this mechanism, as each has energy level structures that result in emission lines from two different upper levels with considerably different excitation energies. A simple energy-level diagram is given in Fig. 3.1 for [NII]. Electrons may be collisionally excited from the ^3P level to either $^1D_2$ or $^1S_0$. The latter energy level results either in a photon at $\lambda5755$ or $\lambda3063$. Any transition $^1S_0 \rightarrow ^1 D_2$ will then result in photons with wavelengths of either $\lambda6583$ or $\lambda6548$. The ratio of intensities of the latter two lines is simply the ratio of the transition probabilities, which will be approximately constant. If the surrounding electron density is sufficiently high, it is possible for collisional de-excitation to populate the lower levels, but this density threshold occurs for $N_e \sim 10^5\,\mathrm{cm}^{-3}$, well above the typical HII region densities of $10 - 100\,\mathrm{cm}^{-3}$. It can be seen, then, that the ratio of intensities of these lines directly reflects the population of the two levels, which in turn is directly related to the collisional excitation rate (electron temperature).

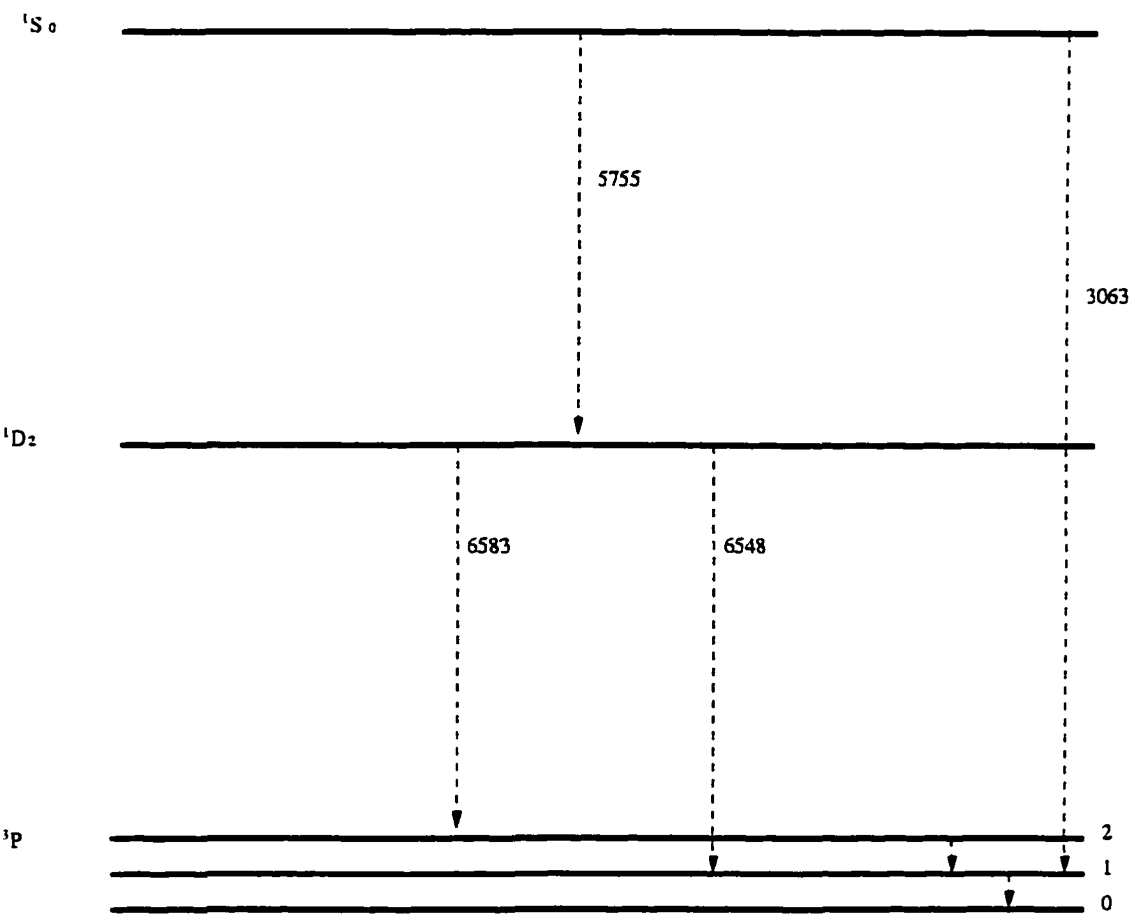

Figure 3.1: Energy level diagram for the [NII] ion in ground $2p^2$ configuration. Splitting of the ^3P term is exaggerated for clarity. Only the strongest transitions are indicated. From Osterbrock (1988).

This relation is given in § 3.2.1 and utilized in the analysis of photoionization models. Additionally, these transitions occur in the observable wavelength region, so that determining electron temperatures for a given emission region should not be difficult. In practice, however, the λ5755 line (for [NII]) and λ4363 line (for [OIII]) are relatively weak, and difficult to discern above the continuum.

Thus, the purpose of this chapter is to introduce a new method for determining N/O in HII regions directly from observations of [OII] λ3727, [OIII] $\lambda\lambda$4959,5007, and [NII] λ6584 and in the absence of measured strengths of the temperature-sensitive lines. Our method is based on the relationship between [NII] electron temperature and the sum of [OII] and [OIII] line strengths which we derive using a grid of photoionization models. This work was originally published in Thurston, Edmunds and Henry (1996), but I present a new calibration of this method to include observations of both high- and low-metallicity HII regions.

In § 3.2.1 we develop and test our new algorithm, while in § 3.2.2 we demonstrate its application with a sample of well-observed spiral galaxies. The results are shown for a full sample of ten spirals as well as for the sample sorted into early and late morphological types. Finally, a summary is presented in § 3.5.

3.2 Method

3.2.1 The Algorithm

To obtain elemental abundance ratios, one traditionally observes a set of emission lines for a given element, preferably from more than one ionization state. If the electron temperature in the emission region is known, one can utilize an n-level atom calculation to solve for the electron level populations and derive the ionic abundance ratio desired. Then, using standard relations between observed ions and element abundances (ionic correction factors) the abundances are determined.

We desire to develop a simple procedure for determining N/O abundance ratios directly from HII region line strength observations which at the same time avoids the need for having to infer electron temperatures explicitly from observed lines, since the auroral lines needed for such temperature determinations are often unavailable. We begin by constructing a grid of photoionization models, using the code CLOUDY (Ferland (1990)). CLOUDY is a numerical photoionization code that computes the temperature and ionization structure for the entire nebula. The input parameters for CLOUDY include the effective ionization temperature of the central star in the nebula, electron density, and elemental abundances. The output includes the emission spectrum for a wide range of emission lines. In this study, the range of input abundances for the grid is $-1.15 < [N/O] < 0.5$ and $-2.0 < [O/H] < 0.50$. Here we use the standard square bracket notation for logarithmic ratios normalized to their solar values (Anders and Grevesse (1989)). Our models were computed with stellar effective temperature set at 40,000 K and utilizing Mihalas (1972) stellar atmospheres, a density of 10 cm^{-3}, and an ionization parameter of $\log U = -3$. Note that this is a slightly different ionizing temperature (40,000 K vs. 35,000 K) than the one used in Thurston, Edmunds and Henry (1996). The new temperature calibration is discussed further below, as well as the overall effect as compared to the earlier reference. All other elements were held at solar levels save the refractory elements (Na, Mg, Al, Si, Ca, Fe, Ni), which were depleted relative to the others by a factor of 10. We then use the model results to derive a relation between the nebular [NII] electron temperature and oxygen line ratios.

Fig. 3.2 illustrates the relation between the electron temperature in the [NII] emission region within the model and $\log R_{23}$, where the quantity R_{23} is defined as a ratio of observed line strengths:

$$R_{23} \equiv \frac{[\mathrm{OIII}]\lambda5007 + [\mathrm{OIII}]\lambda4959 + [\mathrm{OII}]\lambda3727}{H_\beta}$$

The [NII] temperatures were calculated from model emission lines of [NII] $\lambda\lambda6548$, 6583, and [NII] λ5755 using the theoretical description in Osterbrock (1988):

$$\frac{j_{\lambda 6548} + j_{\lambda 6583}}{j_{\lambda 5755}} = \frac{6.91 e^{\frac{2.5\times 10^4}{T}}}{1 + 2.5 \times 10^{-3} \frac{N_e}{\sqrt{T}}} \tag{3.3}$$

This equation was analyzed graphically, and a polynomial fit was found to invert the relation $J(T) \rightarrow T(J)$ (J represents the ratio of intensities). The emission lines for determining R_{23} were taken directly from model line strength predictions.

The relation between R_{23} and [NII] temperature is shown in Fig. 3.2, where points common to a dashed line are for a fixed O/H but varying N/O, while the sets of dashed lines represent varying O/H. Abundance ranges for [N/O] and [O/H] are as given above. Note that by tracing a given dashed line (constant O/H) from low N/O on the right to high N/O on the left we see that the N/O level significantly affects the resulting $\log R_{23}$ ratio without a correspondingly large variance in the electron temperature. This source of uncertainty in using $\log R_{23}$ to trace oxygen abundance has been pointed out before (Henry *et al* (1994)) and is further mentioned below.

Note that there is not a single functional relationship between $\log R_{23}$ and the electron temperature. This is fundamentally due to the relationship between $\log R_{23}$ and the oxygen abundance, which is shown in Fig. 3.8. The correspondence between oxygen abundance and a given value of R_{23} is non-unique. As values of O/H decline, the gas temperature rises and emission from forbidden lines increases. Below about [O/H]=0.1, however, the paucity of emitters determines line production, and the emission is reduced (see Pagel *et al* (1979), and Fig. 3.8 below). We therefore describe the behavior of this relationship in two regimes, called the *low-metallicity* regime (upper part of Fig. 3.2) and the *high-*

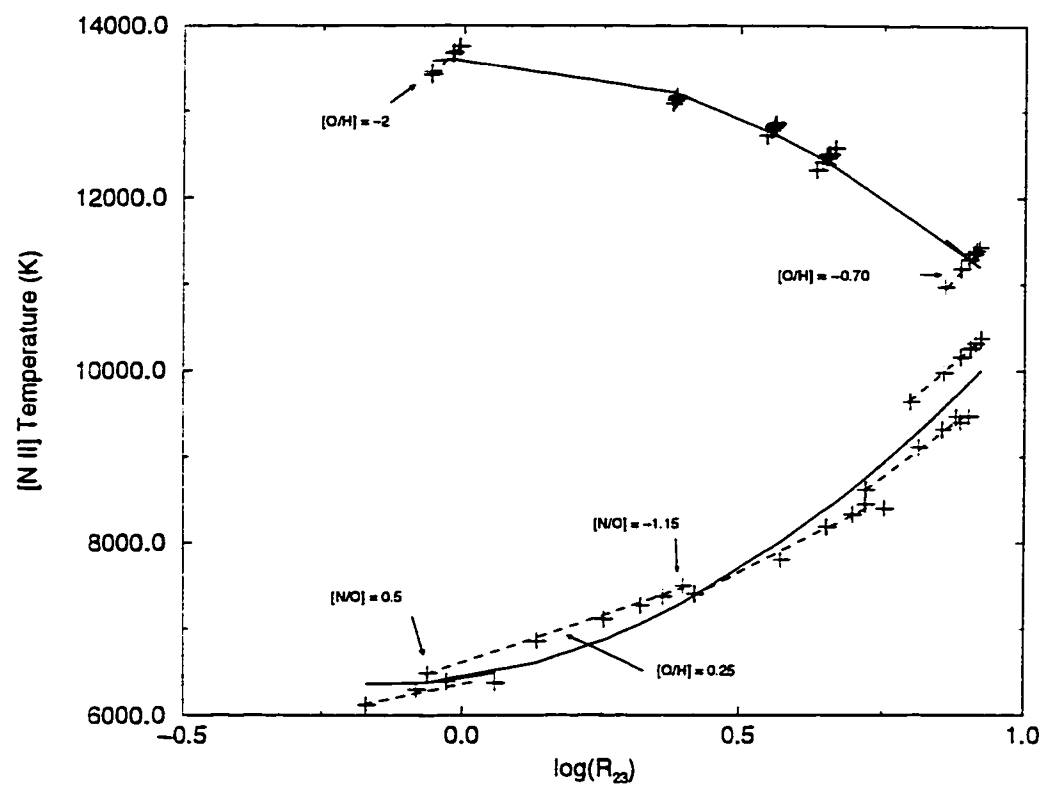

Figure 3.2: A plot of [NII] electron temperature versus logR_{23} for a grid of photoionization models spanning broad abundance ranges in N/O and O/H (see text) for a central star temperature of 40,000K. The plotted points represent individual models, where those connected by the same dashed line share a common O/H input abundance but different N/O input abundance ratios. N/O decreases from left to right along a dashed line, as indicated by the arrows. [O/H] abundances range from 0.50 for the lower leftmost dashed line to -2.0 for the dashed line in the upper left part of the plot. The solid lines show a least-squares fit to the points for both the low- and high-metallicity regions.

metallicity regime (lower part of Fig. 3.2). Least-square fits to the model results are shown with the solid curves and can be represented by the polynomials

$$t_{\rm II} = 6426 + 944(\log R_{23}) + 3178(\log R_{23})^2 \text{ for [O/H] } \geq 0.1 \tag{3.4}$$

for the high-metallicity region, and

$$t_{\rm II} = 13604 + 122(\log R_{23}) - 2977(\log R_{23})^2 \text{ for [O/H] } \leq 0.1 \tag{3.5}$$

for the low-metallicity region. Here, $t_{\rm II}$ is the [NII] temperature (in units of 10^4K). The scatter about the fitted line in the plot corresponds to an uncertainty of roughly ±500 degrees K in electron temperature for a measured value of $\log R_{23}$.

We can now use the [NII] temperature determined from the R_{23} relation along with observed strengths of [NII] $\lambda\lambda$6584,6548 and [OII] $\lambda\lambda$3726,3729 to determine the ionic abundance ratio N^+/O^+. Pagel *et al* (1992) give a convenient formula based upon a 5-level atom calculation:

$$\log \frac{N^+}{O^+} = \log \left[\frac{\text{[NII] } \lambda\lambda 6584{,}6548}{\text{[OII] } \lambda\lambda 3726{,}3729}\right] + .307 - .02 \log t_{\rm II} - \frac{.726}{t_{\rm II}} \tag{3.6}$$

which we have verified theoretically and with a 5-level atom computer program.

Here, [NII] and [OII] are the observed line intensities, and $t_{\rm II}$ is the electron temperature in the [NII] zone derived above.

Finally, to derive N/O, we assume

$$\frac{N^+}{O^+} = \frac{N}{O}$$

There has been some discussion regarding the accuracy of this assumption (see Vila-Costas and Edmunds (1993), with pointers to other articles), but we find through detailed modeling that this equivalency is quite good and introduces only small uncertainties in deriving N/O. To show this, we determined the ratio $\frac{N^+}{O^+}$ averaged over nebular volume for each model. Dividing this quantity by the input abundance ratio N/O for the same model provides a measure of the validity of the above assumption. Ideally, we wish for

$$\frac{N^+/O^+}{N/O} \approx 1$$

In Fig. 3.3 we plot the above ratio against O/H for a subset of our grid of models. The variations due to changing nitrogen abundance within a particular value of O/H are too small to resolve on the plot. We see that over the broad range in O/H the ratio of N^+/O^+ to N/O is always greater than 0.95. Therefore, we may be fairly confident in assuming that the ionic ratio accurately represents the elemental abundance ratio. Similar calculations using an effective temperature of $50,000$K and varying the ionization parameter by a full dex resulted in similar small errors.

Thus, we have devised an algorithm which avoids the need for observing temperature-sensitive auroral lines for determining N/O abundance ratios in extragalactic HII regions. We now proceed to test our method.

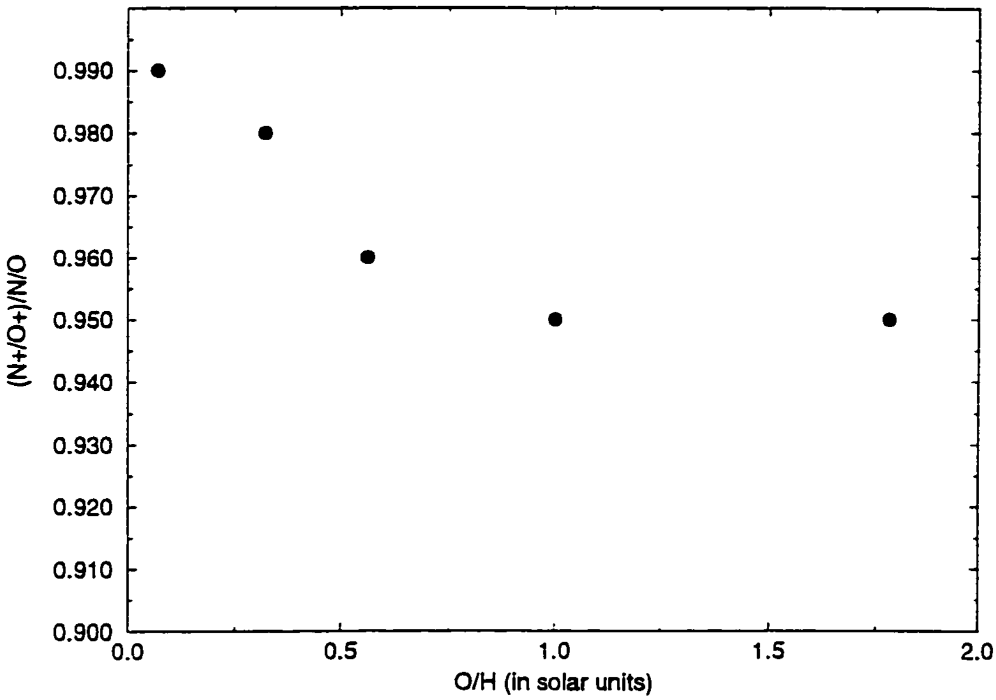

Figure 3.3: N^+/O^+ over nebular volume relative to input N/O abundance ratio versus input O/H abundance for the grid of models. Several models are represented within one point, as the variation due to different N/O input values is unresolvable. Points are computed for T_{eff} = 40000K using the photoionization code CLOUDY.

3.2.2 Testing the Method

Input parameters for each model in our grid, as stated before, include elemental abundances, gas density, ionization parameter, and stellar effective temperature, while the output includes computed line intensities. We applied our method to the predicted set of emission lines for each model in our grid to determine $[N/O]_{method}$. We then compared this quantity to $[N/O]_{true}$, the actual value entered into the corresponding model. The results from this analysis are displayed in Fig. 3.4.

On the vertical axis we show the arithmetic difference between the above quantities as a function of O/H for each model. The dotted line indicates the value for no discrepancy. It can be seen that our method produces uncertainties on the order of ± 0.05 dex across the original grid metallicity range. For these models, stellar effective temperature was again held constant at 40,000K. Varying the T_{eff} up to 50,000K introduced small additional errors of about 0.1 dex. This is attributed to additional photoionization electrons from the harder radiation collisionally exciting ions of oxygen and increasing the number of ions emitting spectral lines. We discuss this and other contaminants of this relation below.

The vertical scatter within a set of models of the same O/H in Fig. 3.4 is due to the spread in input nitrogen abundance—N/H ranges from high to low values as the points move vertically upward. This uncertainty is associated with the use of Fig. 3.2 to obtain electron temperature. As N/H grows within a set of oxygen abundances, the electron temperature drops slowly (nitrogen is an important coolant in nebulae). One can then see from Eq. 3.6 that a lower temperature will lower the ionic abundance ratio. One may note a systematic error resulting in

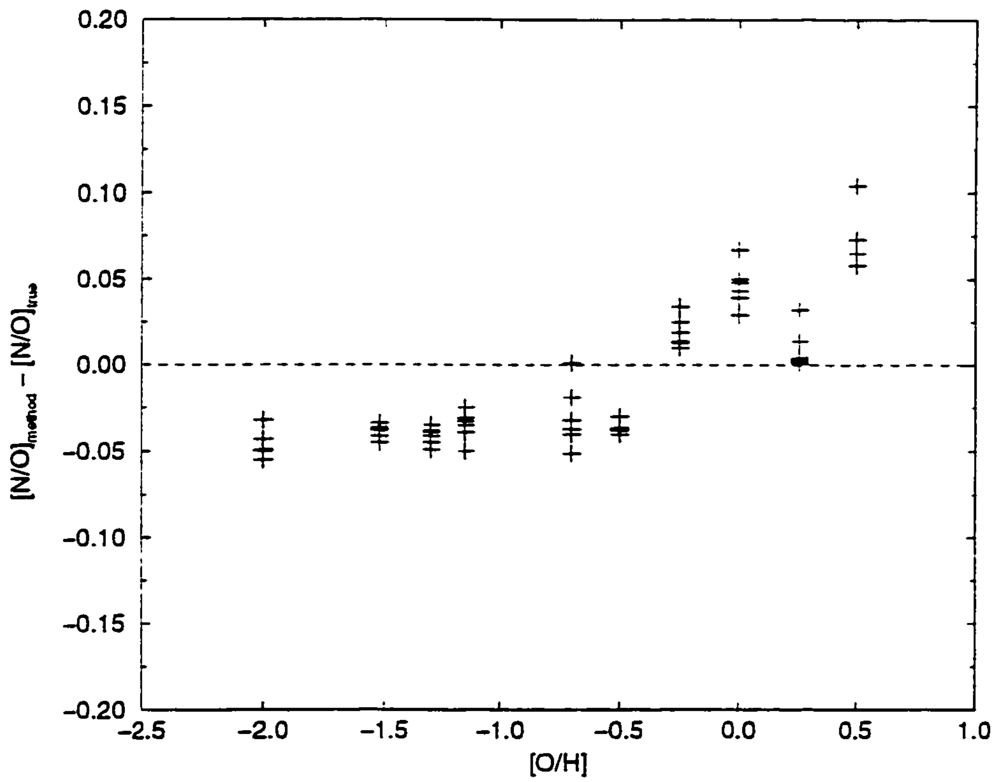

Figure 3.4: [N/O] inferred from model output line strengths compared with model input. [N/O] plotted as a function of input [O/H]. Models with the same [O/H] differ in input [N/O].

an overestimation of the [N/O] abundance at high O/H in Fig. 3.4. This is due primarily to the bias in the polynomial fit of the inversion of $j(T)$, given earlier in Eq. 3.3. If we overestimate the electron temperature, then we infer a higher abundance ratio.

Next, we test our algorithm on a triad of galaxies, NGC 4254, NGC 4303, and M101, recently studied by Henry *et al* (1994), Henry *et al* (1992), and Henry and Howard (1995), respectively. The N/O ratios are derived using emission line strengths from the above references for individual HII regions located in individual galaxies and are shown in Fig. 3.5 and the two figures following. Figs. (3.5 - 3.7) are plots for the above three spirals of logarithmic N/O values normalized to the solar value versus galactocentric distance in units of effective radius, where the latter is the radius of an aperture centered on the galactic nucleus and admitting one-half of the total disk light. The data points represent the abundances for individual HII regions, as determined using our algorithm. The solid lines show simple linear fits to these points. For comparison, results from the above references are shown using dashed lines. It should be noted that in using our method, we obtain N/O for individual HII regions whereas in the papers cited, only the overall trends in N/O behavior across the disks were derived.

The slopes representing the abundance gradients agree well. The discrepancies between the fits are due to differing stellar effective temperatures as well as variations in the ionization parameter chosen for the models. Note we reproduce here the steep [N/O] gradient found in Henry and Howard (1995) for M101 [Fig. 3.7] as well as an earlier study [Evans (1986)].

There is an important point regarding these comparisons: while it is true that both methods (the new one presented here as well as the detailed scheme used in the earlier analyses) rely upon the same photoionization code, the fact that derived slopes are consistent reinforces the validity of the new method. This further implies that discrepancies in abundance slopes with other studies using different photoionization codes may be first traced to differences in the codes rather than errors within the methods. As a case in point, consider a different abundance algorithm, e.g. the one used by Vila-Costas and Edmunds (1993). This earlier work calculated nitrogen abundances and derived gradients whose

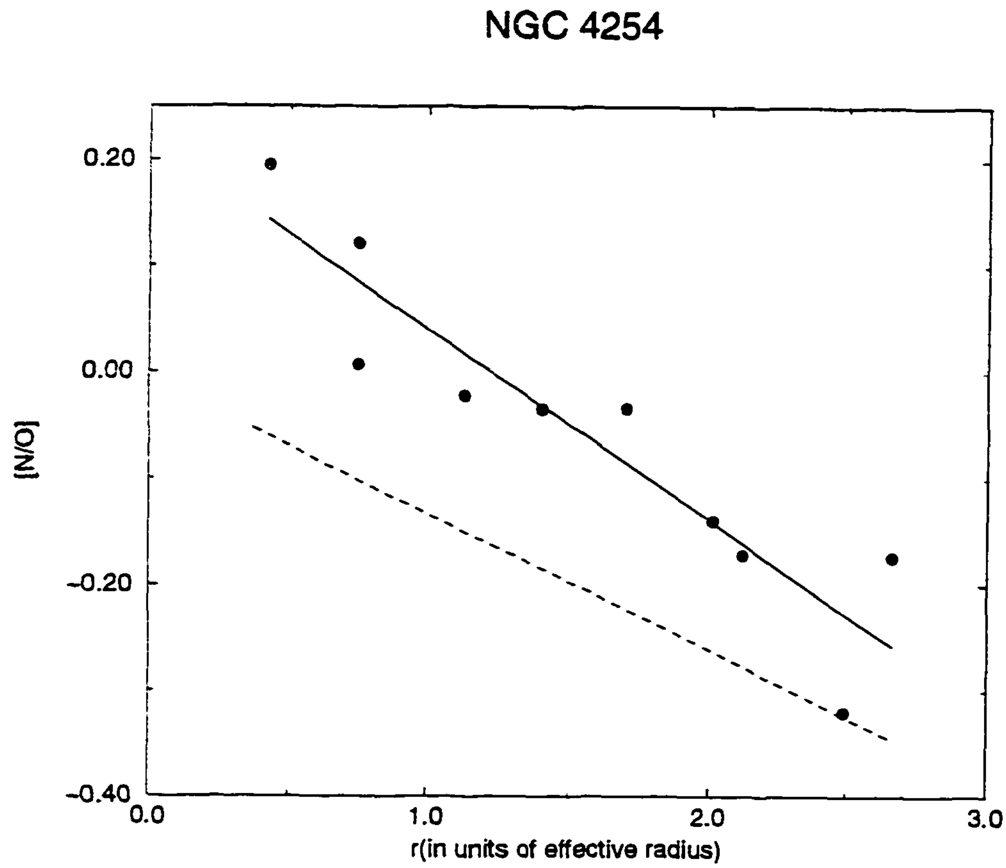

Figure 3.5: Derived [N/O] values from the method presented here versus galactocentric distance in units of effective radius for individual HII region observations from NGC 4254. The solid line corresponds to a linear fit to the data, and the dashed line is the result of Henry *et al.* (1994).

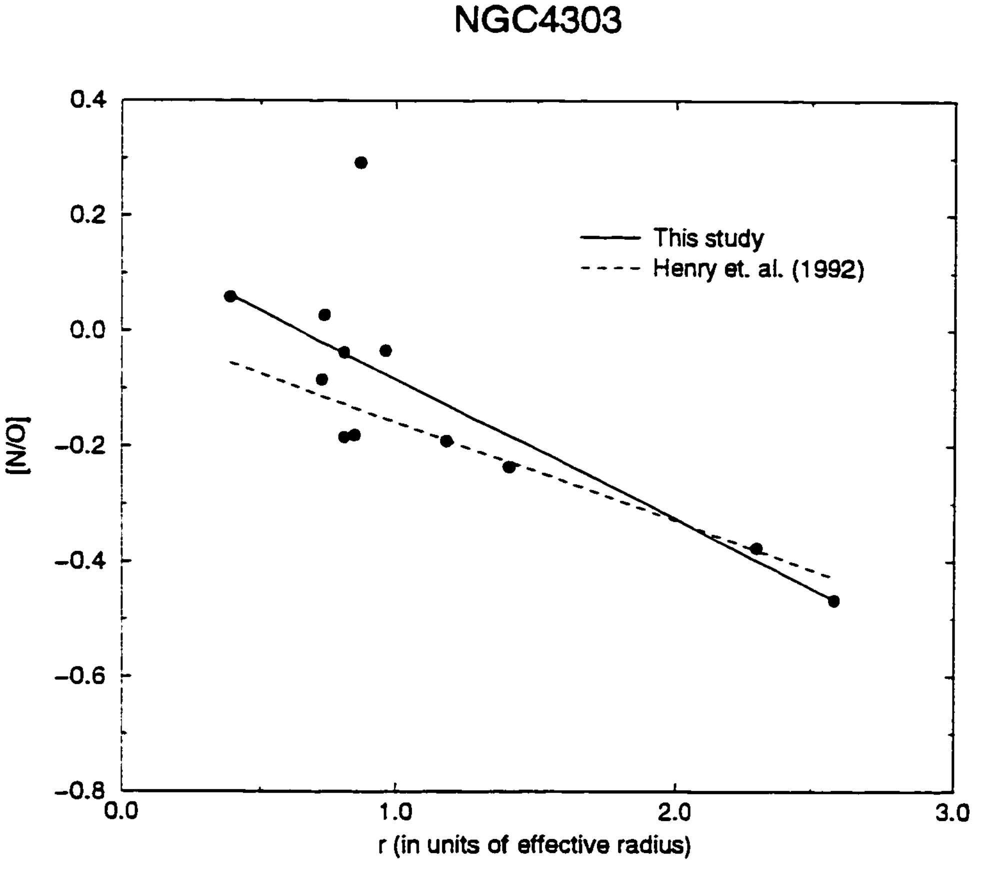

Figure 3.6: Same as Fig. 3.5, but for NGC 4303. Dashed line from Henry *et al.* (1992).

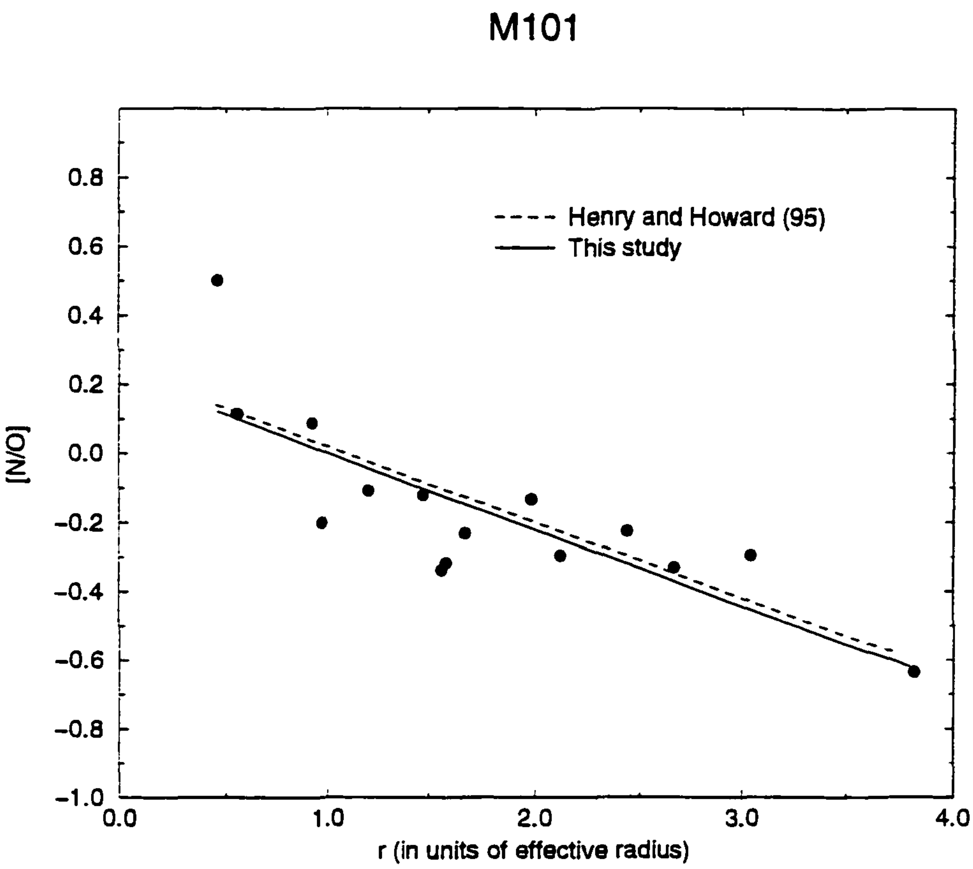

Figure 3.7: Same as Fig. 3.5, but for M 101. Dashed line from Henry and Howard (1995).

slopes were significantly steeper relative to our results for the same galaxies. We have shown that our method presented is internally consistent when using the photoionization code CLOUDY. Thus, the main discrepancy source may stem from the use of a different code, as Vila-Costas and Edmunds' work was based upon the program PHOTO (Stasińska (1990)).

Note that in subsequent discussions, we show the variation of [N/O] with both galactic radius as well as [O/H]. Typically, O/H is derived from observational as well as modeled relationships between the R_{23} ratio and oxygen abundance (Pagel *et al* (1979),Edmunds and Pagel (1984),Edmunds (1989),Skillman (1989)). However, this relation is somewhat sensitive to nebular parameters such as stellar effective temperature, density, and the depletion of refractory elements.

We summarize some of these points in Figs. 3.8 and 3.9, where we plot model input O/H in solar units against the associated model-predicted $\log R_{23}$ emission line ratio. In Fig. 3.8 there are four curves shown: three of them represent a set of models with gas phase abundances of the refractory elements Mg, Si, Ca, Fe, Al, and Ni reduced to 0.1 of their solar level (Anders and Grevesse (1989)), but stellar effective temperature is varied as shown. The fourth curve represents the case for gas phase refractory depletion of only 0.5 solar. A higher level of refractory elements results in more cooling from these elements, with [SiII] 34.8 μm the major coolant. Consequently less cooling is handled by the oxygen lines, thus driving the oxygen emission down. As also shown in Fig. 3.8, the choice of stellar effective temperature imparts additional variance in $\log R_{23}$. The errors involved may be substantial—choosing a low effective temperature may lead to underestimates of the oxygen abundance as large as a factor of two, while overestimating the amount of elemental depletion on grains may grossly overestimate the metallicity in a given HII region, affecting the $\log R_{23}$ ratio by an order of magnitude. For a further discussion of refractory element depletion and its effects on R_{23}, see Henry (1993) and Shields and Kennicutt (1995). Further complicating the relationship is the variation in the line ratio due to the changing abundance of elements important in nebular cooling processes, such as nitrogen (see Fig. 3.2).

Fig. 3.9 elaborates upon the theme of Fig. 3.8, showing the relationship between $\log R_{23}$ and O/H for the input parameters in this study. Here, the effective temperature is held at 40,000K and we show the relation for both high- and low-metallicity regimes. Obviously, there should be a method for discriminating between O/H values for an observed $\log R_{23}$. The best method, as suggested by Eq. 3.3, is to obtain electron temperatures through observations of the appropriate lines; however, as already pointed out, the difficulty in these observations is what has led to this new algorithm. In practice, an independent derivation of O/H usually takes place to resolve the degeneracy, or one could examine the raw intensity of [NII] and [OII], [OIII] lines to more accurately determine the metallicity regime in question.

In Fig. 3.9, the solid lines illustrate a least-squared fit to the data, with fitting parameters of

$$12 + \log(O/H) = 6.90 + 0.93(\log(R_{23})) + 0.52(\log(R_{23}))^2 \text{ for [O/H] } \leq 0.1 \quad (3.7)$$

for the low-metallicity region, and

$$12 + \log(O/H) = 9.29 - 0.31(\log(R_{23})) - 0.66(\log(R_{23}))^2 \text{ for [O/H] } \geq 0.1 \quad (3.8)$$

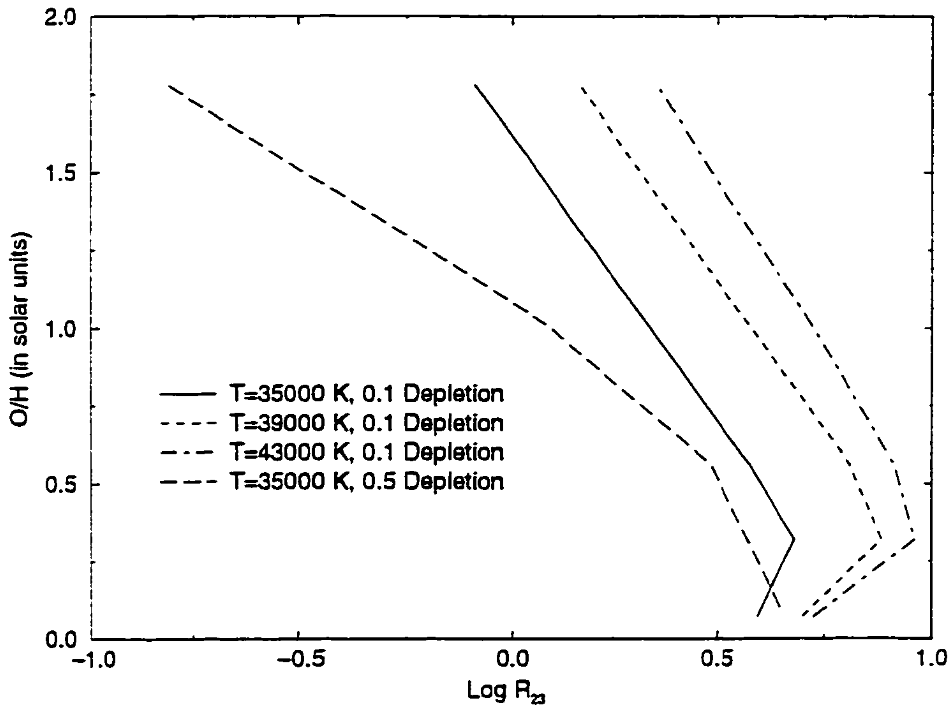

Figure 3.8: Input O/H versus output value for $\log R_{23}$ for a series of models. Separate curves show dependence upon stellar effective temperature and refractory element depletion assumptions.

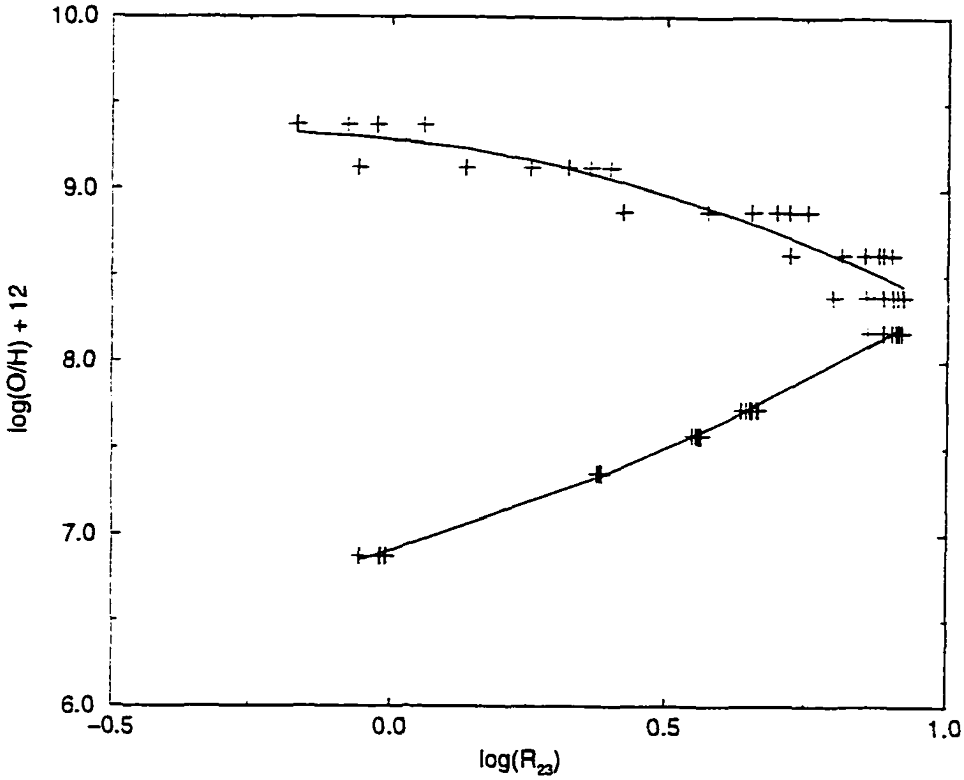

Figure 3.9: Input O/H versus output value for $\log R_{23}$ for a series of models. Note the lack of a unique functional relationship. The solid lines are least-squared fits to the data. The models cover the range $-2.0 < [O/H] < 0.5$, and are generated from the photoionization code CLOUDY with an effective stellar ionizing temperature of 40,000K.

for the high-metallicity region.

We therefore must choose a specific calibration to derive [O/H], and we select the one given in Edmunds (1989). This is the same calibration used in Vila-Costas and Edmunds (1993), in order to make direct comparisons of [N/O] vs. [O/H] abundance ratios with earlier works. This comparison is shown in the following section.

3.3 N/O In A Small Galaxy Sample

We now analyze a small subset of galaxies from the compilation of Vila-Costas and Edmunds (1993) using our new algorithm for determining [N/O]. We chose galaxies for which at least 9 HII regions have been observed (except for M51). Line strengths of [NII] λ6584, [OII] λ3727, and [OIII] $\lambda\lambda$4959,5007 relative to Hβ were taken from the original sources given in Vila-Costas and Edmunds (1993) and new values of [N/O] were determined. Our final results are shown in Tables A.1 - A.11 and Fig. 3.10.

The first column in the tables in Appendix A lists the parent galaxy, and the second column lists the identification of the HII region as given in the original reference. Columns (3), (4), and (5) give the values for effective radius, derived [N/O], and [NII] temperature determined from Eq. 3.3. Data for the effective radii were obtained from Vila-Costas and Edmunds (1992).

Figs. 3.10 and 3.11 graphically show the results in Appendix A, with the [N/O] abundance plotted against effective radius and [O/H] respectively for our sample of ten galaxies. Dwarf galaxy observations are not included, as the radial parameter often is meaningless in dwarf irregular and elliptical galaxies. In Fig. 3.10,

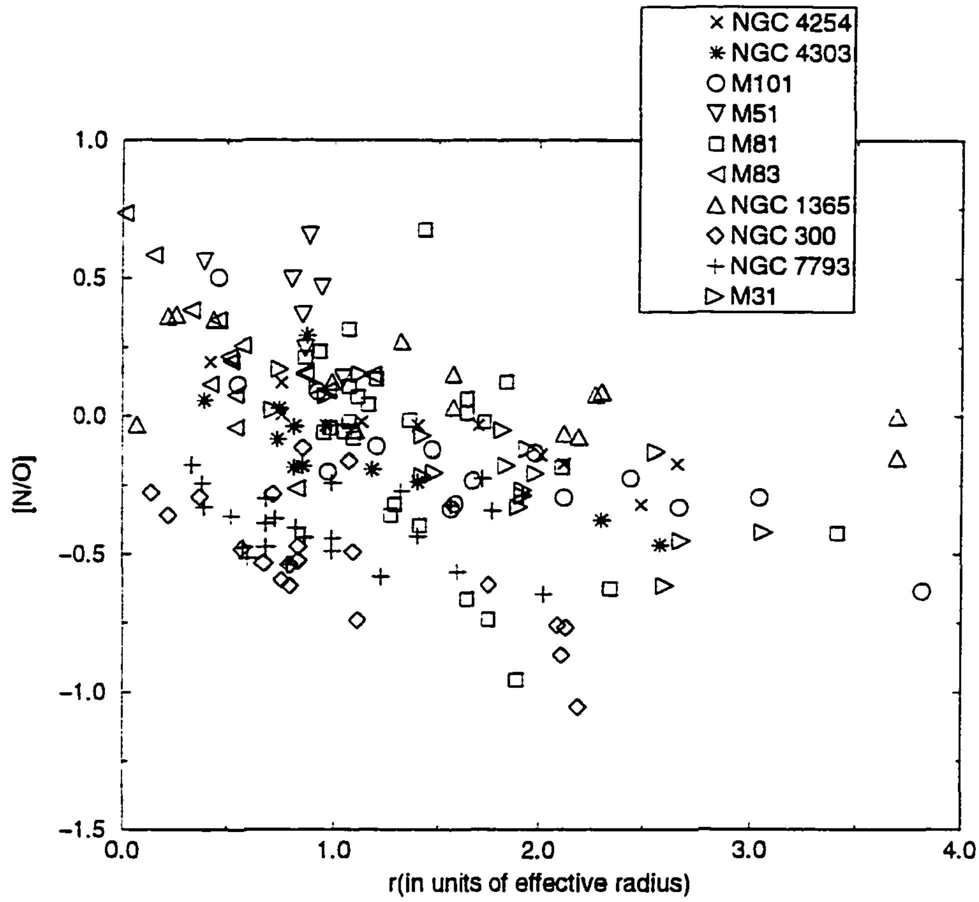

Figure 3.10: Derived [N/O] abundances against galactocentric distance in units of effective radius for seven galaxies in the Vila-Costas and Edmunds (1993) sample, as well as the three galaxies previously shown (NGC 4254, NGC 4303, and M101). Results for specific galaxies are designated by symbol shape.

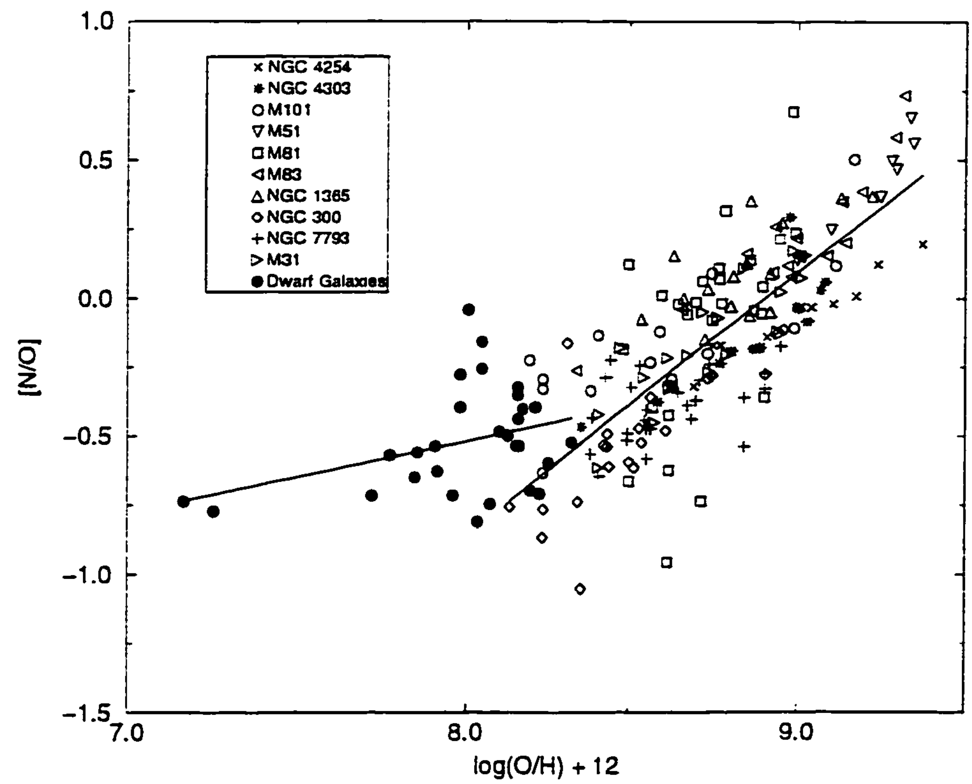

Figure 3.11: Derived [N/O] abundances plotted against [O/H] for our sample. [O/H] was calibrated with the relation in Edmunds (1989). The solid lines represent a least-squared fit to each set of data, as we segregate the dwarf galaxy regions from the spiral galaxy regions. Note the slope for spirals is approximately = 1, which is the slope expected for purely secondary behavior of nitrogen (Edmunds (1990)). The symbols are the same as in Fig. 3.10.

symbol shape refers to specific galaxies as defined in the legend. The data show no unambiguous trends, although a negative gradient in [N/O] is suggested. To directly compare this new algorithm with earlier studies, we also plot the dependence of [N/O] upon [O/H] in Fig. 3.11. Here, dwarf galaxy observations catalogued in Kobulnicky and Skillman (1996), Campbell, Terlevich and Melnick (1986) are appropriate and included.

One may infer positive gradients, implying either some secondary component of nitrogen, or a systematic effect of variation of mean age across the disks showing up because of the delayed release of nitrogen. The contrast in slopes between the spiral galaxies and the dwarf galaxies is interesting, and will be addressed via the chemical evolution models. It is roughly interpreted as illustrating both the delayed release of nitrogen and the fact that nitrogen yields increase with an increase in initial metallicity (secondary behavior). A quantitative analysis is given in Table 3.1. Here we list the slopes of a linear fit to the [N/O] vs. [O/H] data for each galaxy in our sample, and compare these to slopes derived in Vila-Costas and Edmunds (1993).

Table 3.1

Galaxy Name	Slope	$[N/O]_\odot$	Slope (VE93)	$[N/O]_\odot$ (VE93)
NGC 4254	0.66	-0.10	0.83	-0.08
NGC 4303	0.79	-0.09	0.71	0.14
M101	0.64	0.04	0.92	0.03
M51	1.33	-0.07	1.26	-0.15
M81	1.31	0.02	1.10	0.18
M83	0.87	0.13	1.08	0.04
NGC 1365	0.65	0.11	0.85	-0.13
NGC 300	0.80	-0.21	0.65	-0.29
NGC 7793	0.30	-0.38	0.88	-0.26
M31	0.88	-0.09	1.01	-0.06
Dwarf	0.26	-2.60	...	...

Table 3.1: Linear fits of $[N/O]$ vs. $[O/H]$ for several spiral galaxies as derived in this work. Also shown are the values given in Vila-Costas and Edmunds (1993) (denoted as VE93) for the same galaxies using a different] nitrogen abundance algorithm. $[N/O]_\odot$ represents the $[N/O]$ value at solar O/H abundance. Uncertainties are approximately ± 0.05 in the slope due to the uncertainties in the algorithm.

It is important to note that there is no obvious evidence from our data for the need of anything other than a *single* gradient in [N/O] for these galaxies. A composite primary/secondary production process will require a change of slope at some [O/H], but our data are not complete or accurate enough on any given galaxy to claim a definite change of slope. We find that [N/O] is overall varying somewhat less steeply with [O/H] than was found in Vila-Costas and Edmunds (1993), with slopes between 0.30 and 1.33, to be compared with the 1.0 expected from a simple secondary behaviour. There is a hint, however, that (apart from NGC 4254) the average relation is steepening to about 1 above log(O/H) + 12 equal to 9.0 as shown in Fig 3.11.

In Fig. 3.12 we show essentially the same plot as Fig. 3.10, except the symbol shapes represent general morphological type, where late galaxies include types 5-8 while early ones include types 2-4. Table 3.2 lists the morphological type of each galaxy in the study, taken from Vila-Costas and Edmunds (1992). Here again we neglect to show the dwarf galaxies, as they fall into neither early or late classifications and we are interested in systematic differences among spirals.

Table 3.2

Galaxy Name	T-type
NGC 4254	5
NGC 4303	4
M101	6
M51	4
M81	2
M83	5
NGC 1365	3
NGC 300	7
NGC 7793	8
M31	3

Table 3.2: Galaxy morphological T-type used in this thesis, values from Vila-Costas and Edmunds (1992)

This figure shows that the spread in nitrogen abundances for a specific [O/H] are consistently about 0.5 dex and not quite as large as the previous graph shows, since the spread within a particular group of galaxies is less than the composite variance. Interestingly, one can also see that late type spirals tend to have a systematically lower [N/O] than the early types for a given radial coordinate. This is consistent with the speculation in Vila-Costas and Edmunds (1993) regarding this same effect in their study: the slight shift may be due to a delayed secondary component of the nitrogen production mechanism, as the average age of stellar populations are older (on the average) in the early spirals as opposed to the late types (c.f. Edmunds and Pagel (1978), although the original suggestion was made assuming primary nitrogen production). It is seen that early type galaxies also have systematically higher (O/H) than the late types.

It is not entirely obvious how to relate the observations of different spiral galaxies. The effective radius varies among spirals, so we may be introducing additional uncertainty when plotting relationships between many spirals such as in Fig. 3.10. Different normalization procedures are discussed in Vila-Costas and Edmunds (1992). The data in Fig. 3.10 is also plotted for a different normalization parameter, R_{25} (defined as the length of the major axis of the galaxy out to a blue surface brightness level of 25mag arcsec^{-2} after correcting for inclination and galactic extinction). No systematic difference was noted for this change of normalization, however.

We calculated three least-squares fits to the *composite* data in Fig. 3.11 and the *late* and *early* galaxy data in Fig. 3.12, respectively, and obtained the following regression lines:

$$\begin{array}{rrcl} \text{Composite:} & [\mathrm{N/O}] & = & 0.96(12+\log(O/H))-8.51 \\ \text{Late:} & [\mathrm{N/O}] & = & 0.87(12+\log(O/H))-7.87 \\ \text{Early:} & [\mathrm{N/O}] & = & 1.00(12+\log(O/H))-8.85 \end{array} \tag{3.9}$$

These slopes have an approximate uncertainty of ± 0.05 dex, and the intercepts about ± 0.1 dex.

Our variance in nitrogen abundance is slightly enhanced by the fact that we plot all morphological types together; there are suggestions of systematic differences in [N/O] for different galaxy types, as discussed above.

The fitted lines in Fig. 3.12 also suggest that the [N/O] gradient is shallower for late type spirals, though the spread in N/O at a specific distance makes it difficult to decide for certain. Further complicating the interpretation are the gradients

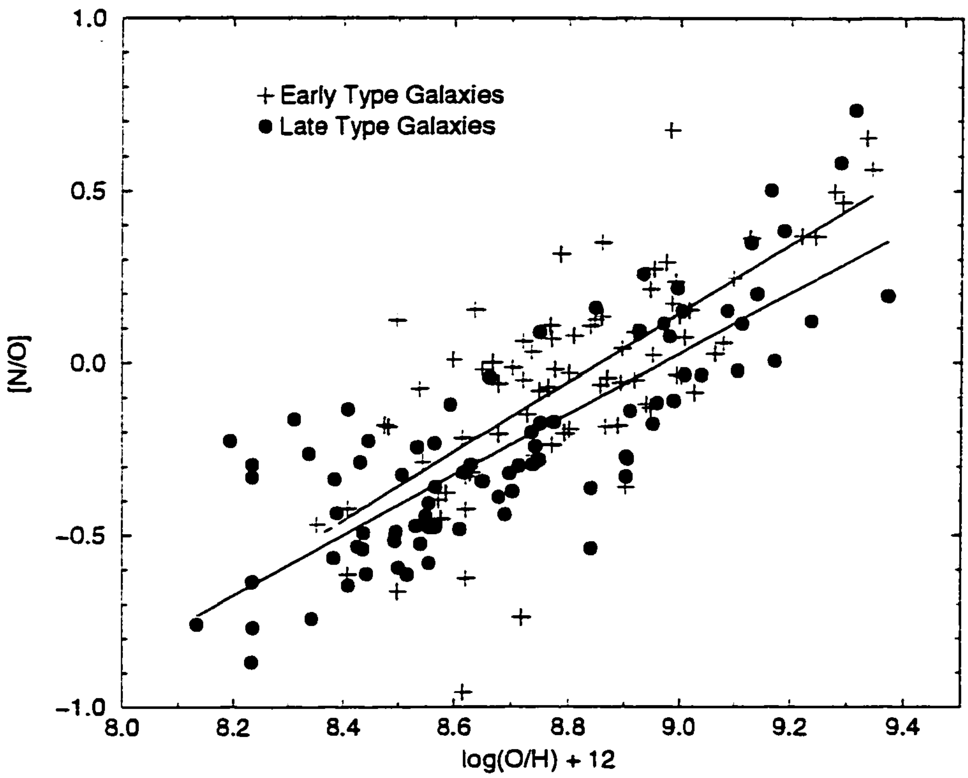

Figure 3.12: Same as Fig. 3.11, except symbol shapes now designate either early (type 2-4) or late (type 5-8) galaxies. For both plots, regression lines are shown with the fits given in the text.

in stellar effective temperature in HII regions found in studies by Henry and Howard (1995). We show, however, in Fig. 3.13 that the changes incurred using a stellar effective temperature of 35,000K instead of 40,000K are small, though not insignificant. The published algorithm (Thurston, Edmunds and Henry (1996)) was calibrated at a stellar effective temperature of 35,000K, and showed a similar divergence according to galaxy type. We are assuming that a temperature change of 5,000K is ample to cover the entire variation across the galaxy. Here we have plotted the same data as for Fig. 3.10; however we also recalibrate our algorithm with an effective temperature of 35,000K and show these values. The general trend is to make the relation slightly shallower as we lower the effective temperature. Note that this is shown for photoionization models using a particular [Mihalas (1972)] stellar atmosphere, so the temperature dependence may be different for differing model atmospheres. This dependence was not explored in this thesis.

The changes in these and other "environment" variables may mask or augment any actual variation in the abundance of a given element through their effect on the emission of lines.

3.4 The N/O Algorithm in Metal-Poor Galaxies

Kobulnicky and Skillman (1996), Campbell, Terlevich and Melnick (1986) have observed and catalogued emission lines from star-forming regions in dwarf galaxies. New [N/O] abundances were computed for these objects in Kobulnicky and Skillman (1996), and serve as a valuable set of test cases for this algorithm at low oxygen abundances. These regions are of intense interest to researchers, as they often show extremely low metal concentrations. This seems to imply that the first

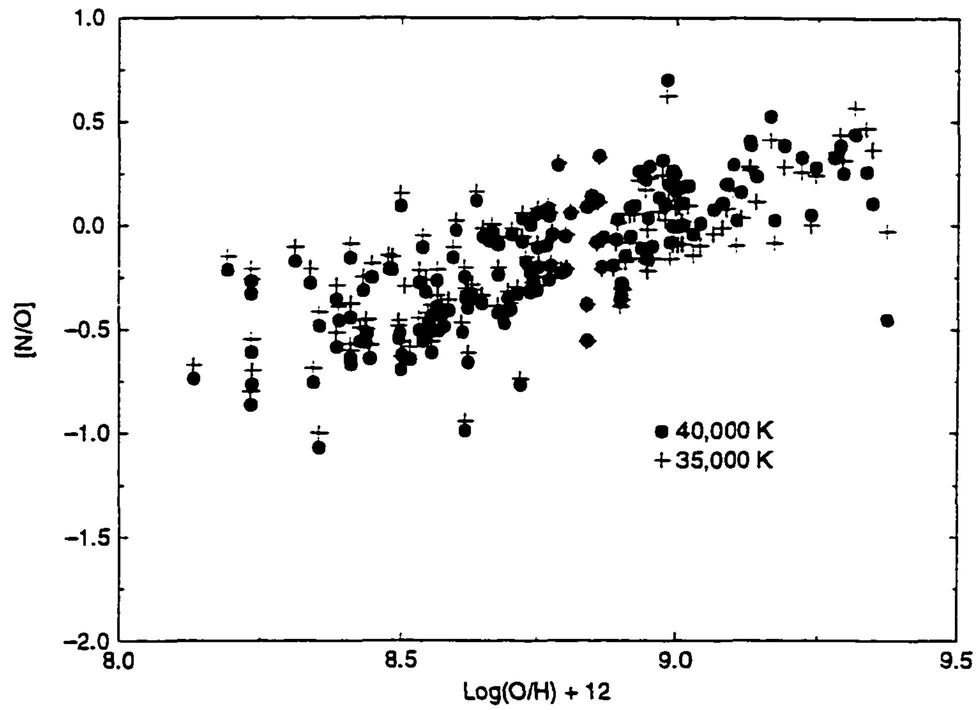

Figure 3.13: Derived [N/O] abundances plotted against [O/H] for our full sample of HII regions. Shown is our algorithm calibrated at 40,000K (circles) and at 35,000K (pluses). Note the relatively small deviations as we lower the effective temperature serve to flatten the relation slightly.

generations of stars have just formed or are being formed, and give us a window into the possible star-forming history of the early galaxy. The 10 spiral galaxies considered in the last section had relatively high oxygen abundances, so we now wish to test this nitrogen abundance algorithm on HII regions with very little previous oxygen contamination.

We choose the set of observations made by Campbell, Terlevich and Melnick (1986) to compare, as well as those of the famous object I Zw 18 (Skillman and Kennicutt (1996)). I Zw 18 in particular is an important test case, as this is the current record-holder for the lowest oxygen abundance (roughly 1/50 solar). It has been argued (Kunth and Sargent (1986)) that it is extremely unlikely that any HII regions with a significantly lower (O/H) *will* be observed, due to the fast pollution (on the order of 10^6 years) of the environment by massive, short-lived stars that generate most of the oxygen we observe.

Fig. 3.14 shows the comparison between our algorithm evaluated in the metal-poor regime and the calculations of Kobulnicky and Skillman (1996). In that study, the authors computed an effective temperature in the O^{++} emission region with relations from Osterbrock (1988) (similar to our calculations for the N^+ region). Temperatures from O^{++} and N^+ may disagree significantly, so Pagel *et al* (1992) and Skillman and Kennicutt (1993) developed a relation between these temperatures based upon the photoionization models of Stasińska (1990). Our results agree well across the metallicity range, however there is a noticeable bias where the present method seems to consistently underestimate the [N/O]. The major source of error can be traced to the method used to compute the electron temperatures in the two methods. Here, the temperature is ultimately derived from observations of [OII] λ3727 and [OIII] $\lambda\lambda$4959,5007, which are all reasonably strong emission lines and correlate well with the [NII] temperature, as can be seen in Fig. 3.2 at low metallicities. In the Kobulnicky and Skillman (1996) survey, the initial O^{++} temperatures are derived from observations of [OIII] $\lambda\lambda$4959,5007 and [OIII] λ4363, the latter of which is typically very weak and subject to a relatively large uncertainty in the intensity. Further compounding the uncertainty is the typical presence of noise and contamination from surrounding stronger lines. This contamination often mimics true detection, (Kobulnicky and Skillman (1996)) and tends to overestimate the temperature (and consequently the [N/O]). Our method should be more precise, since strong emission lines are directly correlated with needed electron temperatures. An additional small source of error is caused by our polynomial fit in Fig. 3.2, where the fitted line intersects the lines of constant O/H at roughly solar values of N/O. In reality, all of these regions have $[N/O] < 0$, so we underestimate the electron temperature and therefore underestimate the [N/O] slightly.

The overall slope of [N/O] vs. [O/H] for the metal-poor set of dwarf galaxies is given in Table 3.1, and is significantly shallower than that of the composite spiral sample. This has been discussed in the earlier section, and we shall return to it in Chapter 4.

3.5 Summary

We present a new method for deriving nitrogen abundances relative to oxygen using only the strong optical lines of [OII], [OIII], and [NII]. The motivation for developing this method is to find the electron temperature in regions of both

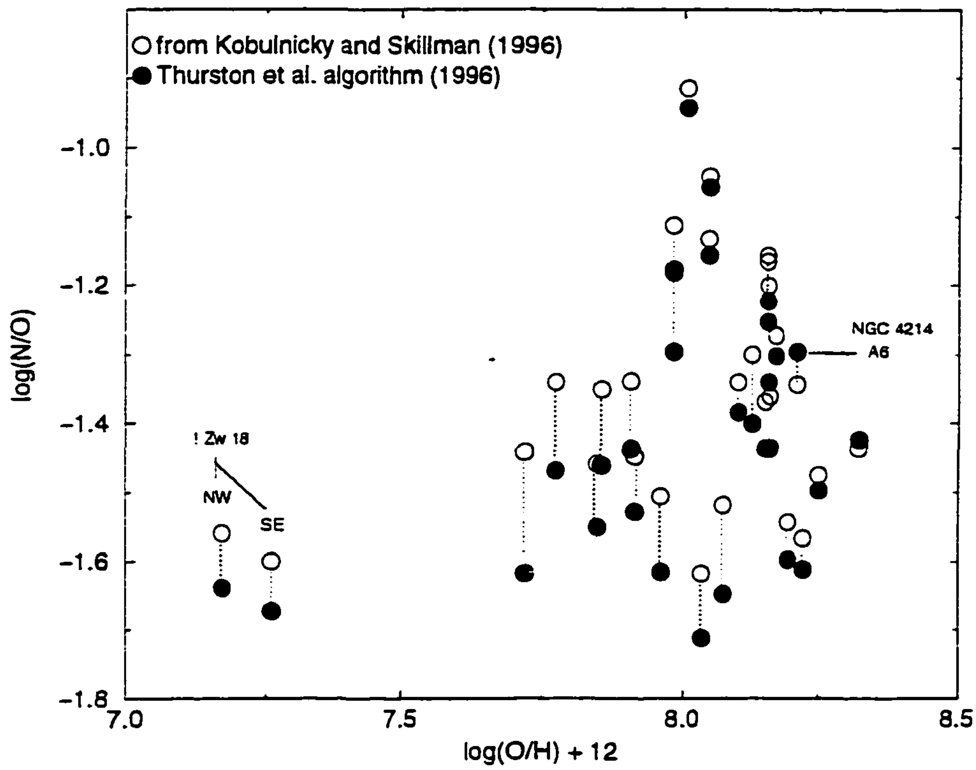

Figure 3.14: Comparison of observation vs. calculated values for a sample of metal-poor star-forming regions. The two regions with $\log(O/H) + 12$ of < 7.25 are the SE and NW knots of I Zw 18, from Skillman and Kennicutt (1996). One region from NGC 4214 is included from Kobulnicky and Skillman (1996) (Region A6), and the others are also from Kobulnicky and Skillman (1996) with the original observations by Campbell, Terlevich and Melnick (1986).

high and low metallicity, when traditional gauges of temperature [OIII] $\lambda 4363$ and [NII] $\lambda 5755$ are too weak to observe. We do this by establishing a relation between the oxygen line ratio R_{23} and the electron temperature in the [NII] emission region [Eq. 3.4 and 3.5], and Fig. 3.2. This relation is reasonably robust, and when coupled with a 5-level atom relation [Eq. 3.6] gives self-consistent abundances when compared with detailed model output. We also show that our method yields consistent results when compared to previous studies which have utilized detailed modeling schemes.

Finally, we applied our algorithm to observational data for 164 HII regions in ten well-observed spiral galaxies as well as metal-poor dwarf galaxy star-forming regions, and generated new estimates of N/O for all of these objects as well as plots of [N/O] vs. galactocentric distance. Our results indicate the presence of a gently decreasing gradient of [N/O] across the disks of spirals as well as a trend toward slightly lower [N/O] abundances in late type spirals relative to early ones. Our gradients of [N/O] vs. [O/H] are compared to an earlier study (Vila-Costas and Edmunds (1993)), and found to be slightly shallower on the average. This would imply that the overall dependence of galactic nitrogen production on seed nuclei may not be as steep as a true secondary process, or that we are seeing the effects of a delayed release of nitrogen with a systematic variation in the mean age of the stellar population across disks. We also find that the [N/O] vs. [O/H] relation is shallower for dwarf galaxies than for spirals, a result consistent with previous studies (Henry (1997)). We now turn to the results of detailed chemical evolution modeling to explain these conclusions.

Chapter 4

Results of Chemical Modeling

Here I present the results of the NICE code as applied to two interesting galactic cases. The goal of this chapter is to address some outstanding issues concerning the implications of our calculated nitrogen abundances in extragalactic HII regions, such as the systematic differences in chemical evolution between early and late type spirals. In the last section, I shall use my numerical models to probe the evolution of nitrogen in dwarf and spiral galaxies as well as to address the question of the timescale of differential nitrogen release (primary vs. secondary).

4.1 Chemical Evolution Differences Between Early and Late Type Galaxies

Here I shall briefly investigate the possible enhancement of [N/O] in early spirals compared to late types with my numerical chemical evolution code, and the inferred differences of the initial parameters between these types of galaxies during formation. It will be useful to briefly review the specific differences in observed quantities between early and late types; in Table 4.1 I list some pertinent parameters that illustrate the segregation of galaxies into these two broad categories. The table illustrates differences between Sa and Sc galaxies, which are typical members of these different morphological types. The data for this table are taken from Carroll and Ostlie (1996).

Table 4.1

	Early (Sa)	Late (Sc)
$\left(\frac{L_{bulge}}{L_{total}}\right)_B$	0.3	0.05
$\frac{M}{L_B}$	6.2 ± 0.6	2.6 ± 0.2
$< B - V >$	0.75	0.52
$\frac{M_{gas}}{M_{total}}$	0.04	0.16

Table 4.1: Table of galactic parameters for early (Sa) and late (Sc) types. The "B" and "V" indicate the blue and visual absolute magnitudes, respectively. Mass and luminosity are given in terms of solar units. From Carroll and Ostlie (1996).

The first row in Table 4.1 shows the most obvious morphological difference between the two types. Early galaxies tend to have large and bright nuclear regions, while late types have dim nuclear luminosities relative to their disks. Late galaxies also typically have many bright HII regions along the spiral arms, which contributes to the non-bulge luminosity. The other obvious observational difference is the $< B - V >$ color difference, (the color *index*) implying that late galaxies are "bluer" than early types. This is most simply interpreted as a greater number of massive blue stars in late spirals. It is true that for a certain IMF, a greater number of blue stars will imply a correspondingly greater number of low-mass red stars, so that it is not immediately clear that the color index should change. The shift in the index can be understood using the data from Popper (1980), which show a mass-luminosity relation in which massive stars emit more luminosity per unit mass than do low-mass stars. Since the radiation from massive stars is concentrated at shorter wavelengths, the overall color observed in a stellar population can appear more blue shortly after a burst of star formation. At later times, after the massive stars have evolved, the color of the region will shift towards the red end of the spectrum. Further evidence for the existence of greater numbers of massive stars in late spirals comes from the $\frac{M}{L_B}$ parameter in Table 4.1, which measures the overall mass/luminosity ratio (in solar units) for the galaxy. The table shows that late spirals have a lower M/L ratio, consistent with the argument that a greater portion of their luminosity comes from massive stars. Finally, one might postulate that a large current population of massive stars implies active star formation, since the lifetime of massive stars is short. One would also expect a large gas fraction in late types to drive the star formation rate. This is supported by the last row in the table, showing that early galaxies have a generally lower gas mass density than late types.

In Chapter 3 we noted a possible correlation between galaxy type and the abundance ratio [N/O]. The average stellar population age is thought to be older in early galaxies, deduced from data such as that shown in Table 4.1. The standard interpretation of the above data is that early galaxies have a very low star formation rate, and therefore the extant stars are generally older than in late galaxies where the rate of formation of new stars is higher. The higher [N/O] in early galaxies is therefore attributed (Vila-Costas and Edmunds (1993)) to the delayed secondary component of nitrogen released at later times by the low-mass stars which preferentially produce secondary nitrogen (See Fig. 4.15 and Figs. 2.5, 2.6). Another factor, though probably less significant, is that early spirals have a generally higher oxygen abundance at a given galactocentric distance than late types (see Fig. 3.12 and Henry (1997), Vila-Costas and Edmunds (1992)). Since the secondary component of nitrogen is dependent upon the initial abundance of the "seed" element (oxygen), the yield of nitrogen will increase slightly with the ambient abundance of oxygen (see also Figs. 2.5 and 2.6).

I shall use the NICE code documented in Chapter 2 in an attempt to model the [N/O]-galaxy type correlation numerically. Recall that the NICE code calculates the change of abundance ratios over time for a single arbitrary "cell" of gas. I must differentiate between the input parameters of early and late types to simulate their present-day observational differences. It is known observationally that early galaxies have a low gas surface density (Vila-Costas and Edmunds (1992), Table 4.1) and hence a low star formation rate. Late spirals tend to have more gas and a higher SFR. I therefore choose early type galaxies to have a more sharply peaked infall rate at early times, while late-type spirals will have an infall rate more heavily weighted towards later epochs. According to this scheme, the early galaxies will use up the available gas at early times during star formation, as shown in Fig. 4.1. The behavior of the SFR should follow that of the gas mass

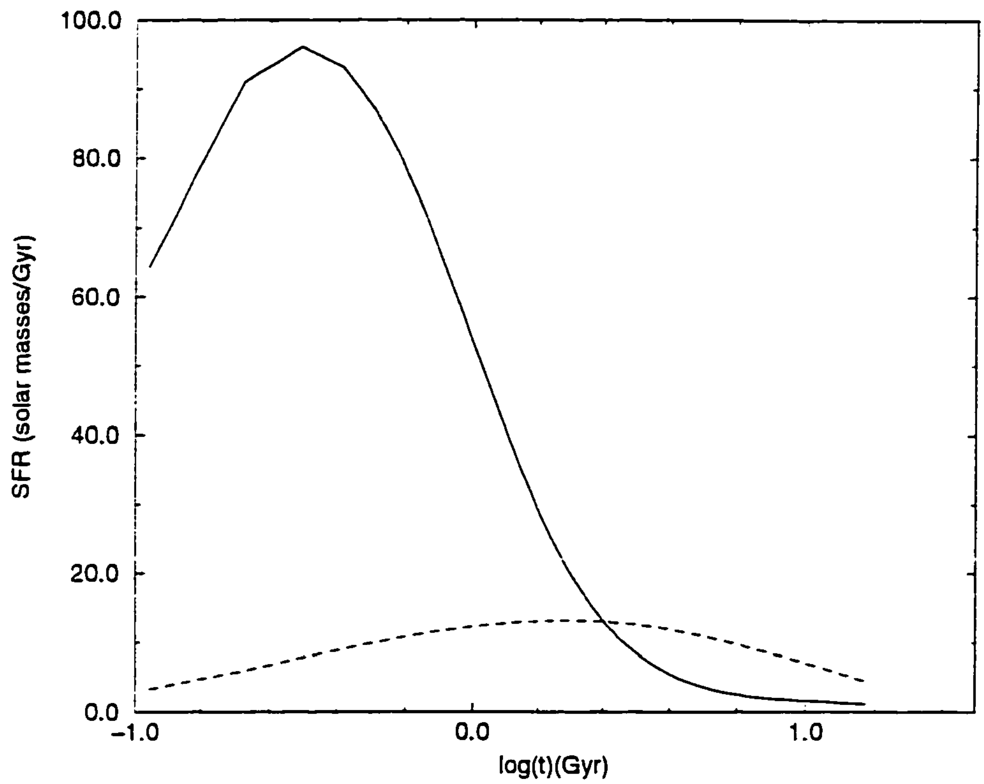

Figure 4.1: Plot of SFR in early- and late-type spirals against time. The solid line denotes the calculation for early spirals and the dashed line refers to late types.

(and therefore the infall rate), since the SFR simply depends on the local gas mass density via a power law (see § 2.2.2).

In the language of Chapter 2, early types have $\tau = 0.5$ while late types have $\tau = 8.0$, where τ represents the exponential timescale for accretion of matter onto the galactic disk. The mass density increase in the calculated zone is shown in Fig. 4.2, where it is seen that the total mass density will increase quickly in the early-type spirals due to the faster infall rate.

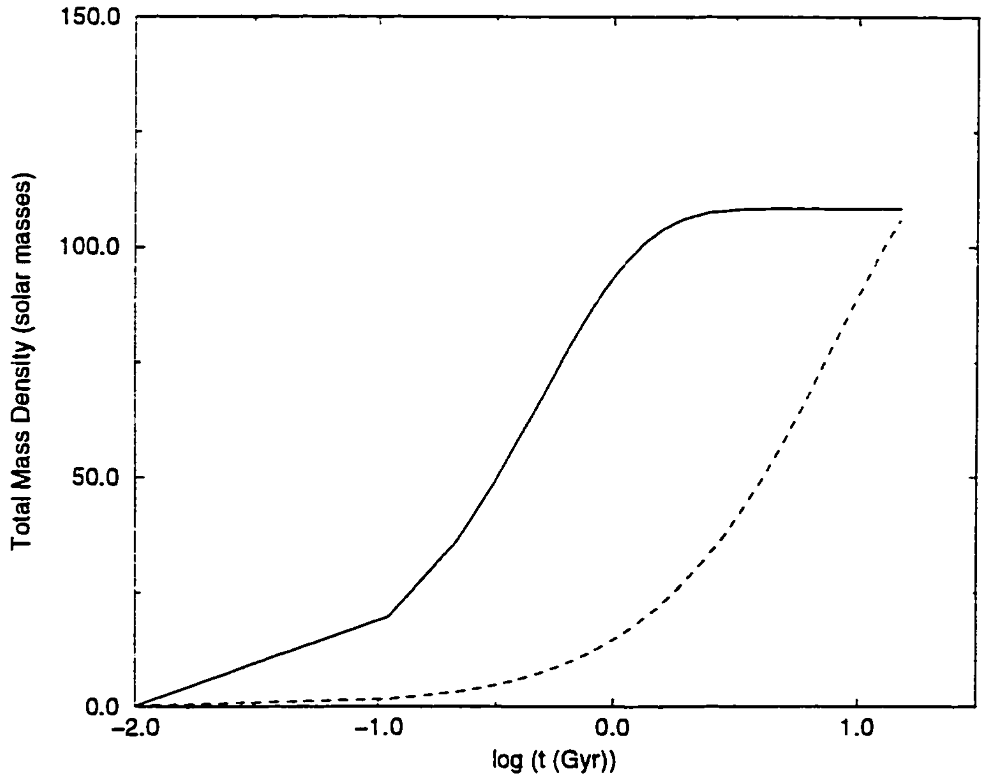

Figure 4.2: Plot of total mass density in early- and late-type spirals against time. The solid line denotes the calculation for early spirals and the dashed line refers to late types.

The input parameters for the NICE models are largely identical to those discussed in Chapter 2, and are shown in Table 4.2. The only difference between the early and late models is the change in the τ_d parameter. The initial gas mass density is actually nonzero, but negligible, in order to avoid arithmetic overflow during the first time step.

Table 4.2

Parameter	Value
Stopping time	15 Gyr
Present time	13 Gyr
Upper Stellar Mass cutoff	40 $M_\odot$
Lower Stellar Mass cutoff	0.08 $M_\odot$
SFR coefficient ν	1.8 $M_\odot$Gyr^{-1}
IMF slope, below 10 $M_\odot$	2.3
IMF slope, above 10 $M_\odot$	2.3
Final mass density	100 $M_\odot$
Initial gas mass density	0.1 $M_\odot$
Exponential infall parameter τ_d	0.5, 8.0 Gyr

Table 4.2: Table of input parameters for spiral galaxy HII regions. The dual values for τ_d are for early and late spirals, respectively.

The total masses of the two types of galaxies at $t = 15$ Gyr are normalized to the same value, so differences in the total mass density should not significantly alter the calculations. This is shown in Fig. 4.3 where the [N/O] ratio is plotted against time for total mass densities of $50 M_\odot$ and $200 M_\odot$. No significant difference in [N/O] can be seen for this changing mass density.

The results showing the difference in [N/O] due to a change in the infall rate are shown in Fig. 4.4, where I plot [N/O] vs. time for the two rates of infall.

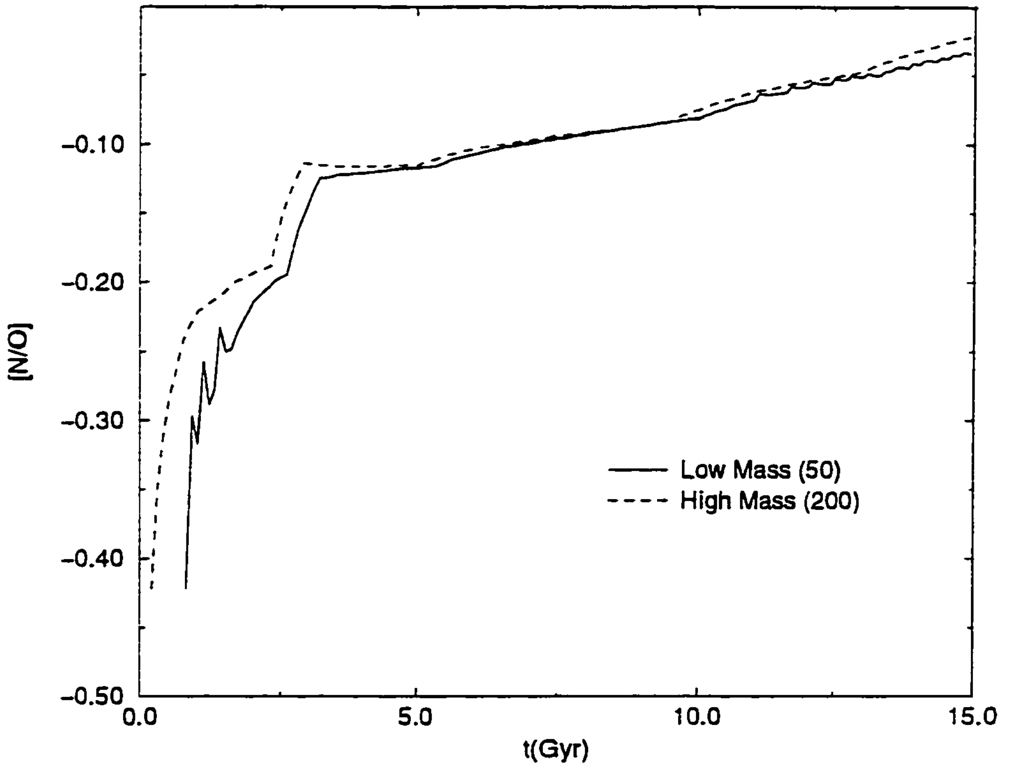

Figure 4.3: Plot of [N/O] vs. time for varying final total mass density. The units in the legend are solar masses.

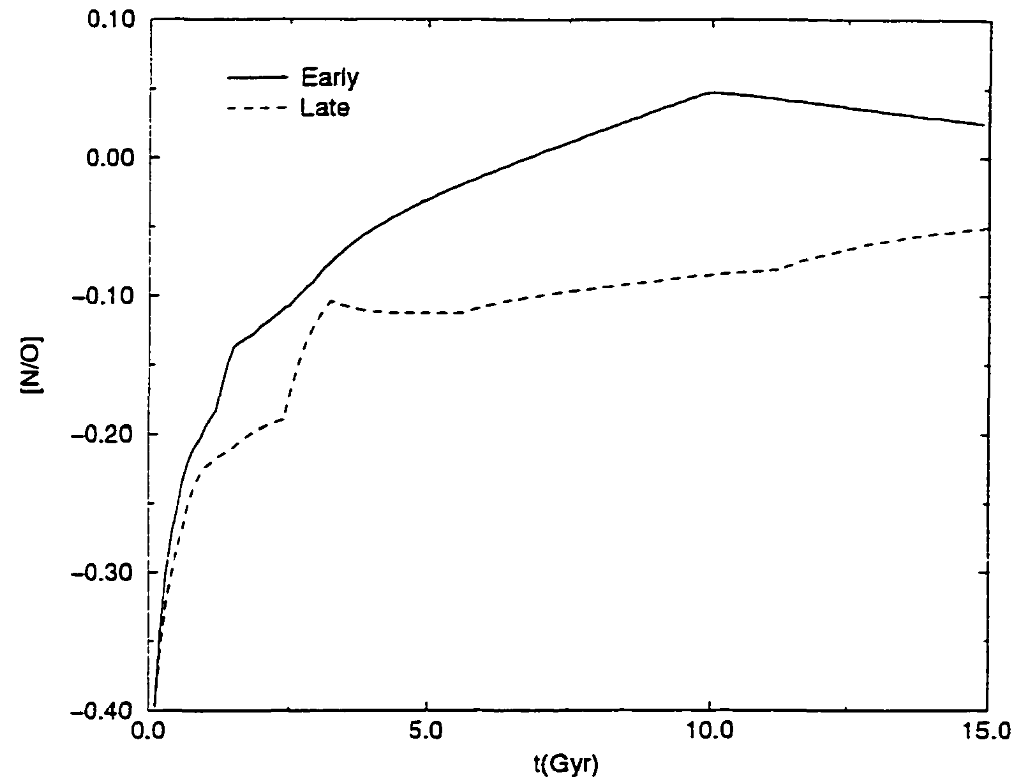

Figure 4.4: Plot of [N/O] evolution in early- and late-type spirals against time in the 1-zone NICE chemical evolution code.

The "kinks" in the diagram reflect the discrete switching of yield databases as time (and metallicity) increase. It is seen that [N/O] is indeed higher in early-type spirals (having the early peak in infall rate), with approximately the same difference in [N/O] abundance ($\sim$ 0.1 dex) as is observed. Furthermore, the gas mass fraction is significantly lower in the early type models (6.2%) than in the late type models (11.7%), which is in general agreement with the observed trends.

It should be noted that changes in other input parameters might alter the results shown in Fig. 4.4. For instance, it is clear that changing the yields of the elements in question would affect the final abundance ratio. In Fig. 4.5, data is shown for two models computed identically to those in Fig. 4.4, except that only the yields calculated with initial solar metallicities are used. Note that a change in [N/O] still exists, though the difference between [N/O] in the early and late types is somewhat smaller. At early times, the [N/O] ratio is higher in Fig. 4.5 than in Fig. 4.4 due to the fact that more nitrogen is generated using solar metallicity yield tables (see Figs. 2.5 and 2.6). Ultimately, since the same yield table is used for all times, the enhanced nitrogen production due to metallicities greater than solar is not reflected either. The final [N/O] is then less than that predicted by the full yield database, as solar metallicities are reached quickly in the early galaxy model where this enhancement occurs. Since the production of secondary nitrogen is almost certainly affected by changes in the initial metallicity of the progenitor star, using the full metallicity-dependent yield database should be more accurate than those yields calculated with a single metallicity. This behavior is important to understand in order to compare my results with those in previous studies, since until very recently only the single-metallicity databases were available.

Changes in other parameters, such as the IMF, need also to be considered. It is clear that making the IMF steeper (increasing the absolute value of the slope) will increase the small-star population with respect to the massive star population. The natural consequence of this is to raise the mass fraction of nitrogen at the expense of oxygen, which will raise the [N/O] ratio. One may see this in Fig. 4.6, where I again plot the [N/O] ratio against time, while now changing the IMF slope to $x = 1.6$ for both the high- and low-mass regime. Note that while the absolute value of [N/O] and the difference between early and late models changes, the basic

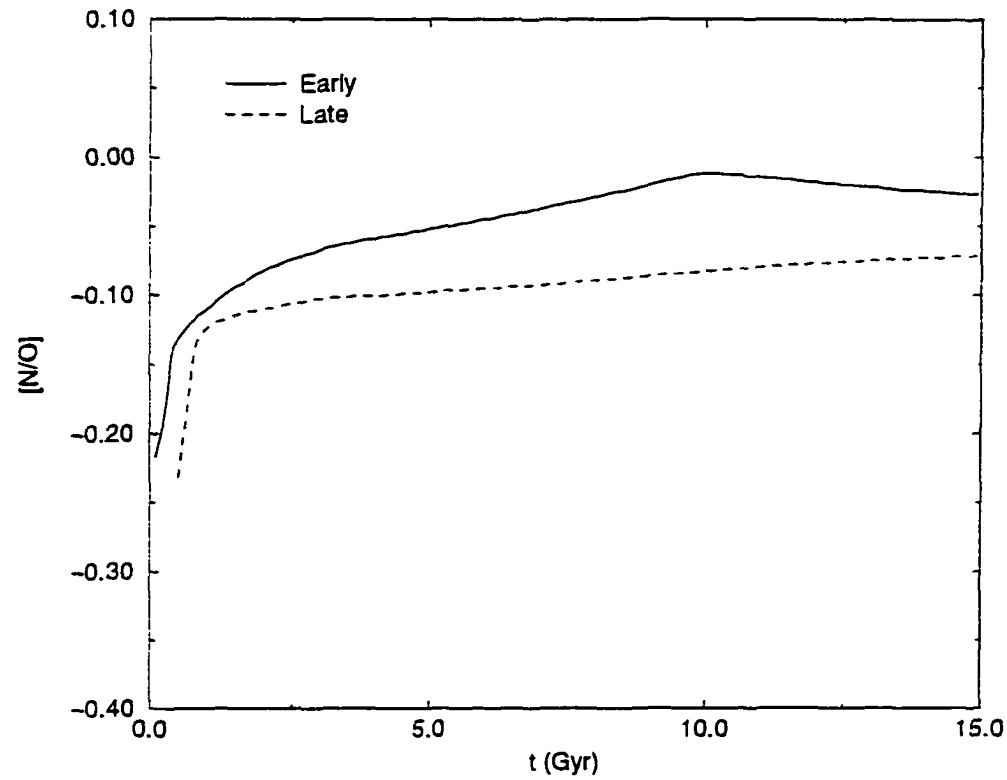

Figure 4.5: Plot of [N/O] evolution in early- and late-type spirals against time in the 1-zone NICE chemical evolution code. This plot is essentially the same as Fig. 4.4, but here I use only the solar-metallicity yields.

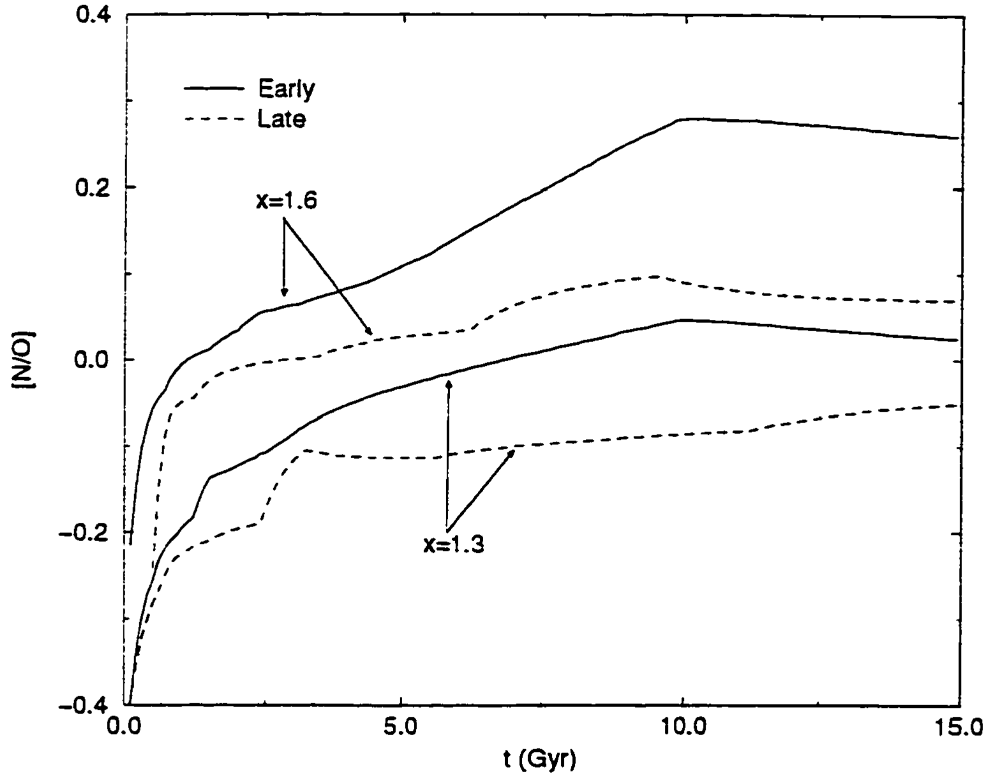

Figure 4.6: Plot of [N/O] evolution in early- and late-type spirals against time in the 1-zone NICE chemical evolution code. This plot is essentially the same as Fig. 4.4, but here the models are calculated with the IMF slope parameter $x = 1.3$ and $x = 1.6$ for both high- and low-mass stars, as indicated.

conclusion (that early-type [N/O] is greater than late-type [N/O]) remains.

It is true that changing the IMF slope will induce a change in the [N/O] ratio without invoking different rates of infall, however a changing IMF alone will not satisfy the observational constraints of a much lower gas fraction in the early galaxies. In Fig. 4.7, I plot the change in the gas mass against time for two values of the IMF parameter, $x = 1.3$ and $x = 1.6$. The gas mass can equivalently be considered to be the gas fraction, as the total mass is the same at all points for

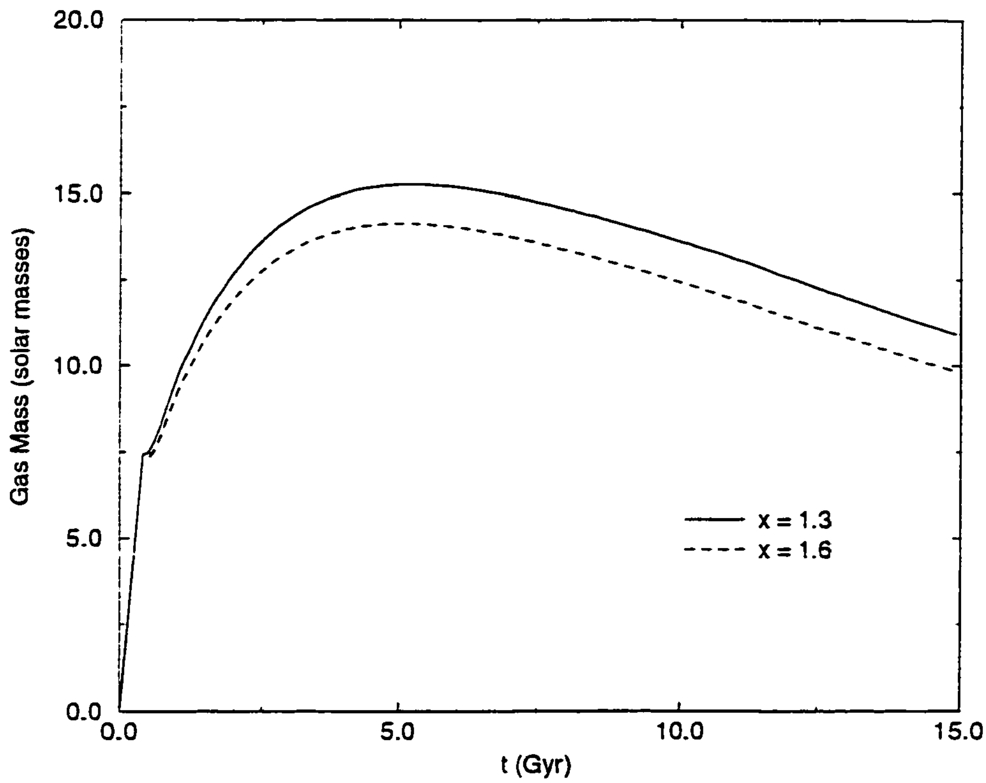

Figure 4.7: Plot of gas mass against time with a changing IMF. The slope parameter for the IMF is varied between either $x = 1.3$ and $x = 1.6$ as indicated. Total mass is the same at all points, and the infall rate is the same in both cases.

both sets of calculations due to the identical infall rate. One expects the gas fraction to decline somewhat with a steeper IMF, since proportionately more gas formed into stars is stored in long-lived objects. This decline is shown in the figure, but the change is not as large as is required by the observed paucity of gas in early-type spirals. It is then evident that a change in IMF may be necessary to *widen* the spread in [N/O] between early and late types, but it is not sufficient to account for the [N/O] behavior while simultaneously affecting the gas fraction.

In Fig. 4.8, I show that the correlation between early-type spirals and an enhanced [N/O] is also still apparent if the upper stellar mass cutoff is $50M_\odot$ instead of $40M_\odot$. Due to the lack of SN yield data from Woosley and Weaver (1995) for these massive objects, I simply assume a uniform yield for stars of initial mass $40M_\odot < M < 50M_\odot$. This yield should be somewhat higher for the more massive stars, but this should be a lower limit to the additional material returned. The absolute value of [N/O] is decreased in both classes of galaxies, since increasing the upper-mass cutoff allows for additional high-mass stars to be formed. These stars will primarily generate oxygen, and thus lower the overall [N/O] ratio. As discussed with the IMF previously, invoking a higher mass cutoff does not appreciably change the gas fraction, and so would not in and of itself satisfy the observational constraints. A plot similar to Fig. 4.7 could be shown to illustrate this point, but the change in gas fraction is too small to resolve.

I conclude, then, that early spiral galaxies once had a much greater accretion rate of gas, and a sharply higher SFR as well. The star formation rates in Fig. 4.1 show that the SFR has effectively stopped in early spirals and the enhancement in [N/O] is chiefly due to the delayed release of secondary N in the (still-evolving) low mass stars. These small stars were formed in greater numbers at early times in early galaxies due to the higher SFR, and are releasing their secondary nitrogen at later times. This results in [N/O] abundances in early spirals that are typically 0.05-0.1 dex above those in late spirals for a given $\log(O/H) + 12$ value, in agreement with the observed abundance ratios. This conclusion is physically appealing in that only one parameter must be varied. The other parameters, such as the upper-mass cutoff and the IMF, may well be different in these types of galaxies,

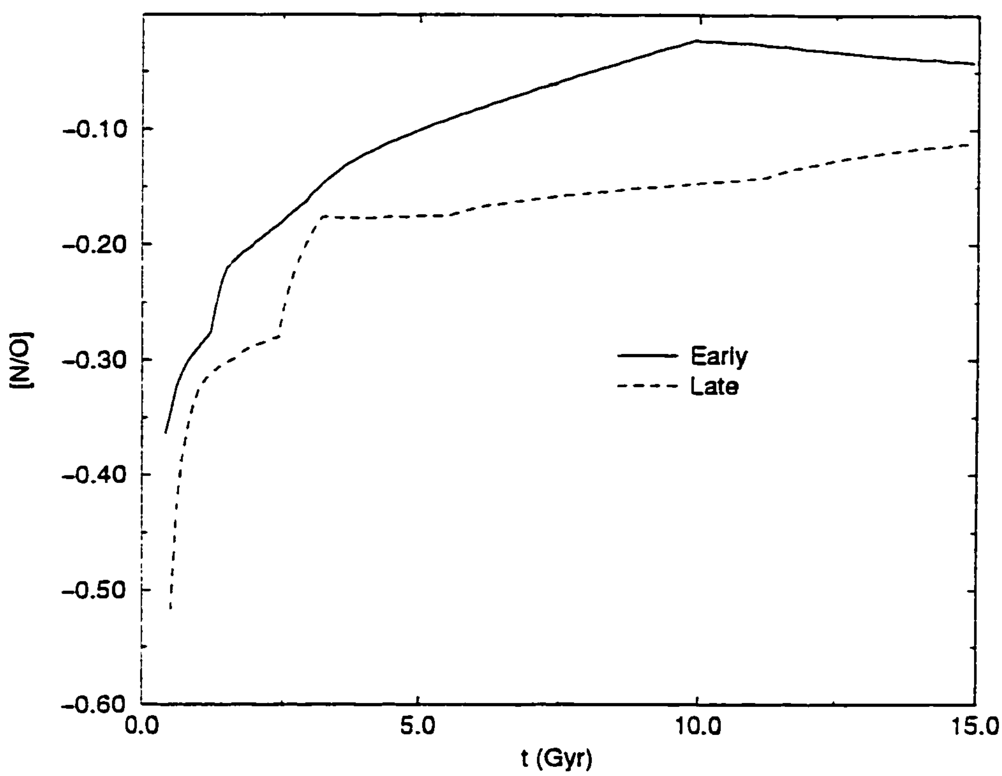

Figure 4.8: Plot of (N/O) evolution in early- and late-type spirals against time, with the upper stellar mass cutoff = $50M_{\odot}$.

but neither is sufficient to explain the [N/O] ratio difference while also accounting for observational gas-mass constraints. The physical properties that would induce differences in the latter two parameters are also poorly understood.

4.2 Results for Metal-Poor Galaxies

Since the discovery of very metal-poor HII regions in dwarf galaxies (Searle and Sargent (1972)), studies of these regions have been fruitful in understanding the early chemical evolution of galaxies as well as parameters governing the nucleosynthesis of primordial elements in the early universe. In some of these galaxies, only one HII region is observed. It is commonly assumed that the nebular abundances represent the chemical composition of the galaxy as a whole, but (as discussed in Chapter 3) the HII region may "self-pollute" on short timescales ($\sim 10^{6-7}$ years). It is interesting, though, that many low-mass galaxies seem to be chemically homogeneous among various HII regions, leading to questions regarding the temperature and observability of these new ejecta (see Kobulnicky (1997)). This pollution arises from very massive, short-lived stars during the current burst of star formation, and thus the observed abundance may not accurately reflect the galactic abundances for those elements typically generated in the deaths of massive stars (O, S, Fe, for example). There are competing effects due to supernova winds emanating from these explosions, creating voids near the event and bow-shaped concentrations along the wavefront. Observations and quantitative analyses of winds are difficult, and are treated in an indirect manner in this study by varying the SFR in the region affected. A working hypothesis is that these winds may introduce a change in the local SFR by disrupting self-gravitating systems and/or depleting the area of gas. The details of these interactions are not addressed here, however.

Kobulnicky and Skillman (1996) present observations of HII regions in NGC 4214, an irregular starburst galaxy similar to the Magellanic Clouds associated with our own galaxy, as well as tables of newly calculated abundances of [N/O] from a compilation of previous observations. From that compilation, which included the observations from a number of different groups, I chose the observations of Campbell, Terlevich and Melnick (1986) to model as well as including one well-studied region from NGC 4214 and the "famous" object I Zw 18 (original observations from Skillman and Kennicutt (1996)). The latter is well-known as the most metal-deficient HII galaxy yet identified. The calculated nitrogen abundances using our method (Chapter 3) are shown in § 3.4 and Fig. 3.14. I reproduce part of that diagram here in Fig. 4.9, and add the HII regions from our 10-galaxy sample in Chapter 3 as well as the theoretical data generated from the NICE code.

Of great interest are the two points from I Zw 18, with $\log(O/H) + 12 = 7.17, 7.26$ from Skillman and Kennicutt (1996) and the QSO observed by Pettini, Lipman and Hunstead (1995). The latter object has a large 3σ uncertainty (skewed towards higher O/H — see reference for details) in $\log(O/H) + 12$, with a likely value around 7.0. The likely value is calculated by assuming [O/S] = 0, since the derived sulfur abundance is more tightly constrained than the oxygen abundance. This is probably a reasonable assumption, as oxygen and sulfur are in roughly solar proportions in HII regions of all metallicities measured in the surveys of Skillman and Kennicutt (1993) and Garnett and Kennicutt (1994). O and S are also manufactured in the same sites (massive stars, Woosley and Weaver (1995)), so it is not surprising that their relative numbers would be constant. [N/O] is very low in this QSO, with an *upper* limit of -1.24.

Table 4.3

Parameter	Value
Stopping time	15 Gyr
Present time	13 Gyr
Upper Mass cutoff	40 $M_\odot$
Lower Mass cutoff	0.08 $M_\odot$
SFR coefficient ν ($\log(O/H) + 12 < 7.20$)	0.15 $M_\odot$Gyr^{-1}
SFR coefficient ν ($\log(O/H) + 12 > 7.20$)	1.8 $M_\odot$Gyr^{-1}
IMF slope, below 10 $M_\odot$	1.3
IMF slope, above 10 $M_\odot$	1.3
Final mass density	100 $M_\odot$
Initial gas mass density	50 $M_\odot$
Exponential infall parameter τ_d	6.0

Table 4.3: Table of input parameters for Fig. 4.9. Note the changing value for ν at $\log(O/H) + 12 = 7.20$.

Fig. 4.9 shows our newly calculated [N/O] abundances against the [O/H] abundance for the regions selected, as well as points calculated for a *single* hypothetical star-forming region over time via the NICE chemical evolution code detailed in Chapter 2. The solid lines represent a temporal sequence of calculations for a star-forming region with an initially primordial gas mass and standard infall (see the input parameters for this group of models given in Table 4.3). The straight lines show the least-square fits to the abundance ratios, as in Fig. 3.11. The solid curves are generated by NICE with purely primary and secondary sources for nitrogen,

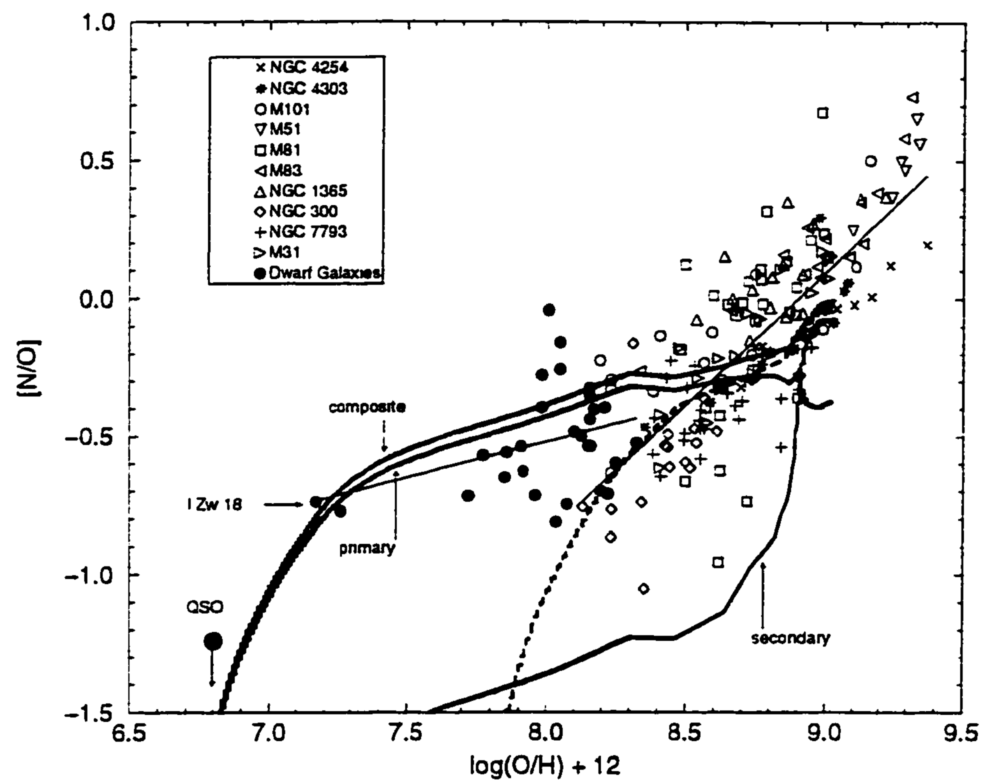

Figure 4.9: NICE model results (bold curves) plotted with observed abundance ratios (symbols) for our sample of HII regions observed in Chapter 3. The bold solid lines represent a temporal sequence of calculations for a star-forming region with an initially primordial gas mass and standard infall (see Table 4.3). Note the lower-leftmost point, taken from a primeval galaxy at a redshift of $z \approx 2.3$. There is a large uncertainty regarding the [O/H] abundance of this object (see Pettini, Lipman and Hunstead (1995)), with the point indicating the most likely value. The point also illustrates the upper limit to [N/O]. The straight lines show the least-square fits to the abundance ratios, as in Fig. 3.11. The solid curves are generated by NICE with purely primary and secondary sources for nitrogen, as indicated. The remaining solid curve (marked "composite") represents the total [N/O] vs. [O/H] computed using both primary and secondary nitrogen yields. The dashed curve indicates model results with the same input parameters as the latter composite solid curve, except for no initial SFR coefficient suppression.

as indicated. The remaining solid curve (marked "composite") represents the total [N/O] vs. [O/H] computed using both primary and secondary nitrogen yields. The dashed curve indicates model results with the same input parameters as the latter composite solid curve, except for no initial SFR coefficient suppression (to be discussed below).

The agreement between the observed objects and the solid-line calculations is good, although there is a large (probably intrinsic) scatter in the observed data. This scatter and its relation to the input parameters will be addressed below, as will the importance of the primary and secondary lines. Note that in this figure, I do not claim to precisely fit the spiral HII regions, since they are members of very different systems than those of dwarf galaxies. Rather, what is important to understand from this plot is that it is possible to model the characteristic abundances of metal-poor HII galaxies while also predicting behavior similar to that shown by the spiral regions. Considering that in the single model O/H increases with time, the plot behavior suggests that dwarf galaxies are chemically less evolved, while spirals are chemically more advanced. This follows from the trend in the models to display primary nitrogen behavior at early times, and to show more secondary nitrogen generation at later times. This will be discussed further in § 4.4. I do not suggest differences in relative ages between spiral HII regions as being the sole cause for the steep slope in [N/O] vs O/H, however, as the [N/O] trend certainly may depend (indirectly) on environmental parameters such as the IMF slope and the upper stellar mass cutoff (as discussed in the previous section) and changes in the local SFR over time. Future work will focus on modeling the trends in HII regions for individual galaxies, to determine possible systematic variations in these parameters. Modeling the overall [N/O] ratio in spirals is addressed in the next section.

Considering only the composite line (computed with both primary and secondary nitrogen generation mechanisms), note that the models predict a sharp rise in [N/O] at low O/H values. This is induced by requiring a suppression of the SFR coefficient ν at extremely early epochs. The value of $\nu = 0.15$ was chosen to fit the metal-poor galaxy points. The later value of $\nu = 1.8$ was chosen to fit current observational constraints including the SN rate and gas mass fraction (see § 2.2.2). The justification behind the introduction of this (artificial?) process can be seen in the figure. NICE assumes only H and He initially as the gas accretes onto the star-forming region, so immediately after the first stars are born there are no metals in the local ISM. The first stars to evolve and return material to the ISM are the most massive ones, and these will typically release oxygen and sulfur in much greater quantities than nitrogen. The stars with masses $< 8M_{\odot}$ will return nitrogen at a later time. Therefore, one can understand the steep slope in [N/O] represented by the dashed line (the unsuppressed SFR model) in Fig. 4.9 as the initial enrichment of the ISM with nitrogen *after* some oxygen enrichment has already taken place. In order to fit the I Zw 18 regions, the SFR must then be suppressed during the time when only oxygen is returned to the ISM; otherwise the oxygen pollution raises the $\log(O/H)+12$ value beyond that of I Zw 18 before nitrogen is returned. The SFR reduction serves to decrease the amount of oxygen generated at this early time before nitrogen enrichment. The amount of oxygen enrichment in the "standard" model (no SFR depletion) is shown in Fig. 4.10, where the $\log(O/H) + 12$ and $\log(N/H) + 12$ ratios are plotted as a function of

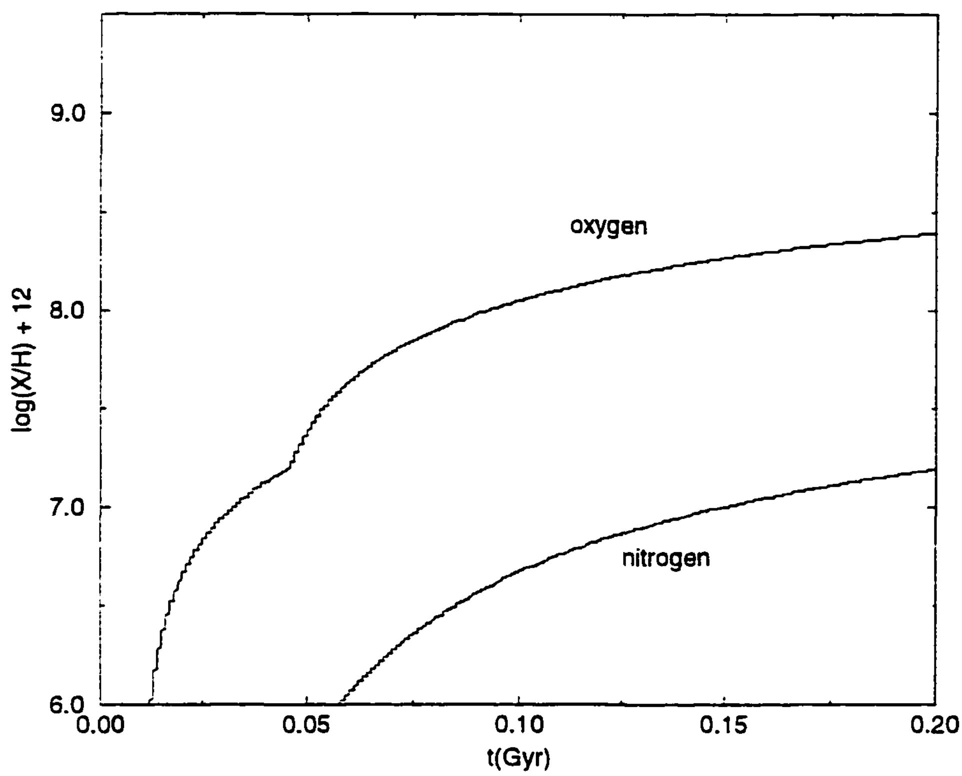

Figure 4.10: Plot showing the differing pollution rates of nitrogen and oxygen in a star-forming region as a function of time. Calculations from NICE with input parameters identical to those in Table 4.3.

time. Note that O/H reaches a value ≈ 7.5 before nitrogen production begins, a value greater than that observed in I Zw 18 and the QSO.

The dashed line in Fig. 4.9 shows a NICE model calculation without the initial SFR reduction. This line should be (with the stated initial parameters and yields) a theoretical minimum for [N/O] at a particular O/H, since the returned fraction of oxygen is considered in full with no reduction of massive star birthrates.

Observational support for this pollution scheme is given by the QSO point in Fig. 4.9. I hypothesize that in this QSO we are seeing some of the very first stars to be born in the region. There simply has not been enough time for sufficient numbers of stars of mass $< 8M_\odot$ (the stars that manufacture nitrogen) to evolve and return their processed elements. Additional determinations of abundances and environmental variables in these primeval systems would likely constrain the initial parameters of large star forming regions. A physical mechanism for the SFR depletion used above may be strong supernova winds that disrupt self-gravitating regions destined to produce stars, especially in dwarf systems where the ambient gravitational potential is weak and the winds are correspondingly strong.

In any case, if O/H remains fairly constant over these short timescales, one may use the discrepancy between observed [N/O] and the computed line (the dashed line in Fig. 4.9) to date the episode of star formation. This has also been suggested in Pettini, Lipman and Hunstead (1995).

It is also interesting to note in Fig. 4.9 that the best fit results from models that contain an initial gas mass, as opposed to the models that generated the best match to solar neighborhood quantities in Chapter 2. Earlier, the best models were those with no initial gas mass (in order to solve the G-dwarf problem). Fig. 4.11 shows this dependence, where the dataset is identical to Fig. 4.9. The solid line represents the NICE model region with the input parameters shown in Table 4.3, while the dashed line shows the model generated with the initial gas mass set to zero. The immediate conclusion is that a good fit to regions such as I Zw 18 requires some dilution of the initial star-forming gas with primordial material. As the G-dwarf population distribution of these galaxies is not determined, the obvious constraint to this parameter cannot be checked.

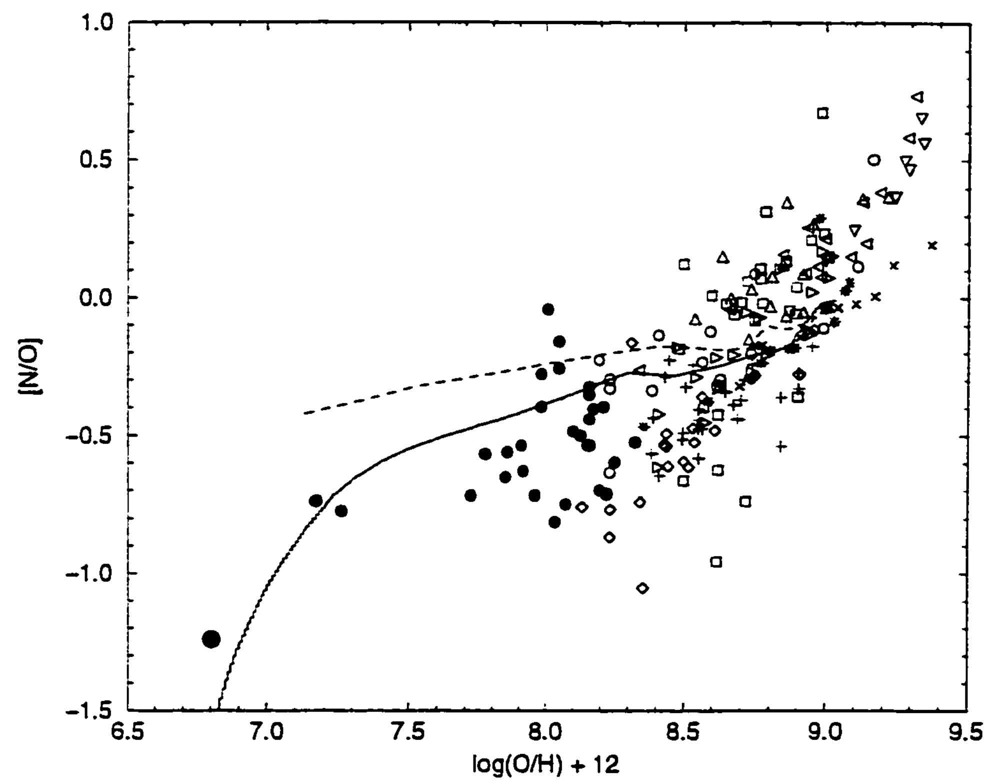

Figure 4.11: Dependence of the NICE models upon initial gas mass. The dashed line represents the model with no initial gas mass, while the solid line represents the model with an initial gas mass density of 50 $M_{\odot}$ (see Table 4.3). Symbols are identical to Fig. 4.9.

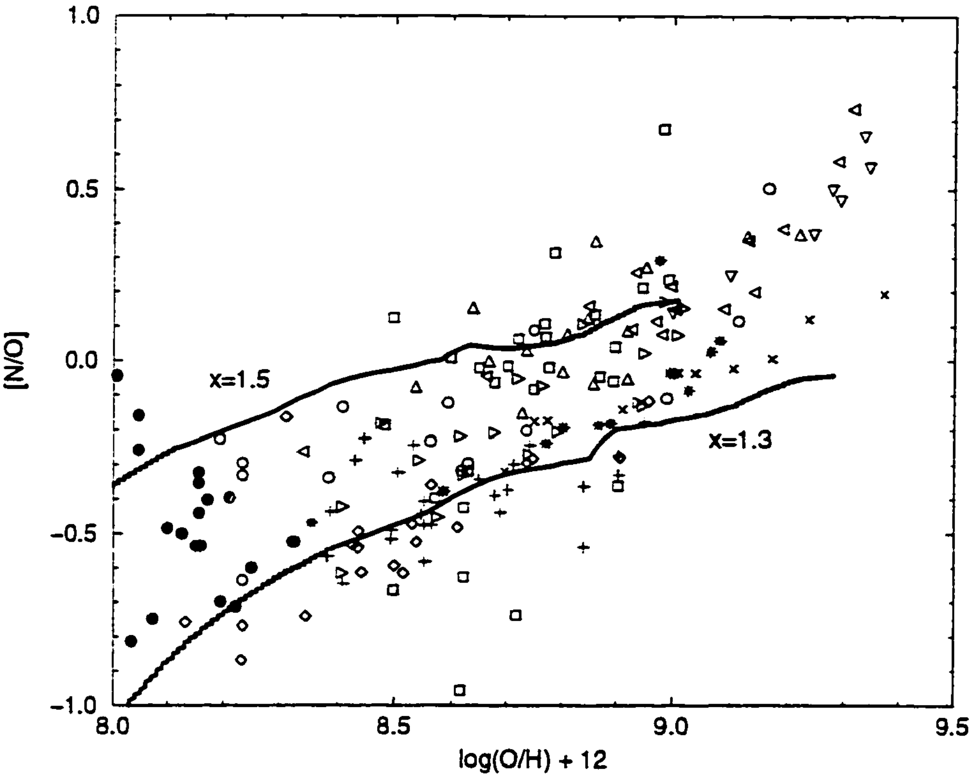

Figure 4.12: NICE model results for the spiral HII regions. The solid lines indicate models calculated with an IMF slope of 2.3 and 2.5 (as indicated, with the IMF slope = $-(1+x)$) for stars with masses $> 10M_{\odot}$.

4.3 Results for Spiral Galaxies

I will now revisit the sample of spiral galaxies presented in Chapter 3 in order to address the apparent trend of [N/O] vs. O/H in these relatively high-metallicity objects. The results of the best model fit to the data are shown in Fig. 4.12.

I shall briefly consider a model parameter that may be responsible for the scatter in the [N/O] vs. O/H plot. The initial mass function is the most likely candidate to cause changes in the [N/O] vs. O/H relation, since it directly alters the relative populations of the stars that generate these elements. Some scatter is surely due to systematic observational uncertainties, but some may be due to changes in quantities such as the IMF. Figs. 4.13 and 4.12 address this issue, and show the same galactic data as in Fig. 4.9. In Fig. 4.12, the points shown are the same as in Fig. 4.9, but only for the region $\log(O/H) + 12 > 8.0$. This region is populated with the calculated [N/O] data presented in Chapter 3 for spiral galaxy HII regions. The solid lines represent model calculations computed with two different values for the massive-star IMF. Recall from Chapter 2 that NICE is capable of describing an IMF with different slopes for low- and high-mass stars. Here I vary the massive star (stellar masses $> 10M_{\odot}$) IMF slope from 2.3 to 2.5. Note that most of the scatter in [N/O] abundances is contained within this variation, however the corresponding scatter in O/H is slightly smaller in the observations. If the IMF actually varied among spirals in this manner, one might expect to observe more HII regions at high O/H ($\log(O/H) + 12 > 9.0$) with solar [N/O]. It seems, however, that the models accurately represent the trend in the observational data, at least to $\log(O/H) + 12 = 9.0$. At this point, there is a hint that the [N/O] vs. O/H relation steepens somewhat. Further observations of hyper-solar metallicity HII regions might reveal this change in slope. These metal-rich objects could not be modeled via variations of input parameters — the oxygen abundance saturates at roughly solar values, and then begins to decrease with time as new star formation and intermediate-mass stellar evolution subtract oxygen from the ISM. Using models with metal-rich infall scenarios were not adequate as the infall tends to drive the overall abundance to the metallicity of the infalling material.

A best-fit line to the spiral data (excluding the regions with greater than solar metallicity) would have $x \approx 1.4$, and it is useful to briefly discuss the implications of this IMF in light of the model constraints given in Chapter 2. With this slightly steeper IMF, fewer massive stars exist to generate oxygen. It is found that increasing the massive star integration cutoff from $40M_{\odot}$ to $50M_{\odot}$ will again produce solar abundance ratios for the input parameters in Chapter 2, with a negligible impact upon the G-dwarf constraint. This new cutoff is well within the limit specified by Tsujimoto et al. (1997).

Changing the IMF slope for low-mass stars (masses $< 10M_{\odot}$) is attempted in Fig. 4.13. The solid line represents the same "best fit" model as in Fig. 4.9, but the two dashed lines show models calculated with a changing low-mass IMF. In Fig. 4.9, the IMF has a slope parameter of 1.3 for all mass ranges. Here, I set the IMF = 1.1 and 1.6 (as indicated in the plot) for the low-mass range. Note that the scatter in [N/O] is approximately spanned for regions with $8.0 < O/H < 9.0$. For the upper curve, the IMF slope for this mass region is shallower than for the other two curves. This implies that a larger proportion of low-mass stars are born in a given stellar population, and therefore, more nitrogen is generated when these stars evolve (and consequently less oxygen, as there are fewer high-mass stars). The opposite is true for the lower curve, as a steeper slope favors higher-mass stars and less nitrogen (and more oxygen).

The physical parameters governing the slope of the IMF are not well understood, so that invoking a non-standard IMF shape becomes something of an *ad-hoc* procedure. These low-metallicity regions also may be subject to a higher degree of intrinsic scatter due to the fact that nitrogen is injected into the local medium with an order of magnitude less oxygen than in the spiral HII regions.

An interesting possibility for future study by NICE is the hypothesis that the scatter in [N/O] is due to an intermittent star-formation history. This is detailed in Kobulnicky and Skillman (1997), and postulates that [N/O] will vary over short timescales based upon the delayed release of nitrogen. As discussed before, since nitrogen comes from less massive stars than does oxygen, it will be delayed $\sim 10^8$ years with respect to oxygen. Massive stars will return oxygen to the ISM, driving the [N/O] ratio down. Later, when the nitrogen is ejected from intermediate-mass stars, and the massive star formation is ending, the [N/O] ratio will climb. Successive bursts of these events may drive [N/O] up over a long period of time. It seems unlikely that such a wide and uniform scatter as is seen in the [N/O] vs. O/H plots is completely described by such short-timescale phenomena, however it may be partially responsible for the overall slope of the relation.

I suggest that the scatter in the diagram is partially due to differing IMFs in the host galaxies, since the [N/O] vs. O/H trend is modeled for those HII regions with solar metallicities or less. It is important to realize that changes of 0.1 in the IMF are probably impossible to determine observationally, especially for extragalactic objects. The utility of this chemical modeling, however, is to show the sensitivity shown by the [N/O] data upon small changes in the IMF. In addition, it is useful to consider the known effect that changes of the IMF will have on the chemical evolution of the galaxy.

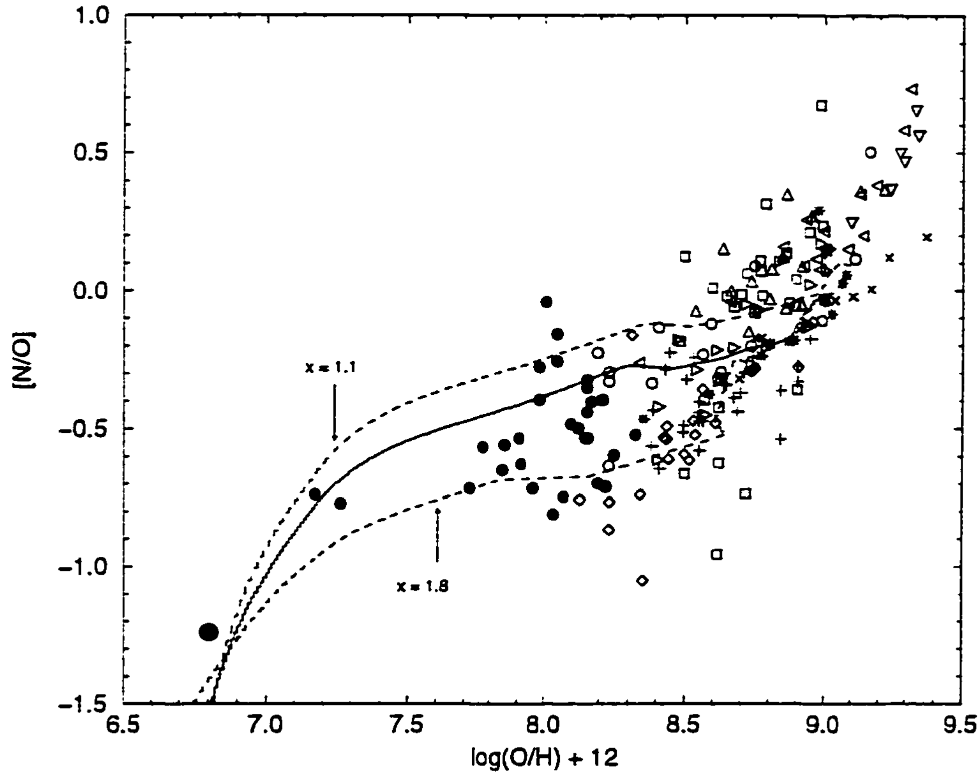

Figure 4.13: Dependence of the NICE models upon the IMF. The solid line is the same as in Fig. 4.9, with the IMF parameter = 1.3 for the entire mass range. The dashed lines represent models with the indicated IMF parameter for the low-mass region ($M < 10M_{\odot}$), where the IMF slope = $-(1 + x)$.

4.4 Primary vs. Secondary Nitrogen

I shall now address the issue regarding the nucleosynthetic origin of nitrogen. Fig. 4.14 shows the two calculated curves indicating the behavior of [N/O] with respect to the primary and secondary paradigms discussed earlier. The secondary curve is represented by the dashed line, while the primary curve is shown by the lower solid line. The third curve is the composite model (primary + secondary). The models suggest that nitrogen is chiefly generated by primary mechanisms until $\log(O/H) + 12 \approx 8.9$, when secondary nitrogen is released. This is also supported by Fig. 4.9, where the composite line mirrors primary behavior during early times. Examining the model output, this secondary contribution occurs at about $t = 1.3$ Gyr, when stars of about 2.0 $M_{\odot}$ have evolved. Here, the SFR has dropped sufficiently for the prompt oxygen production to be dominated by the sheer numbers of the low-mass stars returning secondary nitrogen to the ISM. Another factor, as is seen in Fig. 2.5 and Fig. 4.9, is the decline in primary nitrogen production in favor of the secondary mechanism at these metallicities. Note that the slope of the composite model at these late epochs mirrors the [N/O] vs. [O/H] slope found observationally (the solid line in the figure), supporting the hypothesis that this steep slope shows the effect of secondary nitrogen production.

These results follow from the study of the stellar yield tables of Buell (1997), shown in Fig. 4.15. Here the yields from Buell (1997) are plotted against initial stellar mass. This figure indicates that, at early galactic epochs, primary nitrogen production was dominant for stars with masses $4 < M < 8$ solar masses. These stars evolve faster and produce almost exclusively primary nitrogen. This primary nitrogen is generated from newly-synthesized carbon that has been "dredged"

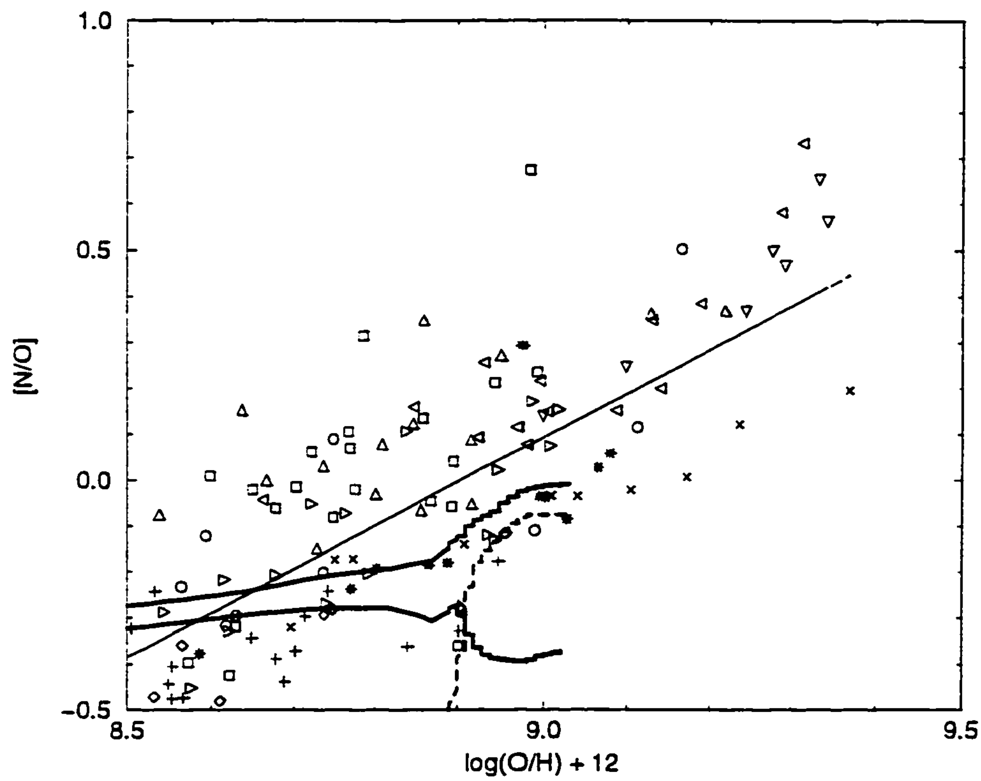

Figure 4.14: Detail of the primary/secondary nitrogen generation at late galactic times. This plot is a detailed view of the upper end of the $\log(O/H) + 12$ range in Fig. 4.9, where now the dashed line is the NICE model run with only secondary nitrogen generation. The lower solid curve represents the model with only primary nitrogen, and the upper curve is the composite model with both mechanisms. Symbols are identical to Fig. 4.9.

(more specifically, the 3rd dredge-up) into a fusion zone by convective processes. The conversion of this carbon ultimately into nitrogen occurs via the hot-bottom burning process. Secondary production dominates after $\sim 10^9$ years, as the small stars (which exist in greater numbers than massive stars) finally evolve and collectively return approximately an order of magnitude more nitrogen than the primary processes in massive stars. This secondary nitrogen is made from carbon and oxygen already present during the star's formation, and is manufactured during the 1st dredge process. For stellar evolutionary details, see Buell (1997). Note in the figure that primary production is virtually nonexistant in stars of less than 4 solar masses, so that these stars will contribute only secondary nitrogen. It is clear, then, that this yield will tend to increase in time, T as it is the nature of secondary mechanisms to generate more N as the ambient metallicity increases. This is also confirmation of the hypothesis that secondary nitrogen production is delayed in galaxies, perhaps by as much as 10^9 years (Chapter 3, Vila-Costas and Edmunds (1993) and references therein). The figure also shows that secondary production is virtually the only source for nitrogen in stars of less than 4 solar masses, as was discussed in Chapter 2 and in Buell (1997).

4.5 Summary

In this chapter, I applied the numerical isotopic chemical evolution (NICE) code to a small number of galactic situations. I found that a likely cause for the systematic difference in [N/O] ratios between early and late type spirals is a more sharply peaked infall rate for early galaxies. When normalized to the same final mass surface density, early types deplete most of the available gas quickly in the

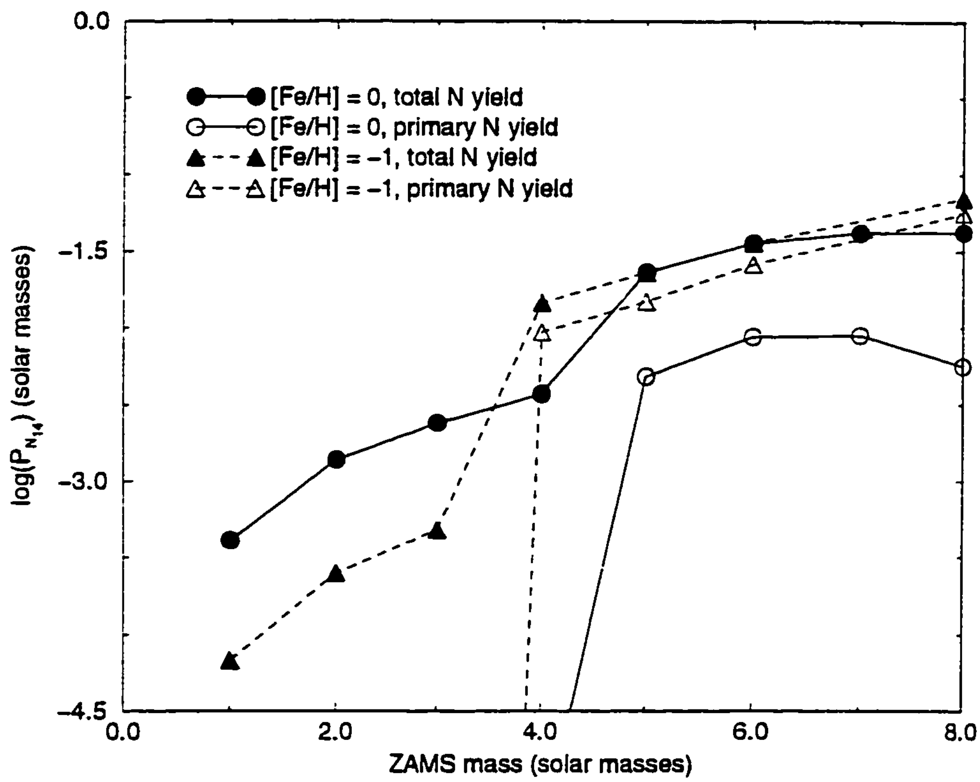

Figure 4.15: Yields from Buell (1997) showing the relative contributions from primary and secondary sources. The solid lines with circles represent a recent era (solar [Fe/H]) while the dashed lines with triangles represent a past era with [Fe/H] = -1. Filled shapes indicate total nitrogen yields, hollow shapes indicate the primary production.

first stellar generations. After approximately 2 billion years, smaller stars begin to dominate nitrogen production through the return of secondary nitrogen to the ISM. This conclusion remains valid when systematically varying the yields for oxygen and nitrogen, changing the slope of the IMF, and altering the upper stellar mass cutoff. The latter two parameters, while inducing a change in [N/O], cannot by themselves reproduce the observed gas fraction difference between early and late types. The infall scenario is the simplest solution to agree with the observational constraints.

I found that the code satisfactorily reproduces the [N/O] abundances for the set of HII regions in dwarf galaxies observed by Campbell, Terlevich and Melnick (1986), the starburst region in NGC 4214 (Kobulnicky and Skillman (1996)), I Zw 18 (observations by Skillman and Kennicutt (1996)), and a highly-redshifted QSO (Pettini, Lipman and Hunstead (1995)). A key component to the modeling of these regions is the introduction of a lower SFR at early times, possibly due to both the lower gravitational potential of these objects and supernova winds. The latter object is interesting, as it appears to have very recently undergone massive star formation. We are probably witnessing the first return of primary nitrogen immediately after the initial oxygen pollution from massive stars. The scatter and trends of [N/O] in Fig. 4.9 can be modeled with the introduction of a variable IMF for different galaxies, though this is probably a fine-tuning parameter. NICE is not able to model the high [N/O] metal-rich objects that show a possibly steeper slope against O/H.

Study of the yields tabulated by Buell (1997) and shown in Fig. 4.15 confirms that primary nitrogen is mainly returned by intermediate-mass stars with $4 <$

$M < 8$ solar masses, and was the dominant source of nitrogen early in the galaxy's history. Secondary nitrogen appears to be time-delayed, as it is almost exclusively generated in small stars, and is the main nitrogen production process at late times.

Chapter 5

Summary of Thesis Work

The mission of this research project is to more completely understand the processing of nitrogen over time in spiral galaxies. It is clear that a model of chemical evolution is necessary to evaluate the dependence of nitrogen evolution upon many free and interrelated parameters, and the numerical code NICE was written for that purpose. It was also necessary to assemble a large and consistent database of observed nitrogen abundances in order to compare the abundance calculations with those of observed HII regions. The numerical evolution code was then used to model the trends found in the observed data.

NICE is a numerical isotopic chemical evolution code written for this thesis in C++. It is a single-zone model, in that it treats the change of abundance over time of specific elements for a single cell of gas. This cell may have an analytic form of infall of material of arbitrary metallicity. The model is calculated in discrete time steps, numerically integrating the appropriate equations detailed in Chapter 2. Within each time step, subtractions from the mass of each isotope in the local environment are made due to star formation. The isotope mass is augmented by (possible) infall and isotopic yields from evolving stars. The specific assumptions common to most of the models computed for this dissertation are: an exponentially decreasing rate of infall with time, a Schmidt star formation rate (approximately proportional to the square of the local gas mass density), a SFR cutoff for gas mass densities of less than $7M_{\odot}$, a Salpeter IMF with a single slope for all mass ranges, and a free parameter c adjusting the rate of type Ia supernovae to match present-day iron abundances. The elemental yields are taken from three sources: Buell (1997) for yields of low- and intermediate-mass stars, Woosley and Weaver (1995) for massive star (type II SN) yields, and Nomoto et al. (1984) for the type Ia supernova nucleosynthesis.

NICE agrees well with the standard observational constraints such as the G-dwarf metallicity distribution, supernova rates, the age-metallicity relation, and modern solar abundance ratios, and is thus employed to model the evolution of nitrogen abundance ratios in HII regions.

It is desirable to possess a control database of the nitrogen abundances in extragalactic HII regions. The line strengths from 164 spiral HII regions and 29 dwarf galaxies were chosen from the literature in order to compute the nitrogen abundance ratios for these objects. The most important components involved in the abundance calculations are the line strengths and the electron temperatures in the emission regions. The original sources used standard temperature estimation methods in those cases where the temperature-sensitive emission lines are too weak to measure directly. In this dissertation, we implement a new algorithm to determine these temperatures using the usually strong optical emission lines of O^{++}. The environmental variables of hypothetical HII regions are entered into the photoionization code CLOUDY, which then produces a set of emission line strengths for the nebula. These input variables include the elemental abundance ratios, which are varied to cover a broadly plausible range of observed ratios. In particular, CLOUDY returns the strength of lines directly related to the electron temperature. A relation is found between the electron temperature and the optical oxygen lines, so that the N/O abundance ratio can be calculated via lines that are typically strong in spiral HII regions. This new algorithm is internally consistent and agrees well with previous studies that utilize a more detailed photoionization modeling technique.

Application of this algorithm to the previously existing line strengths yields (and confirms) three interesting results: the [N/O] ratio decreases with increasing galactocentric radius, [N/O] is slightly lower in late-type spirals relative to early galaxies, and the [N/O] vs. O/H relation is significantly steeper in spiral galaxies (approaching unity) than in dwarf galaxies. It is significant that the dwarf galaxies also have a lower overall metallicity than the spiral sample.

These observational results are addressed in the last chapter, where I apply the NICE code to model the environmental parameters that may be responsible for the observed trends in the [N/O] data. I conclude that a likely cause for the systematic difference in [N/O] ratios between early and late spirals is a more sharply peaked infall rate for early galaxies, resulting in an initially higher rate of star formation for the early galaxies. At later epochs, the [N/O] ratio in early spirals is higher due to the delayed release of nitrogen. The gas mass fraction is also significantly lower in early types, also matching observations.

The slope and the absolute [N/O] vs. O/H abundance ratio is modeled in dwarf galaxies by requiring an initial suppression of the SFR during early stages of star formation. This suppression is needed to allow the nitrogen enrichment to reach observed levels, since the prompt release of oxygen by massive stars increases the O/H mass fraction too quickly. This mechanism is introduced in order to model the I Zw 18 objects, but closely models the primeval galaxy as well. The spiral HII regions with $O/H < O/H_{\odot}$ are modeled with the standard set of input parameters, except for a slightly steeper massive-star IMF slope of 2.4. The HII regions with hyper-solar metallicity were not successfully modeled. The model results (which in turn directly depend upon the yields used) clearly show that primary nitrogen is released before secondary, since the primary mechanism is only dominant in stars of $4 - 8M_{\odot}$. Secondary nitrogen is generated in low-mass stars ($1 - 4M_{\odot}$), and is returned later in the history of the galaxy. Dwarf HII regions, having an overall lower metallicity and thus a shorter history of star formation, show mainly primary nitrogen production. Spiral regions are thought to be more advanced chemically, and show the characteristic steep slope of secondary nitrogen production, although this could also be related to a systematic variation of mean stellar ages across the galactic disks.

Bibliography

[Anders and Grevesse (1989)] Anders, E., Grevesse, N. *Geochim. Cosmochim. Acta*, 53, 197.

[Alloin *et al* (1981)] Alloin, D., Edmunds, M.G., Lindblad, P.O., and Pagel, B.E.J. 1981, *Astronomy and Astrophysics*, 101, 377

[Blair *et al* (1982)] Blair, W.P., Kirshner, R.P., and Chevalier, R.A. 1982, *Astrophysical Journal*, 254, 50

[Buell (1997)] Buell, J.B., *Ph.D. Thesis, University of Oklahoma*, 1997.

[Campbell, Terlevich and Melnick (1986)] Campbell, Alison, Terlevich, Roberto and Melnick, Jorge 1986, *Monthly Notices of the Royal Astronomical Society*, 223, 811.

[Carroll and Ostlie (1996)] Carroll, B.W. and Ostlie, D.A 1996, *Modern Astrophysics*, Addison-Wesley Publishing, p. 1010.

[Chiappini, Matteucci and Gratton (1996)] Chiappini, C., Matteucci, F., and Gratton, R. 1996, *Astrophysical Journal*, 477, 765

[Díaz *et al* (1991)] Díaz, A.I., Terlevich, E., Vilchez, J.M., Pagel, B.E.J., and Edmunds, M.G. 1991, *Monthly Notices of the Royal Astronomical Society*, 253, 245

[Dennefeld and Kunth (1981)] Dennefeld, M. and Kunth, D. 1981, *Astronomical Journal*, 86, 989

[Dufour *et al* (1980)] Dufour, R.J., Talbot, R.J., Jr, Jensen, E.B., and Shields, G.A. 1980, *Astrophysical Journal*, 236, 119

[Edmunds and Pagel (1978)] Edmunds, M.G. and Pagel, B.E.J. 1978, *Monthly Notices of the Royal Astronomical Society*, 185, 77

[Edmunds and Pagel (1984)] Edmunds, M.G., and Pagel, B.E.J. 1984, *Monthly Notices of the Royal Astronomical Society*, 211, 507

[Edmunds (1989)] Edmunds, M.G. 1989, in *Evolutionary Phenomena in Galaxies*, p.356, eds Beckman, J.E. and Pagel, B.E.J., Cambridge University Press, Cambridge

[Edmunds (1990)] Edmunds, M.G. 1990, *Monthly Notices of the Royal Astronomical Society*, 246, 678

[Edvardsson et al. (1993)] Edvardsson, B., Andersen, J., Gustafsson, B., Lambert, D.L., Nissen, P.E., and Tomkin, J. 1993, *Astronomy and Astrophysics*, 275, 101

[Evans (1986)] Evans, I.N. 1986, *Astrophysical Journal*, 309, 544

[Ferland (1990)] Ferland, G.J. 1990, *Ohio State University Report* 90-02

[Garnett and Shields (1987)] Garnett, D.R. and Shields, G.A. 1987, *Astrophysical Journal*, 317, 82

[Garnett and Kennicutt (1994)] Garnett, D.R. and Kennicutt, R.C. 1994, *Astrophysical Journal*, 426, 123

[Gibson and Matteucci (1997)] Gibson, B.K., Matteucci, F. 1997, *Monthly Notices of the Royal Astronomical Society*, 291, L8

[Gratton et al. (1996)] Gratton, R., Carreta, E., Matteucci, F., Sneden, C. 1996, *Astronomy and Astrophysics*

[Greggio and Renzini (1983)] Greggio, L. and Renzini, A. 1983, *Astronomy and Astrophysics*, 118, 217

[Grevesse and Noels (1993)] Grevesse, N. and Noels, A. in *Origin and Evolution of the Elements*, ed. N. Prantzos, E., E. Vangioni-Flam, and M. Casse (Cambridge Univ. Press, p. 15)

[Henry *et al* (1992)] Henry, R.B.C., Pagel, B.E.J., Lasseter, D.F., Chincarini, G.L. 1992, *Monthly Notices of the Royal Astronomical Society*, 258, 321

[Henry (1993)] Henry, R.B.C. 1993, *Monthly Notices of the Royal Astronomical Society*, 261, 306.

[Henry *et al* (1994)] Henry, R.B.C., Pagel, B.E.J., Chincarini, G.L. 1994, *Monthly Notices of the Royal Astronomical Society*, 266, 421

[Henry and Howard (1995)] Henry, R.B.C. and Howard, J.W. 1995, *Astrophysical Journal*, 438, 170

[Henry (1997)] Henry, R.B.C. 1997, Invited review at workshop *Abundance Profiles: Diagnostic Tools for Galaxy History*, Quebec

[Kaler (1981)] Kaler, J.B. (1981), *Astrophysical Journal*, 244, 54

[Kennicutt (1989)] Kennicutt, R.C. 1989, *Astrophysical Journal*, 344, 685

[Kobulnicky and Skillman (1996)] Kobulnicky, H.A. and Skillman, E.D. 1996, *Astrophysical Journal*, 471, 211

[Kobulnicky (1997)] Kobulnicky, H.A. 1997, astro-ph/9711077

[Kobulnicky and Skillman (1997)] Kobulnicky, H.A. and Skillman, E.D. 1997, astro-ph/9709280

[Kunth and Sargent (1986)] Kunth, D. and Sargent, W.L.W. 1983, *Astrophysical Journal*, 273, 81

[Matteucci (1986)] Matteucci, F. 1986, *Monthly Notices of the Royal Astronomical Society*, 221, 911

[Matteucci and François (1989)] Matteucci, F. and François, P. 1989, *Monthly Notices of the Royal Astronomical Society*, 239, 885

[Mihalas (1972)] Mihalas, D. *Non-LTE Model Atmospheres for B and O Stars*, NCAR-TN/STR-76

[McCall *et al* (1982)] McCall, M.L., Rybski, P.M., and Shields, G.A. 1985, *Astrophysical Journal Supplement Series*, 57, 1

[Nissen (1995)] Nissen, P.E. 1995, in *Stellar Populations*, IAU Symposium 164, ed. P.C. van den Kruit and G. Gilmore, the Haghe, Kluwer, Dordrecht, p. 109

[Nomoto et al. (1984)] Nomoto, K., Thielemann, F.K., Yokoi, K. 1984, *Astrophysical Journal*, 286, 644

[Osterbrock (1988)] Osterbrock, D. E. *The Astrophysics of Gaseous Nebulae and Active Galactic Nuclei* University Science Books, 1988, p120-1

[Pagel and Patchett 1975] Pagel, B.E.J., and Patchett, B.E., *Monthly Notices of the Royal Astronomical Society*, 172, 13

[Pagel *et al* (1979)] Pagel, B.E.J., Edmunds, M.G., Blackwell, D.A., Chun, M.S., Smith, G. 1979, *Monthly Notices of the Royal Astronomical Society*, 189, 95

[Pagel *et al* (1992)] Pagel, B.E.J., Simonsen, E.A., Terlevich, R.J., Edmunds, M.G. 1992, *Monthly Notices of the Royal Astronomical Society*, 255, 325

[Pettini, Lipman and Hunstead (1995)] Pettini, Max; Lipman, Keith and Hunstead, R.W. 1995, *Astrophysical Journal*, 451, 100

[Popper (1980)] Popper 1980, *Annual Reviews of Astronomy and Astrophysics*, 18, 115

[Rayo *et al*(1982)] Rayo, J.F., Peimbert, M., and Torres-Peimbert, S. 1982, *Astrophysical Journal*, 255, 1

[Renzini and Voli (1981)] Renzini, A. and Voli, M., *Astronomy and Astrophysics*, 94, 175

[Rocha-Pinto and Maciel (1996)] Rocha-Pinto, H.J., Maciel, W.J., 1996, *Monthly Notices of the Royal Astronomical Society*, 279, 447

[Rubin, Ford and Whitmore (1984)] Rubin, V.C., Ford, W.K. Jr., and Whitmore, B. 1984, *Astrophysical Journal*, 281, L21

[Salpeter (1955)] Salpeter, E.E. 1955, *Astrophysical Journal*, 121, 161

[Sandage and Carlson (1983)] Sandage, A. and Carlson, G. 1983, *Astrophysical Journal*, 267, L25

[Scalo (1986)] Scalo, J.M. 1986, *Fundamentals of Cosmic Physics*, 11, 1

[Schaller et al. (1992)] Schaller, G., Schaerer, D., Meynet, G. and Maeder, A. 1992, *Astronomy and Astrophysics*, 96, 269

[Schmidt (1959)] Schmidt, M. 1959, *Astrophysical Journal*, 129, 243

[Schmidt (1963)] Schmidt, M. 1963, *Astrophysical Journal*, 137, 758

[Searle and Sargent (1972)] Searle, L. and Sargent, W.L.W. 1972, *Astrophysical Journal*, 173, 25

[Serrano and Peimbert (1983)] Serrano, A. and Peimbert, M. 1983, *Rev Mex AA*, 8, 117

[Shields and Kennicutt (1995)] Shields, J.C. and Kennicutt, R.C. 1995, *Astrophysical Journal*, 454, 807

[Skillman (1989)] Skillman, E.D. 1989, *Astrophysical Journal*, 347, 883

[Skillman and Kennicutt (1993)] Skillman, E.D. and Kennicutt, R.C. 1993, *Astrophysical Journal*, 411, 655

[Skillman and Kennicutt (1996)] Skillman, E.D. and Kennicutt, R.C. 1996, *Astrophysical Journal*, 411, 655

[Smith (1975)] Smith, H.D. 1975, *Astrophysical Journal*, 199, 571

[Stauffer and Bothun (1984)] Stauffer, J.R., and Bothun, G.D. 1984, *Astronomical Journal*, 89, 1702

[Stasińska (1990)] Stasińska, G. 1990, *Astronomy and Astrophysics Supplement Series*, 83, 531

[Thielemann et al. (1993)] Thielemann, F.K., Nomoto, K., Hashimoto, M. 1993, in *Origin and Evolution of the Elements*, eds. N. Prantzos, E. Vangioni-Flam and M. Casse, p. 297, Cambridge University Press

[Thurston, Edmunds and Henry (1996)] Thurston, T.R., Edmunds, M.G. and Henry, R.B.C. 1996, *Monthly Notices of the Royal Astronomical Society*, 283, 990

[Timmes, Woosley and Weaver (1995)] Timmes, F. X., Woosley, S. E., and Weaver, Thomas A. *Astrophysical Journal Supplement Series*, 98, 617

[Tinsley (1980)] Tinsley, B.M., *Fundamentals of Cosmic Physics*, 1980, Vol. 5, pp. 287-388

[Tosi (1996)] Tosi, Monica astro-ph/9512096

[Tsujimoto et al. (1995)] Tsujimoto, T., Nomoto, K., Yoshii, Y., Hashimoto, M., Yanagida, S. and Thielemann, F. 1995, *Monthly Notices of the Royal Astronomical Society*, 277, 945

[Tsujimoto et al. (1997)] Tsujimoto, T., Yoshii, Y., Nomoto, K., Matteucci, F., Thielemann, F. and Hashimoto, M. 1997, astro-ph/9702205

[Tully (1988)] Tully, R.B. 1988, *Nearby Galaxy Catalogue*, Cambridge University Press, Cambridge.

[van den Bergh and McClure (1994)] van den Bergh, S. and McClure, R.D. 1994, *Astrophysical Journal*, 425, 205 [van den Hoek and Groenewegen (1996)] van den Hoek, L.B., and Groenewegen, M.A.T., *Astronomy and Astrophysics Supplement Series*, 123, 305

[Vila-Costas and Edmunds (1992)] Vila-Costas, M. B. and Edmunds, M. G. 1992, *Monthly Notices of the Royal Astronomical Society*, 259, 121

[Vila-Costas and Edmunds (1993)] Vila-Costas, M. B. and Edmunds, M. G. 1993, *Monthly Notices of the Royal Astronomical Society*, 265, 199

[Webster and Smith (1983)] Webster, B.L., and Smith, M.G. 1983, *Monthly Notices of the Royal Astronomical Society*, 204, 743

[Woosley and Weaver (1986)] Woosley, S.E. and Weaver, T.A., 1986, *IAU Colloquium 89*, eds. D. Mihalas and K. H. Winkler, Reidel, Dordrecht, p. 91

[Woosley and Weaver (1995)] Woosley, S.E. and Weaver, T.A., 1995, *Astrophysical Journal Supplement Series*, 101, 181

[Zaritsky et al. 1989] Zaritsky, D., Elston, R., and Hill, J.M., *Astronomical Journal*, 97, 1

[Zaritsky et al. 1990] Zaritsky, D., Elston, R., and Hill, J.M., *Astronomical Journal*, 99, 4

Appendix A

Tables of Results from Nitrogen Algorithm

This is the calculated data for all the galactic regions in this thesis, as generated by the new nitrogen abundance algorithm detailed in Chapter 3. In each table, the first column gives the name of the observed region (where applicable), the second gives the galactrocentric radius in units of the effective radius, the third shows the new calculated [N/O] ratio, the fourth shows the calculated [NII] electron temperature in the emission region, and the last column cites the appropriate reference for observational data.

Table A.1: Data for NGC 4254

Object	$\frac{R}{R_{eff}}$	[N/O]	[NII] Temp	Reference
142	0.42	0.195	6553	Henry *et al* (1994)
78	0.75	0.007	6396	Henry *et al* (1994)
173	0.75	0.121	6356	Henry *et al* (1994)
116	1.13	-0.022	6531	Henry *et al* (1994)
134	1.40	-0.035	6745	Henry *et al* (1994)
185	1.70	-0.034	6880	Henry *et al* (1994)
184	2.01	-0.140	7460	Henry *et al* (1994)
84	2.12	-0.172	7918	Henry *et al* (1994)
22	2.49	-0.320	8177	Henry *et al* (1994)
12	2.66	-0.174	7993	Henry *et al* (1994)

Table A.1: The columns represent the HII region name, the galactrocentric distance in units of the effective radius, the computed [N/O] relation, the computed NII temperature, and the appropriate reference for observational data.

Table A.2: Data for NGC 4303

Object	$\frac{R}{R_{eff}}$	[N/O]	[NII] Temp	Reference
95	0.39	0.058	6603	Henry *et al* (1992)
115	0.73	-0.085	6800	Henry *et al* (1992)
155	0.74	0.027	6655	Henry *et al* (1992)
51	0.81	-0.185	7638	Henry *et al* (1992)
175	0.81	-0.038	6917	Henry *et al* (1992)
76	0.85	-0.181	7577	Henry *et al* (1992)
53	0.87	0.292	7054	Henry *et al* (1992)
103	0.96	-0.035	6953	Henry *et al* (1992)
124	1.18	-0.192	7831	Henry *et al* (1992)
148	1.40	-0.237	7929	Henry *et al* (1992)
278	2.30	-0.377	8580	Henry *et al* (1992)
234	2.58	-0.468	9552	Henry *et al* (1992)

Table A.2: The columns represent the HII region name, the galactrocentric distance in units of the effective radius, the computed [N/O] relation, the computed NII temperature, and the appropriate reference for observational data.

Table A.3: Data for M101

Object	$\frac{R}{R_{eff}}$	[N/O]	[NII] Temp	Reference
S1	0.46	0.502	6405	Smith (1975)
H108+111	0.55	0.115	6508	Rayo *et al*(1982)
Smith 3	0.92	0.089	7998	Smith (1975)
H40	0.97	-0.201	8043	Rayo *et al*(1982)
H47	1.20	-0.109	6981	Rayo *et al*(1982)
H69-24	1.47	-0.121	8548	Rayo *et al*(1982)
NGC 5461	1.56	-0.337	9411	Smith (1975)
H69-23	1.58	-0.317	8457	Rayo *et al*(1982)
H69-142	1.67	-0.233	8658	Rayo *et al*(1982)
NGC 5462	1.98	-0.134	9306	Smith (1975)
NGC 5449	2.12	-0.296	8414	Smith (1975)
NGC 5447	2.44	-0.226	10315	Smith (1975)
Smith 12	2.67	-0.330	10112	Smith (1975)
S12	3.04	-0.295	10771	Smith (1975)
NGC 5471	3.81	-0.635	10707	Rayo *et al*(1982)

Table A.3: The columns represent the HII region name, the galactrocentric distance in units of the effective radius, the computed [N/O] relation, the computed NII temperature, and the appropriate reference for observational data.

Table A.4: Data for M51

Object	$\frac{R}{R_{eff}}$	[N/O]	[NII] Temp	Reference
...	0.39	0.561	6483	McCall *et al* (1982)
...	0.80	0.497	6377	McCall *et al* (1982)
CCM 72	0.85	0.367	6357	Díaz *et al* (1991)
CCM 24	0.86	0.246	6546	Díaz *et al* (1991)
CCM 19	0.88	0.652	6460	Díaz *et al* (1991)
CCM 71	0.94	0.466	6393	Díaz *et al* (1991)
CCM 10	1.04	0.138	6928	Díaz *et al* (1991)

Table A.4: The columns represent the HII region name, the galactrocentric distance in units of the effective radius, the computed [N/O] relation, the computed NII temperature, and the appropriate reference for observational data.

Table A.5: Data for M81

Object	$\frac{R}{R_{eff}}$	[N/O]	[NII] Temp	Reference
HK 74	1.43	0.674	7009	Stauffer and Bothun (1984)
HK 169	1.07	0.106	7938	Stauffer and Bothun (1984)
HK 305	1.07	0.315	7882	Stauffer and Bothun (1984)
HK 361	0.95	-0.061	8245	Stauffer and Bothun (1984)
HK 385	0.98	-0.045	7632	Stauffer and Bothun (1984)
HK 453	1.36	-0.015	8156	Stauffer and Bothun (1984)
HK 740	1.64	0.062	8094	Stauffer and Bothun (1984)
HK 744	1.73	-0.021	8343	Stauffer and Bothun (1984)
HK 755	1.64	0.009	8529	Stauffer and Bothun (1984)
M81 A	1.84	0.123	8926	Stauffer and Bothun (1984)
HK 472	0.86	0.212	7227	Garnett and Shields (1987)
13	0.93	0.235	6963	Garnett and Shields (1987)
14	1.05	-0.058	7569	Garnett and Shields (1987)
2	1.07	-0.020	7912	Garnett and Shields (1987)
12	1.09	-0.081	7999	Garnett and Shields (1987)
3	1.11	0.069	7933	Garnett and Shields (1987)
1	1.16	0.041	7552	Garnett and Shields (1987)
11	1.20	0.134	7659	Garnett and Shields (1987)
9	1.27	-0.360	7511	Garnett and Shields (1987)
5	1.29	-0.319	8415	Garnett and Shields (1987)
10	1.41	-0.397	8627	Garnett and Shields (1987)
4	1.64	-0.664	8921	Garnett and Shields (1987)
7	1.75	-0.737	8102	Garnett and Shields (1987)
17	1.89	-0.956	8462	Garnett and Shields (1987)
Münch 18	2.11	-0.185	8986	Garnett and Shields (1987)
HK 537	2.34	-0.626	8445	Garnett and Shields (1987)
Münch 1	3.41	-0.425	10817	Garnett and Shields (1987)

Table A.5: The columns represent the HII region name, the galactrocentric distance in units of the effective radius, the computed [N/O] relation, the computed NII temperature, and the appropriate reference for observational data.

Table A.6: Data for M83

Object	$\frac{R}{R_{eff}}$	[N/O]	[NII] Temp	Reference
2	0.01	0.733	6423	Webster and Smith (1983)
10	0.51	0.216	6949	Webster and Smith (1983)
11	0.52	0.200	6447	Webster and Smith (1983)
12	0.54	-0.043	8300	Webster and Smith (1983)
13	0.54	0.077	7028	Webster and Smith (1983)
14	0.57	0.256	7306	Webster and Smith (1983)
16	0.86	0.159	7694	Webster and Smith (1983)
17	0.86	0.151	6582	Webster and Smith (1983)
I	0.15	0.582	6387	Dufour *et al* (1980)
II	0.33	0.384	6376	Dufour *et al* (1980)
III	0.46	0.349	6469	Dufour *et al* (1980)
V	0.97	0.092	7350	Dufour *et al* (1980)
VI	1.18	0.149	6907	Dufour *et al* (1980)
S5	0.42	0.115	7086	Dufour *et al* (1980)
S10	0.82	-0.263	9620	Dufour *et al* (1980)

Table A.6: The columns represent the HII region name, the galactrocentric distance in units of the effective radius, the computed [N/O] relation, the computed NII temperature, and the appropriate reference for observational data.

Table A.7: Data for NGC 1365

Object	$\frac{R}{R_{\rm eff}}$	[N/O]	[NII] Temp	Reference
3	1.10	-0.051	7393	Pagel *et al* (1979)
4	2.12	-0.065	7667	Pagel *et al* (1979)
8	3.69	-0.149	8067	Pagel *et al* (1979)
L7	2.30	0.088	7406	Alloin *et al* (1981)
L15	2.19	-0.075	8765	Alloin *et al* (1981)
L28	1.57	0.032	8044	Alloin *et al* (1981)
L6	1.57	0.153	8388	Alloin *et al* (1981)
L3	0.07	-0.030	7834	Alloin *et al* (1981)
L11	0.22	0.363	6471	Alloin *et al* (1981)
L4	0.26	0.369	6358	Alloin *et al* (1981)
L33	0.44	0.350	7658	Alloin *et al* (1981)
L10	0.99	0.124	7696	Alloin *et al* (1981)
L17d	1.32	0.272	7184	Alloin *et al* (1981)
L21	2.27	0.078	7810	Alloin *et al* (1981)
L24	3.69	0.000	8281	Alloin *et al* (1981)

Table A.7: The columns represent the HII region name, the galactrocentric distance in units of the effective radius, the computed [N/O] relation, the computed NII temperature, and the appropriate reference for observational data.

Table A.8: Data for NGC 300

Object	$\frac{R}{R_{eff}}$	[N/O]	[NII] Temp	Reference
1	0.14	-0.278	7492	Webster and Smith (1983)
2	0.22	-0.359	8657	Webster and Smith (1983)
4	0.57	-0.481	8484	Webster and Smith (1983)
5	0.67	-0.533	9227	Webster and Smith (1983)
6	0.71	-0.282	8004	Webster and Smith (1983)
7	0.79	-0.615	8855	Webster and Smith (1983)
8	0.83	-0.472	8789	Webster and Smith (1983)
10	1.07	-0.163	9748	Webster and Smith (1983)
11	1.09	-0.494	9179	Webster and Smith (1983)
12	1.11	-0.741	9597	Webster and Smith (1983)
14	2.11	-0.867	10117	Webster and Smith (1983)
15	2.13	-0.767	10105	Webster and Smith (1983)
16	2.19	-1.053	9554	Webster and Smith (1983)
2	0.37	-0.293	8038	Edmunds and Pagel (1984)
1	0.75	-0.594	8917	Pagel *et al* (1979)
5	0.79	-0.540	9187	Pagel *et al* (1979)
W21	0.83	-0.525	8760	Pagel *et al* (1979)
W23	0.85	-0.116	7153	Pagel *et al* (1979)
4	1.75	-0.613	9159	Pagel *et al* (1979)
7	2.09	-0.758	10635	Pagel *et al* (1979)

Table A.8: The columns represent the HII region name, the galactrocentric distance in units of the effective radius, the computed [N/O] relation, the computed NII temperature, and the appropriate reference for observational data.

Table A.9: Data for NGC 7793

Object	$\frac{R}{R_{eff}}$	[N/O]	[NII] Temp	Reference
23	0.39	-0.329	7504	Webster and Smith (1983)
83	0.52	-0.362	7715	Webster and Smith (1983)
36	0.60	-0.516	8944	Webster and Smith (1983)
44	0.68	-0.298	8121	Webster and Smith (1983)
25	0.68	-0.389	8242	Webster and Smith (1983)
25N	0.68	-0.474	8653	Webster and Smith (1983)
19+26+24	0.72	-0.372	8160	Webster and Smith (1983)
20S	0.78	-0.539	7715	Webster and Smith (1983)
13	0.99	-0.490	8933	Webster and Smith (1983)
13S1	0.99	-0.242	8022	Webster and Smith (1983)
13S2	0.99	-0.444	8722	Webster and Smith (1983)
10	1.22	-0.582	8701	Webster and Smith (1983)
39	1.32	-0.272	7502	Webster and Smith (1983)
2	1.59	-0.566	9417	Webster and Smith (1983)
1	1.77	-0.343	8346	Webster and Smith (1983)
133	1.92	-0.288	9208	Webster and Smith (1983)
W12	0.33	-0.177	7202	Edmunds and Pagel (1984)
W2	0.58	-0.476	8702	Edmunds and Pagel (1984)
W5/6	0.86	-0.439	8205	Edmunds and Pagel (1984)
W13	1.40	-0.436	9394	Edmunds and Pagel (1984)
DV132	1.72	-0.225	9143	Edmunds and Pagel (1984)
W11	2.02	-0.646	9303	Edmunds and Pagel (1984)
...	0.38	-0.243	8785	McCall *et al* (1982)
...	0.82	-0.406	8702	McCall *et al* (1982)
...	1.56	-0.323	8892	McCall *et al* (1982)

Table A.9: The columns represent the HII region name, the galactrocentric distance in units of the effective radius, the computed [N/O] relation, the computed NII temperature, and the appropriate reference for observational data.

Table A.10: Data for M31

Object	$\frac{R}{R_{eff}}$	[N/O]	[NII] Temp	Reference
BA 75	0.71	0.022	7200	Blair *et al* (1982)
BA 423	0.74	0.171	6996	Blair *et al* (1982)
BA 289	0.96	0.074	6885	Blair *et al* (1982)
BA 1/2	1.42	-0.072	7948	Blair *et al* (1982)
BA 577	1.48	-0.204	7859	Blair *et al* (1982)
BA 379	1.84	-0.180	9018	Blair *et al* (1982)
BA 668	1.92	-0.268	8030	Blair *et al* (1982)
BA 676	1.94	-0.120	7265	Blair *et al* (1982)
BA 684	2.56	-0.130	7220	Blair *et al* (1982)
BA 487	2.68	-0.452	8615	Blair *et al* (1982)
BA 381	3.06	-0.422	9301	Blair *et al* (1982)
BA 204	1.42	-0.217	8466	Dennefeld and Kunth (1981)
BA 289	0.92	0.107	7719	Dennefeld and Kunth (1981)
BA 359	1.92	-0.288	8741	Dennefeld and Kunth (1981)
BA 429	1.12	0.153	6842	Dennefeld and Kunth (1981)
BA 479	1.82	-0.051	8091	Dennefeld and Kunth (1981)
BA 500	2.60	-0.615	9308	Dennefeld and Kunth (1981)
BA 666	1.90	-0.329	8443	Dennefeld and Kunth (1981)
BA 677	1.98	-0.207	8242	Dennefeld and Kunth (1981)

Table A.10: The columns represent the HII region name, the galactrocentric distance in units of the effective radius, the computed [N/O] relation, the computed NII temperature, and the appropriate reference for observational data.

Table A.11: Data for metal-poor dwarf galaxies

Object	[N/O]	[NII] Temp	Reference
T1304-253	-0.718	10891	Kobulnicky and Skillman (1996)
C1543+091	-0.569	11249	Kobulnicky and Skillman (1996)
Mrk 36	-0.651	11360	Kobulnicky and Skillman (1996)
C1148-203	-0.561	11253	Kobulnicky and Skillman (1996)
Fairall 30	-0.537	11175	Kobulnicky and Skillman (1996)
C0840+120	-0.628	11332	Kobulnicky and Skillman (1996)
UM 462	-0.716	11034	Kobulnicky and Skillman (1996)
T1304-386	-0.396	10957	Kobulnicky and Skillman (1996)
UM 469	-0.277	11526	Kobulnicky and Skillman (1996)
N5253A	-0.043	13024	Kobulnicky and Skillman (1996)
N5253B	-0.598	11133	Kobulnicky and Skillman (1996)
T1345-420	-0.812	11067	Kobulnicky and Skillman (1996)
II Zw 40	-0.257	10753	Kobulnicky and Skillman (1996)
T0645-376	-0.158	11244	Kobulnicky and Skillman (1996)
T1334-396	-0.748	10611	Kobulnicky and Skillman (1996)
T1004-296SE	-0.484	11451	Kobulnicky and Skillman (1996)
T1004-296NW	-0.402	11451	Kobulnicky and Skillman (1996)
T1324-276	-0.536	11067	Kobulnicky and Skillman (1996)
T0633-415	-0.501	10807	Kobulnicky and Skillman (1996)
C1409+120	-0.353	10630	Kobulnicky and Skillman (1996)
Fairall 2	-0.323	11132	Kobulnicky and Skillman (1996)
T1008-286	-0.440	10311	Kobulnicky and Skillman (1996)
T1457-262A	-0.536	11147	Kobulnicky and Skillman (1996)
T1457-262B	-0.712	11026	Kobulnicky and Skillman (1996)
T0440-381	-0.698	11113	Kobulnicky and Skillman (1996)
T1116-325	-0.524	11289	Kobulnicky and Skillman (1996)
1 Zw 18 SE	-0.773	13075	Kobulnicky and Skillman (1996)
1 Zw 18 NW	-0.739	13033	Kobulnicky and Skillman (1996)
N4214 A6	-0.396	11601	Kobulnicky and Skillman (1996)

Table A.11: The columns represent the region name, the computed [N/O] relation, the computed NII temperature, and the appropriate reference for observational data.

Appendix B

NICE Code Listing

B.1 "Element" Class and Function Declarations — nice.hh

```
#ifndef __NICE_HH__
#define __NICE_HH__

#include <stdio.h>
#include <math.h>
#include <fstream.h>
#include <iostream.h>

extern const float  tstop;     // Calculation stop time
extern const float  dt;        // Length of time step
extern const float  mup;       // Upper integrated mass limit
extern const float  mdown;     // Lower integrated mass limit
extern const float  m_cut;     // "Elbow" in IMF
extern const float  dm;        // Size of mass step
extern const float  nu;        // Coefficient for SFR
extern const float  sal_x_low; // Coefficient for low-mass IMF
extern const float  sal_x_hi;  // Coefficient for hi-mass IMF
extern const float  tnow;      // Current galaxy age
extern const float  mass_now;  // Current mass at tnow
extern const float  taudisk;   // Timescale for infall onto disk
```

```
class Element
{

public:
  Element ();
  ~Element ();

  float GetMassFraction() const
  { return its_mass_fraction; }
  float GetMassFractionInfall() const
  { return its_mass_fraction_infall; }
  float GetEjected() const
  { return its_ejected; }
  float GetMass() const
  { return its_mass; }
  float GetLogFraction() const
  { return its_log_fraction; }
  float GetOffset() const
  { return its_offset; }
  void  SetMassFraction(float mf)
  { its_mass_fraction = mf; }
  void  SetMassFractionInfall(float mfi)
  { its_mass_fraction_infall = mfi; }
  void  SetEjected(float ej)
  { its_ejected = ej; }
  void  SetMass(float m)
  { its_mass = m; }
  void  SetLogFraction(float lf)
  { its_log_fraction = lf; }
  void  SetOffset(float of)
  { its_offset = of; }

private:
  float its_mass_fraction;
  float its_mass_fraction_infall;
  float its_ejected;
  float its_mass;
  float its_log_fraction;
  float its_offset;
```

```
};

//  Interpolate between points in input databases
float interpolate(float *, int, int, float);

//  Computes lifetime of a star of mass m
float tau(float);

//  Computes turn-off mass given lifetime t
float turn_off(float);

//  Star formation rate
float psi(float, float);

//  Computes mass of long-lived remnant of star
float remnant(float);

//  Inital Mass Function
float phi(float, float);

//  Computes rate of infall at each time step
float infall(float, float);

//  Directs computation of yield to appropriate function
float yield(int, float, float);

//  Yield of nitrogen
float p14(float, float);

//  Yield of oxygen
float p16(float, float);

//  Yield of helium
float p4(float, float);

//  Yield of sulfur
float p32(float, float);

//  Yield of iron
float p56(float, float);
```

```
//  Rate calculation of supernovae type Ia
float sn1(float, int, float *, float *, float);

//  Rate calculation of supernovae type II
float sn2(float, int, float *, float *, float, float);

//  Calculates loop index for birth of a star of mass m
int   birth(int, float );

//  Calculates the number of low-mass stars formed this loop
float gdwarf(float, int, float *, float *, float);

#endif
```

B.2 Main NICE code — nice.cc

```
#include "nice.hh"


//  In pointer array, elements are stored in order of increasing Z
//
//  Elements are :   [0]    [1]    [2]    [3]    [4]    [5]
//                   1      4      14     16     32     56
//                   H      He     N      O      S      Fe
//
//
//  atomic_number[] array holds the Z of computed elements.  Used
//  to call the correct routine for yields


const int   atomic_number[] = {1, 4, 14, 16, 32, 56};
const float offset[]        = {0.0, 0.60, 1.15, 1.20, 1.50, 1.75};
const float infallfrac[]    = {0.76, 0.24, 0.0, 0.0, 0.0, 0.0};
const float SN1a_w7[]       = {0.0, 0.0, 0.0, 0.143, 0.084, 0.717};
const int   num_elements    = sizeof(atomic_number)/
                              sizeof(atomic_number[0]);

int main()
{
  const int steps = int((tstop / dt) + 1);

  float     total_mass[steps];
  float     gas_mass[steps];
  float     star_mass[steps];


//  The array Z[][] is a 2-D array of pointers to the element
//  objects at each time step for each element.  pointer[] is
//  just an array of pointers to instantiate elements of Z[][]
//  as they are computed


  Element * Z[num_elements][steps];
  Element * pointer[num_elements];
```

```
  float time        = 0.05;  //  Beginning time
  int   n           = 0;     //  Loop counter
  float c           = 0.05;  //  Correction factor for SN1a
  float cc;
  float log_feh     = -10.0; //  Tracks log[Fe/H]
  float metallicity = -10.0; // Tracks log(mass of heavy elements)
  float g_dwarfs    = 0;    // Counts dwarf stars formed this loop
  float g_dwarf_tot = 0;   // Total # of dwarf stars formed
  int   processed_flag;      // Flags what mass range we are in
  total_mass[0]     = 0.1;   //  Total mass indexed by loop
  gas_mass[0]       = 0.1;   //  Gas mass indexed by loop


//  Compute normalization coefficients for IMF and infall


  float a_sal = 1 / (
    ((pow(m_cut, (1 - sal_x_low))
      - pow(mdown, (1 - sal_x_low)))
    / (1 - sal_x_low)) +
    ((pow(mup, (1 - sal_x_hi))
      - pow(m_cut, (1 - sal_x_hi)))
    / (1 - sal_x_hi)));

  float a_inf = mass_now / (taudisk * (1 - exp(-tnow / taudisk)));


//  Main loop over time


  while (time < tstop)
  {


//  Loop over elements


    for (int z = 0; z < num_elements; z++)
    {
      pointer[z] = new Element;
```

```
//  In first loop, initialize all elements using
//  default constructor


      if (n == 0)
      {
        Z[z][0] = pointer[z];
      }
    }

    if (n == 0)
    {
      pointer[0]->SetMass(0.074);
      pointer[1]->SetMass(0.026);
    }


//  Initalize total mass ejected and mass of metals


    float mass_eject          = 0.0;
    float z_mass              = 0.0;

    for (int z = 1; z < num_elements; z++)
    {


//  Now compute the cut-off mass of stars that have
//  evolved during this time step


      float mass              = turn_off(time);
      float element_eject     = 0.0;
      float d_element         = 0.0;


//  For each element, set the mass conversion constant and the
//  mass fraction of this element in the infall
```

```
      pointer[z]->SetOffset(offset[z]);
      pointer[z]->SetMassFractionInfall(infallfrac[z]);


//  Integrate over all evolved stars for their contribution back to
//  the ISM


      while (n > 0 && mass < mup)
      {
        float p = yield(atomic_number[z], mass, metallicity);
        int ago = birth(n, mass);


//  ago finds loop in which this star was born


        if (z == 1)  //  Only have to get ejected mass once
        {
          mass_eject += (mass - remnant(mass))
            * psi(gas_mass[ago], total_mass[ago])
            * phi(mass, a_sal) * dm;
        }

        if (mass >= 3.0 && mass <= 16.0)
          cc = 1.0 - c;
        else
          cc = 1.0;

        if (mass > 12.0)
          processed_flag = 0;
        else
          processed_flag = 1;

        if (ago == n)
        {
          element_eject += (((mass - remnant(mass) - mass * p)
            * Z[z][n-1]->GetMassFraction()) * processed_flag
                           + mass * p)
            * psi(gas_mass[ago], total_mass[ago])
```

```
            * phi(mass, a_sal) * dm * cc;
        }
        else
        {
          element_eject += (((mass - remnant(mass) - mass * p)
            * Z[z][ago]->GetMassFraction()) * processed_flag
                             + mass * p)
            * psi(gas_mass[ago], total_mass[ago])
            * phi(mass, a_sal) * dm * cc;
        }
        mass += dm;
      }


//  Finished integrating over mass, so record the amount of this
//  element ejected


      pointer[z]->SetEjected(element_eject);


//  d_element is the change in element[z] from:
//  Infall - SFR + Ejected


      if (n > 0)
      {
        d_element = ((pointer[z]->GetMassFractionInfall()
                      * infall(time, a_inf))
                    - (Z[z][n-1]->GetMassFraction()
                       * psi(gas_mass[n], total_mass[n]))
                    + pointer[z]->GetEjected()
                    + (sn1(time, n, gas_mass, total_mass, a_sal)
                       * SN1a_w7[z] * c) ) * dt;

        pointer[z]->SetMass(Z[z][n-1]->GetMass() + d_element);
      }
      else
      {
        d_element = ((pointer[z]->GetMassFractionInfall()
                      * infall(time, a_inf))
```

```
                    - (Z[z][0]->GetMassFraction()
                       * psi(gas_mass[n], total_mass[n]))
                    + pointer[z]->GetEjected()
                    + (sn1(time, n, gas_mass, total_mass, a_sal)
                       * SN1a_w7[z] * c) ) * dt;
      }
    }


//  Finished loop over elements, now find the change to the
//  total gas mass


    float d_gas_mass = (-psi(gas_mass[n], total_mass[n])
                         + infall(time, a_inf) + mass_eject) * dt;

    gas_mass[n+1] = gas_mass[n] + d_gas_mass;
    total_mass[n+1] = total_mass[n] + infall(time, a_inf) * dt;
    star_mass[n+1] = total_mass[n+1] - gas_mass[n+1];


//  Check for catastrophe


    if (gas_mass[n+1] < 0.0)
      cout << "Gas mass less than zero...\n";


//  Compute mass of metals, then subtract (He_mass + z_mass)
//  from gas_mass to get H_mass


    for (int z = 2; z < num_elements; z++)
      z_mass += pointer[z]->GetMass();

    pointer[0]->SetMass
      (gas_mass[n] - pointer[1]->GetMass() - z_mass);

    pointer[0]->SetMassFraction
      (pointer[0]->GetMass()/gas_mass[n]);
```

```
    pointer[0]->SetLogFraction
      (log10(pointer[0]->GetMassFraction()));

    Z[0][n] = pointer[0];

    metallicity = log10(z_mass/gas_mass[n]) -
                  pointer[0]->GetLogFraction();

    g_dwarfs = gdwarf(time, n, gas_mass, total_mass, a_sal);
    g_dwarf_tot += g_dwarfs;

    printf("%5.2f %5.2f %5.2f %5.2f %5.2f
            %5.2f %6.2f %6.4f %6.4f ",
           time,
           psi(gas_mass[n], total_mass[n]),
           infall(time, a_inf),
           gas_mass[n],
           total_mass[n],
           g_dwarfs,
           g_dwarf_tot,
           sn1(time, n, gas_mass, total_mass, a_sal) * c,
           sn2(time, n, gas_mass, total_mass, c, a_sal));


//  Compute the mass fractions of the elements, and output


    for (int z = 1; z < num_elements; z++)
    {
      pointer[z]->SetMassFraction
        (pointer[z]->GetMass()/gas_mass[n]);

      pointer[z]->SetLogFraction
        (log10(pointer[z]->GetMassFraction())
         - pointer[0]->GetLogFraction()
         - pointer[z]->GetOffset() + 12.0);

      printf("%5.2f ", pointer[z]->GetLogFraction());

      Z[z][n] = pointer[z];
    }
```

```
    log_feh = Z[5][n]->GetLogFraction()
      + Z[5][n]->GetOffset() -12.0 + 2.78;


//  Print log(Fe/H)+12 and [N/O]


    printf("%5.2f ", log_feh);
    printf("%5.3f", Z[2][n]->GetLogFraction()
           - Z[3][n]->GetLogFraction() + 0.90);

    cout << endl;

    n++;
    time += dt;
  }    // finish time step loop
}
```

B.3 Element Member Functions — nice_functions.cc

```
#include "nice_yields.hh"
#include "nice.hh"


const float tstop     = 15.0;
const float dt        = 0.01;
const float mup       = 40.0;
const float mdown     = 0.08;
const float dm        = 0.1;
const float nu        = 1.8;
const float sal_x_low = 1.3;
const float sal_x_hi  = 1.3;
const float m_cut     = 10.0;
const float tnow      = 13.0;
const float mass_now  = 50.0;
const float taudisk   = 6.0;


Element::Element():
  its_mass_fraction        (0.0),
  its_mass_fraction_infall (0.0),
  its_mass                 (0.0),
  its_ejected              (0.0),
  its_log_fraction         (0.0),
  its_offset               (0.0)
{
};

Element::~Element()
{
};


float interpolate(float * matrix, int row, int col, float var)
{
  for (int i = 0; i < row; i++)
```

```
  {
    if (matrix[(i * col)] <= var && matrix[(i + 1) * col] >= var)
    {
      float vlow = matrix[(i * col)];
      float vhigh = matrix[(i + 1) * col];
      float dv = vhigh - vlow;
      float flow = matrix[(i * col) + 1];
      float fhigh = matrix[(i + 1) * col + 1];
      float dfv = fhigh - flow;
      float slope = dfv / dv;
      return slope * (var - vlow) + flow;
    }
  }
}


float tau(float m)
{
  if (m <= 120.0 && m >= 0.8)
  {
    return interpolate(&Tau[0][0], 20, 2, m);
  }
  else
    return 10.0/(pow(m, 2.5));
}


float turn_off(float t)
{
  if (t <= 25.03 && t >= 0.002)
  {
    return interpolate(&Turn_off[0][0], 20, 2, t);
  }
  else
    return pow((10.0/t), 0.4);
}



float psi(float mg, float tm)
{
```

```
  if (tm == 0.0)
    return 0.0;
  else if (mg < 7.0)
    return 0.0;
  else
    return (nu * pow(mg, 2.2) / tm);
}


float remnant(float m)
{
  if (m > 12.0)
    return (m - (interpolate(&remn[0][0], 10, 2, m)));
  else
    return 0.368 + (0.1 * m) - (0.0026 * pow(m, 2.0))
      + (3.26E-5 * pow(m, 3.0));
}


float phi(float m, float a)
{
  if (m <= 10.0)
    return a * pow(m, (-(1 + sal_x_low)));
  else
    return a * pow(m, (-(1 + sal_x_hi)));
}


float infall(float t, float a)
{
  return a * exp(-t / taudisk);
}


int birth(int n, float m)
{
  int history = (n - int(tau(m) / dt));
  if (history >= 1)
    return history;
  else
    return 1;
```

```
}


float yield(int x, float m, float z)
{
  switch (x)
  {
  case 4:  return p4(m, z);
    break;
  case 14: return p14(m, z);
    break;
  case 16: return p16(m, z);
    break;
  case 32: return p32(m, z);
    break;
  case 56: return p56(m, z);
    break;
  default: cout << "invalid element\n";
  }
}


float p56(float m, float z)
{
  if (m > 12.0 && m < 40.0)
  {
    if (z <= -1.5)
      return interpolate(&Fe56ww_0_0_1[0][0], 10, 2, m) / m ;
    if ((z > -1.5) && (z <= -0.5))
      return interpolate(&Fe56ww_0_1[0][0], 10, 2, m) / m ;
    if (z > -0.5)
      return interpolate(&Fe56ww_1[0][0], 10, 2, m) / m ;
  }
  else
    return 0.0;
}


float p32(float m, float z)
{
  if (m > 12.0 && m < 40.0)
```

```
  {
    if (z <= -1.5)
      return interpolate(&S32ww_0_0_1[0][0], 10, 2, m) / m ;
    if ((z > -1.5) && (z <= -0.5))
      return interpolate(&S32ww_0_1[0][0], 10, 2, m) / m ;
    if (z > -0.5)
      return interpolate(&S32ww_1[0][0], 10, 2, m) / m ;
  }
  else
    return 0.0;
}


float p14(float m, float z)
{
  if (m > 1.0 && m < 8.0)
  {
    if (z <= -1.25)
      return interpolate(&N14b_15[0][0], 13, 2, m) / m;
    if ((z > -1.25) && (z <= -0.75))
      return interpolate(&N14b_10[0][0], 18, 2, m) / m;
    if ((z > -0.75) && (z <= -0.35))
      return interpolate(&N14b_05[0][0], 14, 2, m) / m;
    if ((z > -0.35) && (z <= -0.15))
      return interpolate(&N14b_02[0][0], 18, 2, m) / m;
    if ((z > -0.15) && (z <= -0.05))
      return interpolate(&N14b_01[0][0], 24, 2, m) / m;
    if ((z > -0.05) && (z <= 0.05))
      return interpolate(&N14b_00[0][0], 24, 2, m) / m;
    if ((z > 0.05) && (z <= 0.15))
      return interpolate(&N14b_p1[0][0], 13, 2, m) / m;
    if (z > 0.15)
      return interpolate(&N14b_p2[0][0], 13, 2, m) / m;
  }
  else if (m > 12.0 && m < 40.0)
  {
    if (z <= -1.5)
      return interpolate(&N14ww_0_0_1[0][0], 10, 2, m) / m ;
    if ((z > -1.5) && (z <= -0.5))
      return interpolate(&N14ww_0_1[0][0], 10, 2, m) / m ;
    if (z > -0.5)
```

```
      return interpolate(&N14ww_1[0][0], 10, 2, m) / m ;
  }
  else
    return 0.0;
}


float p16(float m, float z)
{
  if (m > 1.0 && m < 8.0)
  {
    if (z <= -1.25)
      return interpolate(&016b_15[0][0], 13, 2, m) / m;
    if ((z > -1.25) && (z <= -0.75))
      return interpolate(&016b_10[0][0], 18, 2, m) / m;
    if ((z > -0.75) && (z <= -0.35))
      return interpolate(&016b_05[0][0], 14, 2, m) / m;
    if ((z > -0.35) && (z <= -0.15))
      return interpolate(&016b_02[0][0], 18, 2, m) / m;
    if ((z > -0.15) && (z <= -0.05))
      return interpolate(&016b_01[0][0], 24, 2, m) / m;
    if ((z > -0.05) && (z <= 0.05))
      return interpolate(&016b_00[0][0], 24, 2, m) / m;
    if ((z > 0.05) && (z <= 0.15))
      return interpolate(&016b_p1[0][0], 13, 2, m) / m;
    if (z > 0.15)
      return interpolate(&016b_p2[0][0], 13, 2, m) / m;
  }
  if (m > 12.0 && m < 40.0)
  {
    if (z <= -1.5)
      return interpolate(&016ww_0_0_1[0][0], 10, 2, m) / m ;
    if ((z > -1.5) && (z <= -0.5))
      return interpolate(&016ww_0_1[0][0], 10, 2, m) / m ;
    if (z > -0.5)
      return interpolate(&016ww_1[0][0], 10, 2, m) / m ;
  }
  else
    return 0.0;
}
```

```
float p4(float m, float z)
{
  if (m > 1.0 && m < 8.0)
  {
    if (z <= -1.25)
      return interpolate(&He4b_15[0][0], 13, 2, m) / m;
    if ((z > -1.25) && (z <= -0.75))
      return interpolate(&He4b_10[0][0], 18, 2, m) / m;
    if ((z > -0.75) && (z <= -0.35))
      return interpolate(&He4b_05[0][0], 14, 2, m) / m;
    if ((z > -0.35) && (z <= -0.15))
      return interpolate(&He4b_02[0][0], 18, 2, m) / m;
    if ((z > -0.15) && (z <= -0.05))
      return interpolate(&He4b_01[0][0], 24, 2, m) / m;
    if ((z > -0.05) && (z <= 0.05))
      return interpolate(&He4b_00[0][0], 24, 2, m) / m;
    if ((z > 0.05) && (z <= 0.15))
      return interpolate(&He4b_p1[0][0], 13, 2, m) / m;
    if (z > 0.15)
      return interpolate(&He4b_p2[0][0], 13, 2, m) / m;
  }
  else if (m > 12.0 && m < 40.0)
  {
    if (z <= -1.5)
      return interpolate(&He4ww_0_0_1[0][0], 10, 2, m) / m ;
    if ((z > -1.5) && (z <= -0.5))
      return interpolate(&He4ww_0_1[0][0], 10, 2, m) / m ;
    if (z > -0.5)
      return interpolate(&He4ww_1[0][0], 10, 2, m) / m ;
  }
  else
    return 0.0;
}


float sn1(float t, int n, float * mg, float * tm, float a)
{
  if (turn_off(t) > 8.0)
    return 0.0;
  else
```

```
  {
    float d_mu = 0.01;
    float psi_prime = 0.0;
    float sn1 = 0.0;
    float binary_mass = 2.0 * turn_off(t);
    if (binary_mass < 3.0)
      binary_mass = 3.0;
    while (binary_mass < 16.0)
    {
      psi_prime = 0.0;
      float mu_prime = turn_off(t);
      if (mu_prime < (binary_mass - 8.0))
        mu_prime = (binary_mass - 8.0);
      float mu = mu_prime / binary_mass;
      while (mu <= 0.5)
      {
        float secondary_mass = mu * binary_mass;
        int ago = birth(n, secondary_mass);
        psi_prime += (24.0*mu*mu) * psi(mg[ago], tm[ago]) * d_mu;
        mu += d_mu;
      }
      sn1 += psi_prime * phi(binary_mass, a) * dm;
      binary_mass += dm;
    }
    return sn1;
  }
}

float sn2(float t, int n, float * mg, float * tm, float c, float a)
{
  float min_mass = 8.0;
  float evolved_mass = turn_off(t);
  float rate = 0.0;
  float m, cc;
  if (evolved_mass < min_mass)
    evolved_mass = min_mass;
  m = evolved_mass;
  while (m < 40.0)
  {
    if (m > 8.0 && m < 16.0)
      cc = 1-c;
```

```
    else
      cc = 1;
    int ago = birth(n, m);
    rate += psi(mg[ago], tm[ago]) * phi(m, a) * dm * cc;
    m += dm;
  }
  return rate;
}

float gdwarf(float t, int n, float * mg, float * tm, float a)
{
  float m_hi = 0.9;
  float m = mdown;
  float num = 0.0;
  while (m < m_hi)
  {
    num += psi(mg[n], tm[n]) * phi(m, a) * dm * dt;
    m += dm;
  }
  return num;
}
```

B.4 Yield Data — nice_yields.hh

```
#ifndef __YIELDS_HH__
#define __YIELDS_HH__


float He4b_15[13][2]       = {{1.0, 1.24E-02}, {1.2, 1.86E-02},
                               {1.4, 2.75E-02}, {1.7, 4.28E-02},
                               {2.0, 6.01E-02}, {2.5, 7.60E-02},
                               {3.0, 7.79E-02}, {3.5, 2.36E-02},
                               {4.0, 7.87E-02}, {4.5, 1.53E-01},
                               {5.0, 2.27E-01}, {6.0, 3.81E-01},
                               {8.0, 7.09E-01}};

float N14b_15[13][2]       = {{1.0, 2.00E-05}, {1.2, 3.19E-05},
                               {1.4, 4.35E-05}, {1.7, 6.07E-05},
                               {2.0, 7.80E-05}, {2.5, 1.09E-04},
                               {3.0, 1.49E-04}, {3.5, 1.07E-02},
                               {4.0, 1.42E-02}, {4.5, 1.71E-02},
                               {5.0, 2.11E-02}, {6.0, 3.37E-02},
                               {8.0, 7.32E-02}};

float O16b_15[13][2]       = {{1.0, -2.34E-06}, {1.2, -2.53E-06},
                               {1.4, 8.50E-07}, {1.7, 1.10E-05},
                               {2.0, 2.88E-05}, {2.5, 7.85E-05},
                               {3.0, 1.33E-04}, {3.5, -1.06E-03},
                               {4.0, -1.59E-03}, {4.5, -2.03E-03},
                               {5.0, -2.33E-03}, {6.0, -2.74E-03},
                               {8.0, -3.26E-03}};

float He4b_10[13][2]       = {{1.0, 1.25E-02}, {1.2, 1.65E-02},
                               {1.4, 2.38E-02}, {1.6, 3.22E-02},
                               {1.8, 4.33E-02}, {2.0, 5.41E-02},
                               {2.2, 6.16E-02}, {2.4, 8.12E-02},
                               {3.0, 7.53E-02}, {3.5, 3.31E-02},
                               {3.6, 2.61E-02}, {3.7, 1.98E-02},
                               {3.8, 3.39E-02}};

float N14b_10[13][2]       = {{1.0, 6.76E-05}, {1.2, 1.03E-04},
                               {1.4, 1.40E-04}, {1.6, 1.78E-04},
```

```
                          {1.8, 2.14E-04}, {2.0, 2.51E-04},
                          {2.2, 2.91E-04}, {2.4, 3.22E-04},
                          {3.0, 4.78E-04}, {3.5, 1.54E-02},
                          {3.6, 1.38E-02}, {3.7, 1.23E-02},
                          {3.8, 1.29E-02}};

float O16b_10[13][2]    = {{1.0, -9.14E-06}, {1.2, -1.42E-05},
                          {1.4, -3.06E-05}, {1.6, -5.26E-05},
                          {1.8, -8.38E-05}, {2.0, -1.16E-04},
                          {2.2, -1.38E-04}, {2.4, -1.77E-04},
                          {3.0, -1.34E-04}, {3.5, -5.94E-04},
                          {3.6, -1.59E-03}, {3.7, -2.57E-03},
                          {3.8, -2.99E-03}};

float He4b_05[14][2]    = {{1.0, 1.27E-02}, {1.2, 1.64E-02},
                          {1.4, 1.86E-02}, {1.6, 2.73E-02},
                          {1.8, 3.89E-02}, {2.0, 5.40E-02},
                          {2.2, 6.51E-02}, {2.4, 7.29E-02},
                          {2.5, 7.53E-02}, {3.5, 3.32E-02},
                          {4.5, 1.19E-01}, {5.0, 1.97E-01},
                          {6.0, 3.52E-01}, {8.0, 6.53E-01}};

float N14b_05[14][2]    = {{1.0, 1.59E-04}, {1.2, 2.41E-04},
                          {1.4, 3.23E-04}, {1.6, 4.03E-04},
                          {1.8, 4.82E-04}, {2.0, 5.54E-04},
                          {2.2, 6.36E-04}, {2.4, 7.32E-04},
                          {2.5, 7.83E-04}, {3.5, 1.14E-02},
                          {4.5, 1.71E-02}, {5.0, 2.25E-02},
                          {6.0, 3.58E-02}, {8.0, 6.21E-02}};

float O16b_05[14][2]    = {{1.0, -1.93E-05}, {1.2, -2.82E-05},
                          {1.4, -3.94E-05}, {1.6, -1.06E-04},
                          {1.8, -2.03E-04}, {2.0, -3.32E-04},
                          {2.2, -4.27E-04}, {2.4, -4.89E-04},
                          {2.5, -5.10E-04}, {3.5, -3.17E-04},
                          {4.5, -6.07E-03}, {5.0, -8.57E-03},
                          {6.0, -1.26E-02}, {8.0, -1.94E-02}};

float He4b_02[18][2]    = {{1.0, 1.32E-02}, {1.1, 1.49E-02},
                          {1.2, 1.63E-02}, {1.3, 1.74E-02},
                          {1.4, 1.80E-02}, {1.5, 1.83E-02},
```

```
                        {1.6, 2.09E-02}, {1.7, 2.49E-02},
                        {1.8, 2.96E-02}, {1.9, 3.68E-02},
                        {2.0, 4.30E-02}, {2.5, 7.16E-02},
                        {3.5, 4.95E-02}, {4.0, 9.07E-03},
                        {4.5, 9.29E-02}, {5.0, 1.73E-01},
                        {6.0, 3.29E-01}, {8.0, 6.18E-01}};

float N14b_02[18][2]   = {{1.0, 2.48E-04}, {1.1, 3.04E-04},
                        {1.2, 3.64E-04}, {1.3, 4.24E-04},
                        {1.4, 4.85E-04}, {1.5, 5.48E-04},
                        {1.6, 6.11E-04}, {1.7, 6.72E-04},
                        {1.8, 7.31E-04}, {1.9, 7.86E-04},
                        {2.0, 8.42E-04}, {2.5, 1.16E-03},
                        {3.5, 1.96E-03}, {4.0, 1.08E-02},
                        {4.5, 1.59E-02}, {5.0, 2.15E-02},
                        {6.0, 3.45E-02}, {8.0, 5.17E-02}};

float O16b_02[18][2]   = {{1.0, -2.58E-05}, {1.1, -3.11E-05},
                        {1.2, -3.65E-05}, {1.3, -4.18E-05},
                        {1.4, -4.70E-05}, {1.5, -5.21E-05},
                        {1.6, -8.18E-05}, {1.7, -1.30E-04},
                        {1.8, -1.87E-04}, {1.9, -2.72E-04},
                        {2.0, -3.51E-04}, {2.5, -6.71E-04},
                        {3.5, -5.25E-04}, {4.0, -1.96E-03},
                        {4.5, -4.65E-03}, {5.0, -7.56E-03},
                        {6.0, -1.26E-02}, {8.0, -1.95E-02}};

float He4b_01[24][2]   = {{1.0, 1.30E-02}, {1.1, 1.47E-02},
                        {1.2, 1.60E-02}, {1.3, 1.71E-02},
                        {1.4, 1.77E-02}, {1.5, 1.79E-02},
                        {1.6, 1.88E-02}, {1.7, 2.18E-02},
                        {1.8, 2.59E-02}, {1.9, 3.15E-02},
                        {2.1, 4.65E-02}, {2.2, 5.41E-02},
                        {2.3, 5.89E-02}, {2.4, 6.45E-02},
                        {2.5, 6.44E-02}, {2.6, 6.85E-02},
                        {3.3, 7.70E-02}, {3.5, 5.85E-02},
                        {3.9, 2.31E-02}, {4.1, 1.08E-02},
                        {4.5, 6.58E-02}, {5.0, 1.47E-01},
                        {7.0, 4.50E-01}, {8.0, 5.86E-01}};

float N14b_01[24][2]   = {{1.0, 3.16E-04}, {1.1, 3.88E-04},
```

```
                          {1.2, 4.63E-04}, {1.3, 5.40E-04},
                          {1.4, 6.17E-04}, {1.5, 6.96E-04},
                          {1.6, 7.80E-04}, {1.7, 8.57E-04},
                          {1.8, 9.33E-04}, {1.9, 1.01E-03},
                          {2.1, 1.14E-03}, {2.2, 1.21E-03},
                          {2.3, 1.29E-03}, {2.4, 1.38E-03},
                          {2.5, 1.48E-03}, {2.6, 1.57E-03},
                          {3.3, 2.24E-03}, {3.5, 2.47E-03},
                          {3.9, 1.76E-02}, {4.1, 1.38E-02},
                          {4.5, 1.62E-02}, {5.0, 2.17E-02},
                          {7.0, 4.34E-02}, {8.0, 4.61E-02}};

float O16b_01[24][2]    = {{1.0, -3.30E-05}, {1.1, -3.97E-05},
                          {1.2, -4.65E-05}, {1.3, -5.32E-05},
                          {1.4, -5.97E-05}, {1.5, -6.62E-05},
                          {1.6, -8.36E-05}, {1.7, -1.35E-04},
                          {1.8, -2.05E-04}, {1.9, -2.99E-04},
                          {2.1, -5.35E-04}, {2.2, -6.52E-04},
                          {2.3, -7.24E-04}, {2.4, -8.06E-04},
                          {2.5, -8.17E-04}, {2.6, -8.83E-04},
                          {3.3, -1.11E-03}, {3.5, -8.67E-04},
                          {3.9, -8.22E-04}, {4.1, -1.78E-03},
                          {4.5, -3.90E-03}, {5.0, -6.96E-03},
                          {7.0, -1.72E-02}, {8.0, -1.95E-02}};

float He4b_00[24][2]    = {{1.0, 1.28E-02}, {1.1, 1.44E-02},
                          {1.2, 1.57E-02}, {1.3, 1.66E-02},
                          {1.4, 1.72E-02}, {1.5, 1.74E-02},
                          {1.6, 1.74E-02}, {1.7, 1.85E-02},
                          {1.8, 2.16E-02}, {1.9, 2.61E-02},
                          {2.1, 4.12E-02}, {2.2, 4.97E-02},
                          {2.3, 5.17E-02}, {2.4, 5.75E-02},
                          {2.5, 6.09E-02}, {2.6, 6.45E-02},
                          {3.3, 7.53E-02}, {3.5, 8.06E-02},
                          {3.9, 5.56E-02}, {4.1, 3.34E-02},
                          {4.5, 2.45E-02}, {5.0, 1.07E-01},
                          {7.0, 4.07E-01}, {8.0, 5.41E-01}};

float N14b_00[24][2]    = {{1.0, 4.04E-04}, {1.1, 4.96E-04},
                          {1.2, 5.90E-04}, {1.3, 6.87E-04},
                          {1.4, 7.85E-04}, {1.5, 8.85E-04},
```

```
                             {1.6, 9.92E-04}, {1.7, 1.09E-03},
                             {1.8, 1.19E-03}, {1.9, 1.29E-03},
                             {2.1, 1.46E-03}, {2.2, 1.54E-03},
                             {2.3, 1.66E-03}, {2.4, 1.77E-03},
                             {2.5, 1.88E-03}, {2.6, 2.00E-03},
                             {3.3, 2.83E-03}, {3.5, 3.04E-03},
                             {3.9, 3.56E-03}, {4.1, 1.86E-02},
                             {4.5, 1.76E-02}, {5.0, 2.31E-02},
                             {7.0, 4.16E-02}, {8.0, 4.21E-02}};

float O16b_00[24][2]       = {{1.0, -4.21E-05}, {1.1, -5.07E-05},
                             {1.2, -5.92E-05}, {1.3, -6.78E-05},
                             {1.4, -7.60E-05}, {1.5, -8.42E-05},
                             {1.6, -9.28E-05}, {1.7, -1.28E-04},
                             {1.8, -2.03E-04}, {1.9, -3.10E-04},
                             {2.1, -6.29E-04}, {2.2, -7.98E-04},
                             {2.3, -8.46E-04}, {2.4, -9.64E-04},
                             {2.5, -1.04E-03}, {2.6, -1.12E-03},
                             {3.3, -1.48E-03}, {3.5, -1.59E-03},
                             {3.9, -1.16E-03}, {4.1, -9.15E-04},
                             {4.5, -2.64E-03}, {5.0, -5.83E-03},
                             {7.0, -1.68E-02}, {8.0, -1.85E-02}};

float He4b_p1[13][2]       = {{1.0, 1.24E-02}, {1.2, 1.52E-02},
                             {1.4, 1.67E-02}, {1.7, 1.63E-02},
                             {2.0, 2.10E-02}, {2.6, 5.83E-02},
                             {3.0, 6.56E-02}, {3.6, 7.94E-02},
                             {4.0, 9.18E-02}, {4.5, 5.62E-02},
                             {5.0, 4.57E-02}, {6.0, 2.02E-01},
                             {8.0, 4.75E-01}};

float N14b_p1[13][2]       = {{1.0, 5.15E-04}, {1.2, 7.57E-04},
                             {1.4, 1.01E-03}, {1.7, 1.40E-03},
                             {2.0, 1.80E-03}, {2.6, 2.55E-03},
                             {3.0, 3.21E-03}, {3.6, 3.97E-03},
                             {4.0, 4.47E-03}, {4.5, 2.18E-02},
                             {5.0, 2.77E-02}, {6.0, 3.87E-02},
                             {8.0, 4.22E-02}};

float O16b_p1[13][2]       = {{1.0, -5.37E-05}, {1.2, -7.60E-05},
                             {1.4, -9.75E-05}, {1.7, -1.29E-04},
```

```
                                {2.0, -3.48E-04}, {2.6, -1.37E-03},
                                {3.0, -1.67E-03}, {3.6, -2.14E-03},
                                {4.0, -2.45E-03}, {4.5, -1.69E-03},
                                {5.0, -4.79E-03}, {6.0, -1.19E-02},
                                {8.0, -1.69E-02}};

float He4b_p2[13][2]         = {{1.0, 1.19E-02}, {1.2, 1.45E-02},
                                {1.4, 1.58E-02}, {1.8, 1.44E-02},
                                {2.0, 1.65E-02}, {2.4, 4.51E-02},
                                {3.0, 6.25E-02}, {3.4, 6.87E-02},
                                {4.0, 9.74E-02}, {4.5, 1.39E-01},
                                {5.0, 1.25E-01}, {6.0, 1.10E-01},
                                {8.0, 3.70E-01}};

float N14b_p2[13][2]         = {{1.0, 6.60E-04}, {1.2, 9.67E-04},
                                {1.4, 1.28E-03}, {1.8, 1.96E-03},
                                {2.0, 2.30E-03}, {2.4, 2.88E-03},
                                {3.0, 4.04E-03}, {3.4, 4.70E-03},
                                {4.0, 5.55E-03}, {4.5, 6.86E-03},
                                {5.0, 3.05E-02}, {6.0, 5.16E-02},
                                {8.0, 4.78E-02}};

float O16b_p2[13][2]         = {{1.0, -6.88E-05}, {1.2, -9.71E-05},
                                {1.4, -1.24E-04}, {1.8, -1.77E-04},
                                {2.0, -3.50E-04}, {2.4, -1.37E-03},
                                {3.0, -2.17E-03}, {3.4, -2.52E-03},
                                {4.0, -3.48E-03}, {4.5, -4.79E-03},
                                {5.0, -4.35E-03}, {6.0, -1.20E-02},
                                {8.0, -1.61E-02}};

float He4v_z_3[11][2]         = {{1.0, 0.148E-1}, {1.3, 0.213E-1},
                                 {1.5, 0.210E-1}, {1.7, 0.197E-1},
                                 {2.0, 0.242E-1}, {2.5, 0.188E-1},
                                 {3.0, 0.149E-1}, {4.0, 0.202E-1},
                                 {5.0, 0.234E-1}, {7.0, 0.316E-1},
                                 {8.0, 0.295E-1}};

float N14v_z_3[11][2]         = {{1.0, 0.304E-4}, {1.3, 0.364E-4},
                                 {1.5, 0.424E-4}, {1.7, 0.459E-4},
                                 {2.0, 0.811E-4}, {2.5, 0.882E-4},
                                 {3.0, 0.802E-4}, {4.0, 0.472E-2},
```

```
                              {5.0, 0.657E-2}, {7.0, 0.869E-2},
                              {8.0, 0.794E-2}};

float O16v_z_3[11][2]       = {{1.0, -0.223E-5}, {1.3, .249E-3},
                              {1.5, 0.284E-3}, {1.7, 0.304E-3},
                              {2.0, 0.400E-3}, {2.5, 0.429E-3},
                              {3.0, 0.417E-3}, {4.0, 0.431E-3},
                              {5.0, 0.412E-3}, {7.0, 0.629E-4},
                              {8.0, 0.960E-4}};

float He4v_z_2_4[11][2]     = {{1.0, 0.152E-1}, {1.3, 0.184E-1},
                              {1.5, 0.189E-1}, {1.7, 0.203E-1},
                              {2.0, 0.269E-1}, {2.5, 0.309E-1},
                              {3.0, 0.318E-1}, {4.0, 0.199E-1},
                              {5.0, 0.247E-1}, {7.0, 0.282E-1},
                              {8.0, 0.326E-1}};

float N14v_z_2_4[11][2]     = {{1.0, 0.124E-3}, {1.3, 0.160E-3},
                              {1.5, 0.198E-3}, {1.7, 0.215E-3},
                              {2.0, 0.337E-3}, {2.5, 0.418E-3},
                              {3.0, 0.444E-3}, {4.0, 0.447E-2},
                              {5.0, 0.639E-2}, {7.0, 0.858E-2},
                              {8.0, 0.939E-2}};

float O16v_z_2_4[11][2]     = {{1.0, 0.636E-4}, {1.3, 0.144E-3},
                              {1.5, 0.207E-3}, {1.7, 0.309E-3},
                              {2.0, 0.361E-3}, {2.5, 0.396E-3},
                              {3.0, 0.512E-3}, {4.0, 0.276E-3},
                              {5.0, 0.257E-3}, {7.0, -0.254E-3},
                              {8.0, -0.321E-3}};

float He4v_z_2_09[12][2]    = {{1.0, 0.134E-1}, {1.3, 0.174E-1},
                              {1.4, 0.174E-1}, {1.5, 0.191E-1},
                              {1.7, 0.186E-1}, {2.0, 0.249E-1},
                              {2.5, 0.325E-1}, {3.0, 0.342E-1},
                              {4.0, 0.262E-1}, {5.0, 0.265E-1},
                              {7.0, 0.311E-1}, {8.0, 0.406E-1}};

float N14v_z_2_09[12][2]    = {{1.0, 0.241E-3}, {1.3, 0.306E-3},
                              {1.4, 0.308E-3}, {1.5, 0.356E-3},
                              {1.7, 0.394E-3}, {2.0, 0.576E-3},
```

```
                                   {2.5, 0.733E-3}, {3.0, 0.784E-3},
                                   {4.0, 0.443E-2}, {5.0, 0.643E-2},
                                   {7.0, 0.881E-2}, {8.0, 0.111E-1}};

float O16v_z_2_09[12][2]  = {{1.0, 0.536E-4}, {1.3, 0.139E-3},
                                   {1.4, 0.148E-3}, {1.5, 0.216E-3},
                                   {1.7, 0.249E-3}, {2.0, 0.254E-3},
                                   {2.5, 0.235E-3}, {3.0, 0.305E-3},
                                   {4.0, 0.572E-4}, {5.0, 0.660E-4},
                                   {7.0, -.632E-3}, {8.0, -.992E-3}};

float He4v_z_1_7[12][2]   = {{1.0, 0.186E-1}, {1.3, 0.257E-1},
                                   {1.4, 0.148E-1}, {1.5, 0.160E-1},
                                   {1.7, 0.143E-1}, {2.0, 0.200E-1},
                                   {2.5, 0.276E-1}, {3.0, 0.329E-1},
                                   {4.0, 0.313E-1}, {5.0, 0.314E-1},
                                   {7.0, 0.358E-1}, {8.0, 0.390E-1}};

float N14v_z_1_7[12][2]   = {{1.0, 0.773E-3}, {1.3, 0.122E-2},
                                   {1.4, 0.867E-3}, {1.5, 0.986E-3},
                                   {1.7, 0.102E-2}, {2.0, 0.127E-2},
                                   {2.5, 0.154E-2}, {3.0, 0.173E-2},
                                   {4.0, 0.182E-2}, {5.0, 0.729E-2},
                                   {7.0, 0.976E-2}, {8.0, 0.108E-1}};

float O16v_z_1_7[12][2]   = {{1.0, 0.981E-3}, {1.3, 0.187E-2},
                                   {1.4, 0.416E-3}, {1.5, 0.371E-3},
                                   {1.7, 0.178E-3}, {2.0, 0.777E-4},
                                   {2.5, -.419E-4}, {3.0, -.147E-5},
                                   {4.0, -.216E-3}, {5.0, -.291E-3},
                                   {7.0, -.128E-2}, {8.0, -.160E-2}};

float He4ww_1[10][2]     = {{12.0, 4.11}, {13.0, 4.51},
                                  {15.0, 5.24}, {18.0, 6.28},
                                  {20.0, 6.72}, {22.0, 7.51},
                                  {25.0, 8.64}, {30.0, 10.4},
                                  {35.0, 11.9}, {40.0, 13.0}};

float N14ww_1[10][2]     = {{12.0, 3.60E-2}, {13.0, 4.68E-2},
                                  {15.0, 5.40E-2}, {18.0, 5.68E-2},
                                  {20.0, 5.98E-2}, {22.0, 6.73E-2},
```

```
                                {25.0, 7.93E-2}, {30.0, 1.04E-1},
                                {35.0, 1.25E-1}, {40.0, 1.41E-1}};

float O16ww_1[10][2]        = {{12.0, 0.210}, {13.0, 0.272},
                                {15.0, 0.680}, {18.0, 1.130},
                                {20.0, 1.940}, {22.0, 2.380},
                                {25.0, 3.250}, {30.0, 4.880},
                                {35.0, 5.820}, {40.0, 6.030}};

float S32ww_1[10][2]        = {{12.0, 7.57E-2}, {13.0, 2.60E-2},
                                {15.0, 6.34E-2}, {18.0, 5.46E-2},
                                {20.0, 1.52E-1}, {22.0, 1.72E-1},
                                {25.0, 1.41E-1}, {30.0, 9.99E-2},
                                {35.0, 1.68E-2}, {40.0, 1.15E-2}};

float Fe56ww_1[10][2]       = {{12.0, 1.22E-2}, {13.0, 1.28E-2},
                                {15.0, 1.47E-2}, {18.0, 1.71E-2},
                                {20.0, 1.83E-2}, {22.0, 1.97E-2},
                                {25.0, 2.19E-2}, {30.0, 2.53E-2},
                                {35.0, 2.78E-2}, {40.0, 2.84E-2}};

float He4ww_0_1[10][2]      = {{12.0, 3.91}, {13.0, 4.30},
                                {15.0, 5.04}, {18.0, 6.18},
                                {20.0, 6.70}, {22.0, 7.42},
                                {25.0, 8.60}, {30.0, 10.5},
                                {35.0, 12.0}, {40.0, 14.0}};

float N14ww_0_1[10][2]      = {{12.0, 2.90E-3}, {13.0, 4.03E-3},
                                {15.0, 4.85E-3}, {18.0, 5.67E-3},
                                {20.0, 6.30E-3}, {22.0, 6.94E-3},
                                {25.0, 8.56E-3}, {30.0, 1.08E-2},
                                {35.0, 1.29E-2}, {40.0, 1.59E-2}};

float O16ww_0_1[10][2]       = {{12.0, 0.145}, {13.0, 0.290},
                                 {15.0, 0.555}, {18.0, 0.994},
                                 {20.0, 1.52}, {22.0, 2.12},
                                 {25.0, 2.90}, {30.0, 4.42},
                                 {35.0, 5.78}, {40.0, 6.25}};

float S32ww_0_1[10][2]       = {{12.0, 1.36E-2}, {13.0, 3.15E-2},
                                 {15.0, 3.40E-2}, {18.0, 4.80E-2},
```

```
                                {20.0, 1.29E-1}, {22.0, 1.84E-1},
                                {25.0, 2.17E-1}, {30.0, 6.44E-2},
                                {35.0, 5.52E-3}, {40.0, 2.03E-3}};

float Fe56ww_0_1[10][2]     = {{12.0, 6.97E-4}, {13.0, 8.03E-4},
                                {15.0, 8.56E-4}, {18.0, 1.01E-3},
                                {20.0, 1.08E-3}, {22.0, 1.17E-3},
                                {25.0, 1.33E-3}, {30.0, 1.53E-3},
                                {35.0, 1.67E-3}, {40.0, 1.86E-3}};

float He4ww_0_0_1[10][2]    = {{12.0, 3.90}, {13.0, 4.28},
                               {15.0, 5.09}, {18.0, 6.25},
                               {20.0, 6.62}, {22.0, 7.50},
                               {25.0, 8.76}, {30.0, 10.3},
                               {35.0, 12.0}, {40.0, 13.9}};

float N14ww_0_0_1[10][2]    = {{12.0, 3.33E-4}, {13.0, 4.36E-4},
                                {15.0, 5.43E-4}, {18.0, 6.24E-4},
                                {20.0, 6.81E-4}, {22.0, 7.77E-4},
                                {25.0, 9.29E-4}, {30.0, 1.15E-3},
                                {35.0, 1.42E-3}, {40.0, 1.68E-3}};

float O16ww_0_0_1[10][2]    = {{12.0, 0.142}, {13.0, 0.210},
                                {15.0, 0.423}, {18.0, 0.952},
                                {20.0, 1.62}, {22.0, 1.94},
                                {25.0, 2.83}, {30.0, 4.45},
                                {35.0, 5.65}, {40.0, 6.19}};

float S32ww_0_0_1[10][2]    = {{12.0, 1.40E-2}, {13.0, 2.18E-2},
                                {15.0, 3.46E-2}, {18.0, 5.61E-2},
                                {20.0, 1.48E-1}, {22.0, 1.48E-1},
                                {25.0, 2.05E-1}, {30.0, 9.82E-2},
                                {35.0, 1.11E-1}, {40.0, 4.31E-4}};

float Fe56ww_0_0_1[10][2] = {{12.0, 5.08E-5}, {13.0, 5.41E-5},
                                {15.0, 6.32E-5}, {18.0, 7.86E-5},
                                {20.0, 8.38E-5}, {22.0, 8.93E-5},
                                {25.0, 1.05E-4}, {30.0, 1.17E-4},
                                {35.0, 1.32E-4}, {40.0, 1.33E-4}};

float Tau[20][2]            = {{0.8, 25.03}, {0.9, 15.50},
```

```
                                   {1.0, 9.962}, {1.5, 2.695},
                                   {1.7, 1.827}, {2.0, 1.116},
                                   {2.5, 0.585}, {3.0, 0.353},
                                   {4.0, 0.165}, {5.0, 0.094},
                                   {7.0, 0.043}, {9.0, 0.026},
                                   {12.0, 0.016}, {15.0, 0.012},
                                   {20.0, 0.008}, {25.0, 0.006},
                                   {40.0, 0.004}, {60.0, 0.003},
                                   {85.0, 0.003}, {120.0, 0.002}};

float Turn_off[20][2]            = {{0.002, 120.0}, {0.003, 85.0},
                                   {0.003, 60.0}, {0.004, 40.0},
                                   {0.006, 25.0}, {0.008, 20.0},
                                   {0.012, 15.0}, {0.016, 12.0},
                                   {0.026, 9.0}, {0.043, 7.0},
                                   {0.094, 5.0}, {0.165, 4.0},
                                   {0.353, 3.0}, {0.585, 2.5},
                                   {1.116, 2.0}, {1.827, 1.7},
                                   {2.695, 1.5}, {9.962, 1.0},
                                   {15.50, 0.9}, {25.03, 0.8}};

float remn[10][2]                = {{12.0, 10.7}, {13.0, 11.6},
                                   {15.0, 13.6}, {18.0, 16.3},
                                   {20.0, 18.0}, {22.0, 20.1},
                                   {25.0, 23.1}, {30.0, 28.2},
                                   {35.0, 31.3}, {40.0, 32.5}};

#endif
```

B.5 Sample Makefile

```
CPP    = g++
INC    = -I/usr/include/g++
EXEC   = NICE

CFLAGS = -O2 -s -fforce-addr -ffast-math \
 -fstrength-reduce -funroll-all-loops

SOURCE = nice_functions.cc \
         nice.cc

OBJECTS = nice_functions.o \
          nice.o

$(EXEC): $(OBJECTS)
$(CPP) $(CFLAGS) -o $@ $(OBJECTS) -lm

clean:
-rm -f *.o *.*~
```

IMAGE EVALUATION TEST TARGET (QA-3)

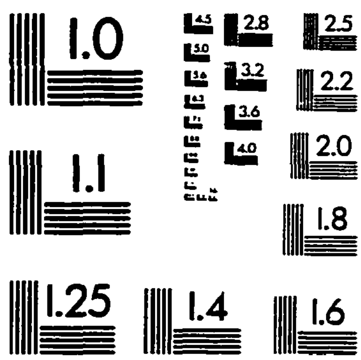

150mm

6"

APPLIED IMAGE, Inc
1653 East Main Street
Rochester, NY 14609 USA
Phone: 716/482-0300
Fax: 716/288-5989